Effective model for meson screening and pole masses at finite temperature

石井, 優大

https://doi.org/10.15017/1806807

出版情報：九州大学, 2016, 博士（理学）, 課程博士
バージョン：

Effective model for meson screening and pole masses at finite temperature

Masahiro Ishii

Theoretical Nuclear Physics, Department of Physics
Graduate School of Science, Kyushu University
744, Motooka, Nishi-ku, Fukuoka 819-0395, Japan

Abstract

Temperature (T) dependence of meson mass is an essential quantity characterizing properties of hot-QCD matter. T dependence of meson masses is obtainable through measurements of mesons and leptons emitted in heavy-ion collisions, but the experimental results have large uncertainty because of indirect measurements. In this thesis, the meson mass is referred to as "meson pole mass" in order to distinguish it from "meson screening mass". Meson pole and screening masses, $M_\xi^{\rm pole}(T)$ and $M_\xi^{\rm scr}(T)$, of ξ-meson are defined by the inverse of the exponential decay of the mesonic correlation functions in its temporal and spatial directions, respectively. This definition means that $M_\xi^{\rm pole}(T)$ is experimentally measurable, but $M_\xi^{\rm scr}(T)$ is not. In lattice QCD (LQCD) simulations at finite T as the first-principle calculation of QCD, the $M_\xi^{\rm scr}(T)$ is usually calculated instead of $M_\xi^{\rm pole}(T)$, since the temporal (imaginary-time) size is limited up to $1/T$, but the spatial lattice size doesn't have such limitation in general. The relation between $M_\xi^{\rm pole}(T)$ and $M_\xi^{\rm scr}(T)$ at finite T is not understood at all, although $M_\xi^{\rm pole}(0) = M_\xi^{\rm scr}(0)$ from the definition.

This thesis aims at predicting meson pole masses $M_\xi^{\rm pole}(T)$ reliably from the corresponding meson screening masses $M_\xi^{\rm scr}(T)$ calculated with LQCD simulations. For this purpose, we construct the practical and reliable effective model that reproduces LQCD data on $M_\xi^{\rm scr}(T)$ and describe the chiral-symmetry restoration and the effective $U(1)_{\rm A}$-symmetry restoration simultaneously. In effective models, screening-mass calculations were quite difficult compared with pole-mass calculations, because it required time-consuming numerical calculations. This difficulty is solved by proposing a new method based on the Pauli-Villars regularization and a new prescription in calculating the spatial correlation function for $M_\xi^{\rm scr}(T)$. We have then predicted $M_\xi^{\rm pole}(T)$ from LQCD data on $M_\xi^{\rm scr}(T)$ by using the proposed model for both scalar mesons ($\xi = a_0, \kappa, \sigma$ and f_0) and pseudoscalar ones ($\xi = \pi, K, \eta$ and η'). Particularly for η' meson, we have found that the predicted value is consistent with the experimental value recently measured in heavy-ion collisions. The model also proposes the following approximate relations between $M_\xi^{\rm pole}(T)$ and $M_\xi^{\rm scr}(T)$: (i) $M_\xi^{\rm scr}(T) - M_\xi^{\rm pole}(T) \approx M_{\xi'}^{\rm scr}(T) - M_{\xi'}^{\rm pole}(T)$ and (ii) $M_\xi^{\rm scr}(T)/M_{\xi'}^{\rm scr}(T) \approx M_\xi^{\rm pole}(T)/M_{\xi'}^{\rm pole}(T)$, when ξ'-meson has the same spin-parity as ξ-meson. Using relations (i) and (ii), we can easily estimate $M_\xi^{\rm pole}(T)$ from $M_\xi^{scr}(T), M_{\xi'}^{\rm scr}(T)$ and $M_{\xi'}^{\rm pole}(T)$. When ξ'-meson is heavy, $M_{\xi'}^{\rm pole}(T)$ may be obtainable with state-of-arts LQCD simulations.

Contents

Abstract **i**

1 Introduction **1**
1.1 Quark matter at finite temperature 1
1.1.1 Deconfinement transition and center symmetry 2
1.1.2 Spontaneous breaking of chiral symmetry 4
1.1.3 Instantons and $U(1)_{\mathrm{A}}$ symmetry breaking 5
1.2 Experimental surveys for quark matter 6
1.3 Lattice QCD and effective models 6
1.4 Meson masses 8
1.5 Purpose 9

2 Formulation for meson screening mass **10**
2.1 2-flavor PNJL and EPNJL models 10
2.2 Mesonic correlation functions 12
2.3 Difficulty of screening-mass calculations 15
2.4 Meson screening mass in EPNJL model 16
2.5 Numerical Results 18
2.6 Short Summary 20

3 $U(1)_{\mathrm{A}}$ symmetry restoration **22**
3.1 $U(1)_{\mathrm{A}}$ symmetry and Columbia plot 22
3.2 Model setting 24
3.2.1 EPNJL model 24
3.2.2 Mesonic correlation functions 26
3.2.3 Meson pole mass 29
3.2.4 Meson screening mass 29
3.2.5 Meson susceptibility 30
3.3 Numerical Results 31
3.3.1 Meson screening masses 31
3.3.2 Meson susceptibilities 36
3.3.3 The order of chiral transition near the physical point . 38
3.4 Short Summary 40

4 Model prediction for meson pole masses **41**
4.1 Formalism . . . 41
4.1.1 Model setting . . . 41
4.1.2 Meson pole masses . . . 45
4.1.3 Meson screening masses . . . 49
4.1.4 Model tuning for LQCD-data analyses . . . 51
4.2 Numerical Results . . . 53
4.2.1 Parameter fitting . . . 53
4.2.2 Meson screening masses . . . 55
4.2.3 Meson pole masses . . . 56
4.2.4 Relation between pole and screening masses . . . 58
4.2.5 Discussion . . . 61
4.3 Short Summary . . . 62

5 Summary and Outlook **64**

List of Figures

1.1 Running coupling constant α_s as a function of energy scale Q taken from Ref. [1]. 2

2.1 Singularities of $\chi_{\xi\xi}(0, \tilde{q}^2)$ in the complex-$\tilde{q}$ plane 16
2.2 T dependence of chiral condensate and Polyakov loop in the 2-flavor system. 19
2.3 T dependence of pion and sigma-meson screening masses calculated with the PNJL and EPNJL models. 20

3.1 Columbia plot 23
3.2 T dependence of pion and a_0-meson screening masses calculated by EPNJL model with $K(T)$. 31
3.3 T dependence of pion and a_0-meson screening masses calculated by PNJL model with $K(T)$. 32
3.4 T dependence of $\Delta_{l,s}$ and Φ. 33
3.5 T dependence of pion and a_0-meson screening masses calculated by PNJL model with $K(0)$. 34
3.6 T dependence of pion and a_0-meson screening masses calculated by PNJL model with $K(0)$. 35
3.7 Mass difference $\Delta M_{\rm scr}(T)$ between pion and a_0-meson screening masses. 35
3.8 T dependence of the difference Δ_{π,a_0} between π and a_0 meson susceptibilities for two cases of $M_\pi(0) = 135$ and 200 MeV. . . 36
3.9 T dependence of $\Delta_{\pi,\sigma}$ and Δ_{η,a_0} for $M_\pi(0) = 135$ MeV. 37
3.10 T dependence of $\Delta_{\pi,\sigma}$ and Δ_{η,a_0} for $M_\pi(0) = 200$ MeV. 37
3.11 T dependence of (a) chiral susceptibility χ_{ll} and (b) Polyakov-loop susceptibility $\bar{\chi}_{\Phi\bar{\Phi}}$ at S-point, P-point and C_l-point. . . . 38
3.12 Order of chiral transition near physical point in the m_l–m_s plane. 39

4.1 T dependence of (a) $\Delta_{l,s}$ and (b) $\Delta M^{\rm scr}_{a_0,\pi}$. 53
4.2 T dependence of meson screening masses for (a) pseudoscalar mesons $\pi, K, \eta_{\bar{s}s}$ and (b) scalar mesons $a_0, \kappa, \sigma_{\bar{s}s}$ 54

4.3 T dependence of meson screening masses for (a) pseudoscalar mesons π, K, η, η' and (b) scalar mesons a_0, κ, σ, f_0 calculated with the realistic parameter set (A). 56
4.4 Model prediction on T dependence of meson pole masses for (a) pseudoscalar mesons π, K, η, η' and (b) scalar mesons a_0, κ, σ, f_0 57
4.5 Difference between screening and pole masses for (a) pseudoscalar mesons π, K, η, η' and (b) scalar mesons a_0, κ, σ, f_0 . . 58
4.6 T dependence of $M_\xi^{\rm pole}/M_{\xi'}^{\rm pole}$ and $M_\xi^{\rm scr}/M_{\xi'}^{\rm scr}$ for (a) pseudoscalar mesons ($\xi = K, \eta, \eta',\ \xi' = \pi$) and (b) scalar mesons ($\xi = \kappa, \sigma, f_0,\ \xi' = a_0$). 60
4.7 T dependence of channel-mixing effects on (a) η- and η'-meson screening masses and (b) σ- and f_0-meson screening masses. . 61

List of Tables

1.1 Experimental values on current quark masses 2

2.1 Parameter set of Polyakov-loop potential $\mathcal{U}$. 11
2.2 Parameter sets of EPNJL model for 2-flavor and 2+1-flavor systems. 12

4.1 Model parameters in coupling strengths $G_{\rm S}(T)$ and $G_{\rm D}(T)$. . 42
4.2 Two model-parameter sets 44
4.3 Physical quantities at vacuum calculated with the parameter set (A) of Table 4.2 and the corresponding experimental or empirical values. 45

Chapter 1

Introduction

1.1 Quark matter at finite temperature

Strong interaction is one of the four basic interactions existing in the nature. The interaction is working among quarks and gluons. In this sense, quarks and gluons are fundamental particles in the nature. At low temperature (T), they are confined into hadrons by strong interaction. As T increases, the mean distance among hadrons and anti-hadrons gets shorter, and consequently hadrons and anti-hadrons start to overlap with each other. At extremely high T, hadrons are considered to melt into quarks and gluons gas, i.e., quark–gluon plasma (QGP). In fact, the QGP phase exists in the early universe, and the QGP phase is changed into the hadron phase as a result of the cooling (expansion) of the universe. The transition between the hadron and QGP phases has been studied experimentally and theoretically; however, it has not been revealed yet. Elucidation of quark and hadron matters at finite T is an essential subject between particle physics and cosmology, that is, a bridge between the two fields.

The strong interaction is known to be described by quantum chromodynamics (QCD). The Lagrangian density in Euclid spacetime is

$$\mathcal{L}_{\rm QCD} = \bar{\psi}\left(\gamma_\mu D_\mu + \hat{m}\right)\psi + \frac{1}{2}{\rm tr_c}\left(F_{\mu\nu}^2\right) \tag{1.1}$$

for quark fields ψ and gluon fields A_μ. The trace $\mathrm{tr_c}$ is taken in color space. The ψ is $\psi = (\psi_{\rm u}, \psi_{\rm d}, \psi_{\rm s}, \psi_{\rm c}, \psi_{\rm b}, \psi_{\rm t})^{\rm T}$ for up (u), down (d), strange (s), charm (c), bottom (b), and top (t) quarks. The A_μ are connected with ψ through the covariant derivative $D_\mu = \partial_\mu - igA_\mu$ with the coupling constant g. Gluon dynamics is organized by the field strength tensor $F_{\mu\nu}$:

$$F_{\mu\nu} = \partial_\mu A_\nu - \partial_\nu A_\mu + ig[A_\mu, A_\nu]. \tag{1.2}$$

The current-quark-mass matrix $\hat{m}$ is $\hat{m} = {\rm diag}(m_{\rm u}, m_{\rm d}, m_{\rm s}, m_{\rm c}, m_{\rm b}, m_{\rm t})$ and the values are tabulated in Table 1.1. In this study, we focus on the nonperturbative aspects of hot-QCD matter that are realized in lower temperatures of order $\Lambda_{\rm QCD} \sim 200$ MeV as a typical energy scale of QCD. Therefore we consider dynamics of the light quarks (u, d, and s quarks) whose current masses are smaller than $\Lambda_{\rm QCD}$.

Table 1.1: Experimental values on current quark masses taken from Ref. [1].

m_{u}	m_{d}	m_{s}	m_{c}	m_{b}	m_{t}
2.3 MeV	4.8 MeV	95 MeV	1.275 GeV	4.18 GeV	160 GeV

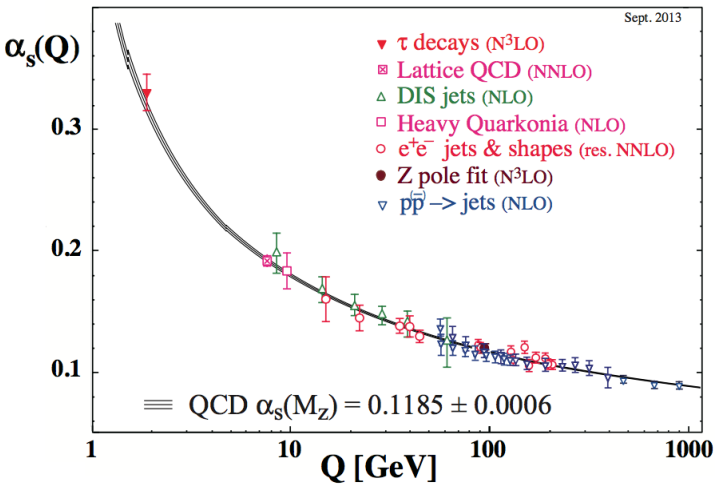

Fig. 1.1: Running coupling constant α_s as a function of energy scale Q taken from Ref. [1].

The most important property of QCD is asymptotic freedom. Strong interaction among quarks and gluons gets weaker as the energy scale Q goes up. The Q dependence of the running coupling constant $\alpha_{\mathrm{s}}(Q)$ is experimentally measured in the deep-inelastic scattering (DIS) between leptons and hadrons, τ decay, and so on, as shown in Fig. 1.1. The symbols denote the experimental results and the lines denote the theoretical predictions based on perturbation theory. The perturbation well reproduces the experimental results in $Q > 1$ GeV.

In low $Q \leq 1$ GeV, the QCD vacuum has nonperturbative structures such as color confinement, the spontaneous breaking of chiral symmetry, and the existence of instantons and antiinstantons. They come from large/local gauge and global symmetries that the QCD Lagrangian possesses.

1.1.1 Deconfinement transition and center symmetry

The transition from the hadron (confinement) phase at low T to the QGP (deconfinement) phase at high T is characterized by the spontaneous breaking of "center symmetry", as shown below. The symmetry is exact in the pure Yang–Mills theory, but not in QCD. The pure Yang–Mills theory corresponds to QCD in the limit of heavy quark mass. In QCD, the expectation value

$\langle O \rangle$ of an operator O is obtained with the path integral as

$$\langle O \rangle = \frac{1}{Z} \int_{\rm BC} \mathcal{D}\psi \mathcal{D}\bar{\psi} \mathcal{D}A_\mu \; O[\psi, \bar{\psi}, A_\mu] \; \exp\left[-(S_{\rm Quark}[\psi, \bar{\psi}, A_\mu] + S_{\rm YM}[A_\mu]) \right], \tag{1.3}$$

where the quark and Yang–Mills parts of QCD action, $S_{\rm Quark}$ and $S_{\rm YM}$, are

$$S_{\rm Quark} = \int_0^\beta d\tau \int d^3\boldsymbol{x} \; \bar{\psi}(\gamma_\mu D_\mu + \hat{m})\psi, \quad S_{\rm YM} = \int_0^\beta d\tau \int d^3\boldsymbol{x} \; \frac{1}{2} {\rm tr_c}(F_{\mu\nu}^2) \tag{1.4}$$

in Euclidean spacetime $(x^\mu) = (\tau, \boldsymbol{x})$ where imaginary time τ has an upper limit $\beta = 1/T$. The partition function Z of QCD is described as

$$Z = \int_{\rm BC} \mathcal{D}\psi \mathcal{D}\bar{\psi} \mathcal{D}A_\mu \; \exp\left[-(S_{\rm Quark}[\psi, \bar{\psi}, A_\mu] + S_{\rm YM}[A_\mu]) \right]. \tag{1.5}$$

The subscript "BC" of the integral means the boundary conditions

$$\psi\left(\tau + \beta, \boldsymbol{x}\right) = -\psi\left(\tau, \boldsymbol{x}\right), \quad \bar{\psi}\left(\tau + \beta, \boldsymbol{x}\right) = -\bar{\psi}\left(\tau, \boldsymbol{x}\right), \tag{1.6}$$

$$A_\mu\left(\tau + \beta, \boldsymbol{x}\right) = A_\mu\left(\tau, \boldsymbol{x}\right) \tag{1.7}$$

for $\psi, \bar{\psi}$ and A_μ. In the τ direction, we should impose the antiperiodic boundary condition on fermions such as quarks, and the periodic boundary condition on bosons such as gluons. Now we consider the following local ${\rm SU(3)_c}$ gauge transformation

$$\begin{aligned} \psi(x) &\rightarrow \psi'(x) = V(x)\psi(x), \\ A_\mu(x) &\rightarrow A'_\mu(x) = V(x)\left(A_\mu(x) - \frac{i}{g}\partial_\mu \right) V^\dagger(x) \end{aligned} \tag{1.8}$$

with the *aperiodic* boundary condition

$$V\left(\tau + \beta, \boldsymbol{x}\right) = \boldsymbol{z} V\left(\tau, \boldsymbol{x}\right) \tag{1.9}$$

for $V(x)$ in the τ direction. The symbol $\boldsymbol{z}$ is the "center" of ${\rm SU(3)_c}$ group that commutes with all the elements of ${\rm SU(3)_c}$, and it is defined as

$$\boldsymbol{z} = e^{2\pi i k/3} \boldsymbol{I}_{\rm C} \equiv z_3 \boldsymbol{I}_{\rm C} \quad (k = 0, 1, 2) \tag{1.10}$$

with the unit matrix $\boldsymbol{I}_{\rm C}$ in color space. We call the transformation as "$\rm Z_3$ transformation" in order to distinguish it from the usual gauge transformation (1.8)-(1.9) with $\boldsymbol{z}$ replaced by $\boldsymbol{I}_{\rm C}$. In QCD, the Lagrangian is invariant under the $\rm Z_3$ transformation. This symmetry is then referred to be "center symmetry". However, the $\rm Z_3$ transformation modifies the boundary condition for $\psi, \bar{\psi}$ as

$$\psi'\left(\tau + \beta, \boldsymbol{x}\right) = -z_3 \psi'\left(\tau, \boldsymbol{x}\right), \quad \bar{\psi}'\left(\tau + \beta, \boldsymbol{x}\right) = -z_3^* \bar{\psi}'\left(\tau, \boldsymbol{x}\right). \tag{1.11}$$

Therefore, *center symmetry is explicitly broken through the boundary condition for dynamical quarks, although it is preserved in QCD Lagrangian itself.*

Center symmetry becomes exact in pure Yang–Mills theory, since the theory has no quark-dynamics.

Center symmetry is considered to be approximately good in QCD, particularly for heavy quarks. An order parameter of the center-symmetry breaking is the Polyakov loop $\Phi \equiv \langle \Phi(\boldsymbol{x}) \rangle$ where the Polyakov-loop operator $\Phi(\boldsymbol{x})$ is defined by

$$\Phi(\boldsymbol{x}) = \frac{1}{3}\mathrm{tr_c}\mathcal{T}\exp\left(ig\int_0^\beta d\tau\ A_4(\tau,\boldsymbol{x})\right). \tag{1.12}$$

Here, the symbol $\mathcal{T}$ stands for the path ordering for τ. Under the Z_3 transformation, the Polyakov-loop operator is transformed as

$$\Phi(\boldsymbol{x}) \to \Phi'(\boldsymbol{x}) = z_3\Phi(\boldsymbol{x}). \tag{1.13}$$

This property means that $\Phi = 0$ corresponds to the center-symmetric phase and $\Phi \neq 0$ does to the center-symmetry broken phase. The Polyakov loop is related to an excitation energy F_Q of single heavy quark as [2]

$$\Phi \propto \exp\left(-\beta F_\mathrm{Q}\right). \tag{1.14}$$

In the confinement phase, F_Q should be infinity, so that $\Phi = 0$. Therefore, the confinement phase is center-symmetric. In the deconfinement phase, F_Q is finite, so that $\Phi \neq 0$. Hence, center symmetry is broken in the deconfinement phase. The Polyakov loop is thus an order parameter of the breaking of center symmetry, that is, the confinement/deconfinement transition:

$$\Phi = \begin{cases} 0 & \text{for} \quad \text{the confinement phase with center symmetry,} \\ \text{finite} & \text{for} \quad \text{the deconfinement phase without center symmetry.} \end{cases} \tag{1.15}$$

1.1.2 Spontaneous breaking of chiral symmetry

In the chiral limit of $m_\mathrm{u} = m_\mathrm{d} = m_\mathrm{s} = 0$, QCD Lagrangian (1.1) is invariant under the flavor $U(3)_\mathrm{R} \times U(3)_\mathrm{L}$ rotation for the right- and left-handed quarks, ψ_R and ψ_L, defined by

$$\psi_\mathrm{R} = P_+\psi, \quad \psi_\mathrm{L} = P_-\psi \tag{1.16}$$

with $\psi = (\psi_\mathrm{u}, \psi_\mathrm{d}, \psi_\mathrm{s})^\mathrm{T}$ and the projection operators $P_\pm = (1 \pm \gamma_5)/2$. We rewrite the Lagrangian with ψ_R and ψ_L fields as

$$\mathcal{L}_\mathrm{QCD} = \bar{\psi}_\mathrm{R}\gamma_\mu D_\mu \psi_\mathrm{R} + \bar{\psi}_\mathrm{L}\gamma_\mu D_\mu \psi_\mathrm{L} + (\bar{\psi}_\mathrm{R}\hat{m}\psi_\mathrm{L} + \bar{\psi}_\mathrm{L}\hat{m}\psi_\mathrm{R}) + \cdots, \tag{1.17}$$

where $\hat{m} = \mathrm{diag}(m_\mathrm{u}, m_\mathrm{d}, m_\mathrm{s})$. The global $U(3)_\mathrm{R} \times U(3)_\mathrm{L}$ transformation with rotation angles $\boldsymbol{\alpha}$ and $\boldsymbol{\beta}$ is

$$\begin{aligned} \psi_\mathrm{R} \to \psi'_\mathrm{R} = U(\boldsymbol{\alpha})\psi_\mathrm{R}, \quad \psi_\mathrm{L} \to \psi'_\mathrm{L} = U(\boldsymbol{\beta})\psi_\mathrm{L}, \\ \bar{\psi}_\mathrm{R} \to \bar{\psi}'_\mathrm{R} = \bar{\psi}_\mathrm{R}U^\dagger(\boldsymbol{\alpha}), \quad \bar{\psi}_\mathrm{L} \to \bar{\psi}'_\mathrm{L} = \bar{\psi}_\mathrm{L}U^\dagger(\boldsymbol{\beta}). \end{aligned} \tag{1.18}$$

Here, $U(\boldsymbol{\theta})$ is a unitary matrix with rotation angles $\boldsymbol{\theta} = (\theta^0, ..., \theta^8)$:

$$U(\boldsymbol{\theta}) = \exp\left(i \sum_{a=0}^{8} \theta^a T^a \right) \tag{1.19}$$

with the matrices T^a defined by

$$T^0 = \sqrt{\frac{2}{3}} \boldsymbol{I}_{\rm F}, \quad T^a = \frac{\lambda^a}{2} \quad (a = 1, 2, ..., 8), \tag{1.20}$$

where the $\boldsymbol{I}_{\rm F}$ is the unit matrix and the λ^a correspond to the Gell-Mann matrices in flavor space. The transformation (1.18) with $\boldsymbol{\beta} = -\boldsymbol{\alpha}$ is called "chiral transformation", and QCD Lagrangian (1.17) is invariant under the chiral transformation in the chiral limit. If one considers finite current-quark masses, chiral symmetry is explicitly broken by the mass terms in QCD Lagrangian (1.17). The explicit breaking seems to be small, since $m_u, m_d, m_s < \Lambda_{\rm QCD} \sim 200$ MeV. Therefore chiral symmetry is approximately good in QCD Lagrangian. However, in QCD vacuum, chiral symmetry is not preserved and $U(3)_{\rm R} \times U(3)_{\rm L}$ symmetry is broken into $SU(3)_{\rm V} \times U(1)_{\rm V} \times U(1)_{\rm A}$ symmetry. This is called "the spontaneous breaking of chiral symmetry". An order parameter of the breaking is chiral condensate

$$\langle \bar{\psi}_f \psi_f \rangle = \langle \bar{\psi}_{{\rm R},f} \psi_{{\rm L},f} \rangle + \langle \bar{\psi}_{{\rm L},f} \psi_{{\rm R},f} \rangle \tag{1.21}$$

for flavor f. The condition $\langle \bar{\psi}_f \psi_f \rangle = 0$ corresponds to the chiral-symmetric phase and $\langle \bar{\psi}_f \psi_f \rangle \neq 0$ does to the chiral-symmetry broken phase as

$$\langle \bar{\psi}_f \psi_f \rangle = \begin{cases} 0 & \text{for} \quad \text{the chiral-symmetric phase,} \\ \text{finite} & \text{for} \quad \text{the chiral-symmetry broken phase.} \end{cases} \tag{1.22}$$

1.1.3 Instantons and $U(1)_{\rm A}$ symmetry breaking

In Ref. [3], Weinberg considered the relation between pion mass (M_π) and η'-meson mass ($M_{\eta'}$). He pointed out that current algebra indicates $M_{\eta'} \leq \sqrt{3} M_\pi$ and this result is inconsistent with the experimental result $M_{\eta'} \gg \sqrt{3} M_\pi$. This problem was solved by considering quantum anomaly of axial current and introducing topologically nontrivial gauge configurations, each with different winding number ν, in QCD vacuum. In the chiral limit ($\hat{m} = 0$), the quantum anomaly leads to

$$\partial_\mu j_{5\mu}(x) = -2 N_{\rm f} Q(x) \tag{1.23}$$

as a relation between the $U(1)_{\rm A}$ current $j_{5\mu}(x)$ and the topological charge density $Q(x)$, which are defined by

$$j_{5\mu}(x) = \bar{\psi}(x) \gamma_\mu \gamma_5 \psi(x), \quad Q(x) = \frac{g^2}{16\pi^2} {\rm tr}_{\rm c} \left(F_{\mu\nu}(x) \tilde{F}_{\mu\nu}(x) \right) \tag{1.24}$$

with the number $N_{\rm f}$ of flavors and

$$\tilde{F}_{\mu\nu}(x) = \frac{1}{2}\epsilon_{\mu\nu\rho\sigma}F_{\rho\sigma}(x). \tag{1.25}$$

The winding number ν is defined by

$$\nu \equiv \int d^4x\ Q(x). \tag{1.26}$$

The nontrivial gauge configuration with $\nu = 1$ ($\nu = -1$) is called instanton (antiinstanton).

In the operator level, $U(1)_{\rm A}$ symmetry is always broken through $Q(x)$, as shown in Eq. (1.23). For the expectation value of Eq. (1.23), the $U(1)_{\rm A}$-symmetry breaking is affected by the nontrivial structure of QCD vacuum. After integrating both the sides of Eq. (1.23) in spacetime x, global $U(1)_{\rm A}$ symmetry is approximately conserved if QCD vacuum is dominated by topologically trivial ($\nu = 0$) gauge configurations [4]. In this sense, the $U(1)_{\rm A}$-symmetry breaking due to finite ν is simply called "$U(1)_{\rm A}$ anomaly" in this thesis.

1.2 Experimental surveys for quark matter

In experiments, properties of hot-QCD matter have been explored through measurements of hadrons and leptons produced in heavy-ion collisions. Heavy ions are collided with incident energies large enough to create QGP. In Relativistic heavy-ion collider (RHIC) experiments [5], QGP is considered to be realized in the intermediate stage of the collisions by measuring various kinds of flows and jets of hadrons. Similar measurements have been performed by changing incident energies, centrality, and targets with Large Hadron Collider (LHC) in CERN, Facility for Antiproton and Ion Research (FAIR) in GSI, Nuclotron-based Ion Collider fAcility (NICA) in Dubna, and Japan Proton Accelerator Research Complex (JPARC) in KEK.

T dependence of meson mass is the essential quantity that characterizes properties of hot-QCD matter. In principle, one can determine T dependence of meson masses through measurements of mesons emitted in heavy-ion collisions. However, the experimental results have large uncertainty in general, because they are indirect measurements. In fact, η'-meson mass measured at finite T has large errors that mainly come from data analyses [6].

1.3 Lattice QCD and effective models

Lattice QCD (LQCD) simulation is the first-principle calculation of QCD and hot-QCD. In the simulations, spacetime x is discretized into a lattice. Each lattice point is labeled by a vector $n = (n_x, n_y, n_z, n_\tau)$, where $x_\mu = n_\mu a$

for lattice spacing a and integer n_μ. Quark fields $\psi(x)$ and $\bar{\psi}(x)$ are defined on each lattice point. For convenience, we introduce dimensionless quark fields ψ_n and $\bar{\psi}_n$ on each lattice point:

$$\psi(x) = a^{3/2}\psi_n, \quad \bar{\psi}(x) = a^{3/2}\bar{\psi}_n. \tag{1.27}$$

The factor $a^{3/2}$ is necessary to make ψ_n and $\bar{\psi}_n$ dimensionless. Gluon fields $A_\mu(x)$ are described as link variables

$$U_{n,\mu} \equiv U(na, na + \hat{\mu}a) \tag{1.28}$$

with the comparator

$$U(x, y) \equiv \mathcal{P} \exp\left[ig \int_x^y dz_\nu A_\nu(z)\right], \tag{1.29}$$

where $\hat{\mu}$ is the unit vector in the μ direction and the symbol $\mathcal{P}$ is the path ordering for the z-direction. The QCD partition function Z is then represented by

$$\begin{aligned} Z &= \int \mathcal{D}\psi\mathcal{D}\bar{\psi}\mathcal{D}U \ \exp\left[-\left(S_{\rm Quark}[\psi, \bar{\psi}, U] + S_{\rm YM}[U]\right)\right] \\ &= \int \mathcal{D}U \ \det\mathcal{M}[U] \ \exp\left[-S_{\rm YM}[U]\right], \end{aligned} \tag{1.30}$$

where see for example Ref. [7] for the explicit forms of $S_{\rm Quark}$, $S_{\rm YM}$, $\mathcal{M}$ and the path integral. The path integral is numerically performed by using Monte-Carlo method with the importance sampling. When $\det\mathcal{M}[U]$ is complex, the importance sampling breaks down. This problem is called "Sign problem". This problem occurs for finite quark-number chemical potential $\mu_{\rm q}$. For this reason, LQCD simulations provide a lot of results particularly at $\mu_{\rm q} = 0$.

As an approach complementary to LQCD simulations, properties of QCD and hot-QCD have been studied intensively by effective models such as the Nambu–Jona-Lasinio (NJL) model and the Polyakov-loop extended Nambu–Jona-Lasinio (PNJL) model [8–24]. In the NJL model, $U(1)_{\rm A}$ anomaly and the spontaneous breaking of chiral symmetry are taken into account. In the PNJL model, confinement is approximately considered through the Polyakov loop Φ, in addition to $U(1)_{\rm A}$ anomaly and the spontaneous breaking of chiral symmetry. These models have been applied for many phenomena. In particular, the PNJL model has been used to investigate the relation between the chiral and the deconfinement transitions. Lately, a Polyakov-loop (Φ) dependent four-quark interaction was introduced so as to enhance the correlation between the two transitions [25,26]. The PNJL model with the entanglement (Φ-dependent) four-quark interaction is now called the entanglement-PNJL (EPNJL) model [25, 26]. The EPNJL model is successful in reproducing LQCD results in the imaginary $\mu_{\rm q}$ region [27, 28] and the real isospin chemical potential region [29] where LQCD is free from the Sign problem.

1.4 Meson masses

Meson mass is a key characterizing QCD vacuum. T dependence of meson masses plays an important role in understanding properties of hot-QCD matter, for example, in determining reaction rates of hadron-hadron collisions and dilepton production.

In this thesis, the meson mass is referred to as "meson pole mass" in order to distinguish it from "meson screening mass". Meson pole and screening masses, $M_\xi^{\rm pole}(T)$ and $M_\xi^{\rm scr}(T)$, of ξ-meson are defined by the inverse of the exponential decay of the mesonic correlation functions in its temporal τ- and spatial $\boldsymbol{x}$-directions, respectively. Obviously, this definition shows that $M_\xi^{\rm pole}(T)$ is experimentally measurable, but $M_\xi^{\rm scr}(T)$ is not. On the other hand, in LQCD simulations at finite T as the first-principle calculation of QCD, the $M_\xi^{\rm scr}(T)$ is usually calculated instead of $M_\xi^{\rm pole}(T)$, since the temporal (imaginary-time) size is limited up to $1/T$, but the spatial lattice size doesn't have such limitation in general. The relation between $M_\xi^{\rm pole}(T)$ and $M_\xi^{\rm scr}(T)$ at finite T is not understood at all, although $M_\xi^{\rm pole}(0) = M_\xi^{\rm scr}(0)$ from the definition. T dependence of light-meson screening masses was evaluated lately in a wide range of $140 \lesssim T \lesssim 800$ MeV by using 2+1-flavor LQCD simulations with improved (p4) staggered fermions [30]. Thus, the $M_\xi^{\rm scr}(T)$ are available with LQCD simulations, but not measurable experimentally.

The $M_\xi^{\rm scr}(T)$ are thus obtainable with LQCD simulations but not with experiments. In contrast, the $M_\xi^{\rm pole}(T)$ are experimentally measurable but hard to obtain with LQCD simulations. If we can predict $M_\xi^{\rm pole}(T)$ theoretically from LQCD results on $M_\xi^{\rm scr}(T)$, we can compare the predicted $M_\xi^{\rm pole}(T)$ with the corresponding experimental data directly. Furthermore, when experimental data are not available for $M_\xi^{\rm pole}(T)$ of interest, such a prediction may be useful in experimental analyses.

As a complementary approach to LQCD simulations for $M_\xi^{\rm scr}(T)$ and experimental measurements for $M_\xi^{\rm pole}(T)$, we can consider effective models such as the PNJL model [8–24] and the EPNJL model [25,26]. T dependence of $M_\xi^{\rm pole}(T)$ was often studied with the NJL-type effective models [8, 12, 19, 23,24,31]. These models well describe $M_\xi^{\rm pole}(T)$ at $T = 0$, but it was difficult to calculate $M_\xi^{\rm scr}(T)$ at finite T with the NJL-type models. However, this problem was solved very recently; see Chapter 2 for the detail.

Throughout these discussions, we can find the following three problems in order to obtain $M_\xi^{\rm pole}(T)$ accurately:

(I) In principle, T dependence of $M_\xi^{\rm pole}(T)$ can be determined from measurements in heavy-ion collisions. However, the measurements are indirect, so that the experimental results have large uncertainty.

(II) LQCD simulation is the first-principle calculation of QCD. However, the calculation of $M_\xi^{\rm pole}(T)$ is quite difficult compared with $M_\xi^{\rm scr}(T)$,

because the imaginary-time size is limited up to $1/T$. The difficulty becomes more serious as T increases.

(III) In effective models, screening-mass calculations were quite difficult compared with pole-mass calculations.

1.5 Purpose

The aim of this thesis is to make a reliable model prediction on $M_\xi^{\rm pole}(T)$ from the corresponding $M_\xi^{\rm scr}(T)$ calculated with LQCD simulations. We solve problems (I)$\sim$(III) to accomplish the aim.

In Chapter 2, we solve problem (III) by considering the following two prescriptions: (1) The Pauli-Villars regularization and (2) a new prescription in calculating the spatial correlation function for $M_\xi^{\rm scr}(T)$. These two prescriptions extremely reduce numerical costs, as shown in Chapter 2.

In Chapter 3, we solve problems (I) and (II) particularly for π and a_0 mesons by proposing a new version of EPNJL model that reproduces LQCD data on $M_\pi^{\rm scr}(T)$ and $M_{a_0}^{\rm scr}(T)$.

In Chapter 4, we solve problems (I) and (II) generally for scalar and pseudoscalar mesons by proposing a new version of PNJL model that reproduces LQCD data on $M_\xi^{\rm scr}(T)$ for $\xi = \pi, K, \eta_{\bar{s}s}, a_0, \kappa, \sigma_{\bar{s}s}$ mesons.

This thesis is based on the following two published and one submitted papers:

- Effective model approach to meson screening masses at finite temperature, M. Ishii, T. Sasaki, K. Kashiwa, H. Kouno, and M. Yahiro, Phys. Rev. D 89, 071901(R) (2014).
- Determination of $U(1)_{\rm A}$ restoration from pion and a_0-meson screening masses: Toward the chiral regime, M. Ishii, K. Yonemura, J. Takahashi, H. Kouno, and M. Yahiro, Phys. Rev. D 93, 016002 (2016).
- Model prediction for temperature dependence of meson pole masses from lattice QCD results on meson screening masses, M. Ishii, H. Kouno, and M. Yahiro, submitted in Physical Review D.

Chapter 2

Formulation for meson screening mass

In this chapter, we evaluate temperature (T) dependence of pion and sigma-meson screening masses by using the Polyakov-loop extended Nambu–Jona-Lasinio (PNJL) model and the entanglement-PNJL (EPNJL) model. For this purpose, we propose a practical method of calculating meson screening masses in NJL-type effective models. Our method solves the well-known problem that the evaluation of screening masses is difficult in NJL-type effective models. The method is based on the Pauli–Villars (PV) regularization and a new prescription of calculating the correlation function for meson screening mass. We first show that the EPNJL model with the PV regularization is successful in reproducing 2-flavor lattice QCD results on T dependence of the chiral condensate and the Polyakov loop. We then apply the method to recent 2+1-flavor lattice QCD results on T dependence of pion screening mass. Since pion is composed of u and d quarks, we use 2-flavor EPNJL model for simplicity. This approximation is good enough for qualitative discussion.

2.1 2-flavor PNJL and EPNJL models

The PNJL model is one of effective models for QCD in the low-energy region. The model describes the spontaneous breaking of chiral symmetry and color confinement of quarks at the same time. The Lagrangian density of 2-flavor PNJL model in Minkowski space is defined as

$$\mathcal{L}_{\rm PNJL} = \bar{\psi}(i\gamma_\mu D^\mu - \hat{m}_0)\psi + G_{\rm S}[(\bar{\psi}\psi)^2 + (\bar{\psi}i\gamma_5\boldsymbol{\tau}\psi)^2] - \mathcal{U}(\Phi[A], \bar{\Phi}[A], T) \quad (2.1)$$

with the u-, d-quark fields $\psi = (\psi_{\rm u}, \psi_{\rm d})^{\rm T}$, the current-quark-mass matrix $\hat{m}_0 = {\rm diag}(m_{\rm u}, m_{\rm d})$ and the Pauli matrices $\boldsymbol{\tau} = (\tau_1, \tau_2, \tau_3)$ in isospin space. We consider the isospin-symmetric case for simplicity: $m_{\rm u} = m_{\rm d} = m_0$. The gauge fields A_μ are introduced through the covariant derivative

$$D_\mu = \partial_\mu + iA_\mu, \quad (2.2)$$

where the A^μ are assumed to be static background fields and $A^\mu = g\delta^\mu_0 A^0 = -ig\delta^\mu_0 A_4$ for the coupling constant g. The Polyakov loop Φ and its conjugate $\bar{\Phi}$ are then obtained in the Polyakov gauge by

$$\Phi = \frac{1}{3}\mathrm{tr_c}(L), \qquad \bar{\Phi} = \frac{1}{3}\mathrm{tr_c}(L^*) \tag{2.3}$$

with $L = \exp[iA_4/T] = \exp[i\mathrm{diag}(A_4^{11}, A_4^{22}, A_4^{33})/T]$ for the classical variables A_4^{jj} satisfying that $A_4^{11} + A_4^{22} + A_4^{33} = 0$.
The A_4^{jj} are not uniquely determined from Φ and $\bar{\Phi}$, because of the gauge symmetry, e.g., Φ and $\bar{\Phi}$ are invariant under the interchange of A_4^{11}, A_4^{22} and A_4^{33}. The arbitrariness does not change any physics. Particularly for zero quark chemical potential ($\mu = 0$), Φ equals to $\bar{\Phi}$, because the QCD Lagrangian (1.1) is invariant under the charge conjugation. Hence it is possible to determine A_4^{11}, A_4^{22} and A_4^{33} as

$$A_4^{11} = -A_4^{22} = \cos^{-1}\left(\frac{3\Phi - 1}{2}\right) T, \ A_4^{33} = 0 \tag{2.4}$$

for $\mu = 0$. Here, Φ and $\bar{\Phi}$ are mainly governed by the Polyakov-loop potential $\mathcal{U}$ in Eq. (2.1). We use the logarithm-type Polyakov-loop potential [18]

$$\mathcal{U}(\Phi, \bar{\Phi}, T) = T^4 \left[-\frac{a(T)}{2}\Phi\bar{\Phi} + b(T)\ln\left\{1 - 6\Phi\bar{\Phi} + 4(\Phi^3 + \bar{\Phi}^3) - 3(\Phi\bar{\Phi})^2\right\}\right], \tag{2.5}$$

$$a(T) = a_0 + a_1\left(\frac{T_0}{T}\right) + a_2\left(\frac{T_0}{T}\right)^2, \ b(T) = b_3\left(\frac{T_0}{T}\right)^3. \tag{2.6}$$

The parameter set in $\mathcal{U}$ is fitted to reproduce LQCD data at finite T in the pure gauge limit, i.e., QCD without dynamical quarks. The parameter set is tabulated in Table 2.1. The potential yields the first-order deconfinement

Table 2.1: Parameter set of Polyakov-loop potential $\mathcal{U}$. The parameters are taken from Ref. [18].

a_0	a_1	a_2	b_3	T_0 (Pure gauge)
3.51	−2.47	15.2	−1.75	270 [MeV]

phase transition at $T = T_0$. In the pure gauge limit, LQCD data show the phase transition at $T = 270$ MeV. Hence the parameter T_0 is often set to 270 MeV. However, if one considers dynamical quarks, the PNJL model with this value of T_0 yields a larger value of pseudocritical temperature for the deconfinement transition than the LQCD prediction. This problem can be solved by rescaling T_0, as shown in Ref. [25]. Therefore, we treat T_0 as an adjustable parameter.

The EPNJL model is an extension of the PNJL model. In the EPNJL model, the coupling constant of the four-quark interaction is assumed to depend on Φ and $\bar{\Phi}$ [25, 26]:

$$G_{\rm S}(\Phi) = G_{\rm S}(0) \cdot \left[1 - \alpha_1 \Phi\bar{\Phi} - \alpha_2 \left(\Phi^3 + \bar{\Phi}^3\right)\right]. \tag{2.7}$$

When $\alpha_1 = \alpha_2 = 0$, the EPNJL model is reduced to the PNJL model. The parameters α_1, α_2 and T_0 in the EPNJL model are determined to reproduce LQCD data on the chiral-transition temperature $T_{\rm c}^{\chi}$. The parameters are tabulated in Table 2.2. When we analyze 2-flavor LQCD results on T dependence of chiral condensate and Polyakov loop, we use the first parameter set named "2-flavor" in Table 2.2. When we analyze 2+1-flavor LQCD results on T dependence of pion screening mass, we use second parameter set named "2+1-flavor" in Table 2.2; see Sec. 2.5 for the detail.

Table 2.2: Parameter sets of EPNJL model for 2-flavor and 2+1-flavor systems.

	α_1	α_2	T_0 [MeV]
2-flavor	0.2	0.2	200
2+1-flavor	0.31	0.31	156

2.2 Mesonic correlation functions

We derive the equations for pion and sigma-meson screening masses. First, we determine the dressed quark propagator by using the mean-field (Hartree) approximation. We then treat a meson propagation as a mesonic fluctuation from the mean-field variable by taking the random-phase approximation.

Making the mean-field approximation to the Lagrangian density (2.1) leads to the linearized Lagrangian density

$$\mathcal{L}_{\rm EPNJL}^{\rm MFA} = \bar{\psi} S^{-1} \psi - U_{\rm M}(\sigma, \Phi, \bar{\Phi}) - \mathcal{U}(\Phi[A], \bar{\Phi}[A], T), \tag{2.8}$$

where S is the dressed quark propagator

$$S = \frac{1}{i\gamma_\nu \partial^\nu - i\gamma_0 A_4 - \hat{M}} \tag{2.9}$$

with the effective-quark-mass matrix $\hat{M} = {\rm diag}(M, M)$ satisfying $M = m_0 - 2G_{\rm S}(\Phi)\sigma$ and the mesonic potential $U_{\rm M} = G_{\rm S}(\Phi)\sigma^2$. The variable σ means the chiral condensate: $\sigma = \langle\bar{\psi}\psi\rangle$. Making the path integral over the quark

field, one can get the thermodynamic potential (per unit volume) as

$$\begin{aligned}\Omega_{\rm EPNJL}(\sigma,\Phi,\bar{\Phi},T) = U_{\rm M} + \mathcal{U} - 2N_{\rm f}\int\frac{d^3\boldsymbol{p}}{(2\pi)^3}\Big[3E_{\boldsymbol{p}} \\ + \frac{1}{\beta}\ln\ [1+3(\Phi+\bar{\Phi}e^{-\beta E_{\boldsymbol{p}}})e^{-\beta E_{\boldsymbol{p}}}+e^{-3\beta E_{\boldsymbol{p}}}] \\ + \frac{1}{\beta}\ln\ [1+3(\bar{\Phi}+\Phi e^{-\beta E_{\boldsymbol{p}}})e^{-\beta E_{\boldsymbol{p}}}+e^{-3\beta E_{\boldsymbol{p}}}]\Big] \qquad (2.10)\end{aligned}$$

with $\beta = 1/T$, $E_{\boldsymbol{p}} = \sqrt{\boldsymbol{p}^2 + M^2}$ and the number $N_{\rm f}$ of flavors. Mean-field variables (σ, Φ and $\bar{\Phi}$) are determined to minimize $\Omega_{\rm EPNJL}$.

The mesonic current corresponding to $\xi = \pi$ or σ meson is

$$J_\xi(x) = \bar{\psi}(x)\Gamma_\xi\psi(x) - \langle\bar{\psi}(x)\Gamma_\xi\psi(x)\rangle, \qquad (2.11)$$

where the matrix Γ_ξ has the color, flavor and Dirac indices. The matrix Γ_ξ is $\Gamma_\xi = \boldsymbol{I}_{\rm C}\otimes\boldsymbol{I}_{\rm D}\otimes\boldsymbol{I}_{\rm F}$ for $\xi = \sigma$ and $\Gamma_\xi = \boldsymbol{I}_{\rm C}\otimes i\gamma_5\otimes\tau_3$ for $\xi = \pi$, where $\boldsymbol{I}_{\rm C}, \boldsymbol{I}_{\rm D}$ and $\boldsymbol{I}_{\rm F}$ are the unit matrices in color, Dirac and flavor spaces, respectively. The mesonic correlation function $\zeta_{\xi\xi}(t,\boldsymbol{x})$ in coordinate space $x = (t,\boldsymbol{x})$ is defined by

$$\zeta_{\xi\xi}(t,\boldsymbol{x}) \equiv \langle 0|{\rm T}\left(J_\xi(x)J_\xi^\dagger(0)\right)|0\rangle, \qquad (2.12)$$

where the symbol T stands for the time-ordered product. The mesonic correlation function $\chi_{\xi\xi}(q_0^2,\boldsymbol{q}^2)$ in momentum space $q = (q_0,\boldsymbol{q})$ is obtained as the Fourier transformation of $\zeta_{\xi\xi}(t,\boldsymbol{x})$:

$$\chi_{\xi\xi}(q_0^2,\boldsymbol{q}^2) = i\int d^4x\ e^{iq\cdot x}\zeta_{\xi\xi}(t,\boldsymbol{x}). \qquad (2.13)$$

Using the random-phase (ring) approximation, one can obtain the Schwinger-Dyson equation

$$\chi_{\xi\xi}(q_0^2,\boldsymbol{q}^2) \ = \ \Pi_{\xi\xi}(q_0^2,\boldsymbol{q}^2) + 2G_{\rm S}(\Phi)\Pi_{\xi\xi}(q_0^2,\boldsymbol{q}^2)\chi_{\xi\xi}(q_0^2,\boldsymbol{q}^2) \qquad (2.14)$$

for $\chi_{\xi\xi}(q_0^2,\boldsymbol{q}^2)$, where the one-loop polarization function $\Pi_{\xi\xi}(q_0^2,\boldsymbol{q}^2)$ is defined as

$$\Pi_{\xi\xi}(q_0^2,\boldsymbol{q}^2) \ \equiv \ (-i)\int\frac{d^4p}{(2\pi)^4}{\rm tr}_{\rm c,f,d}\left(\Gamma_\xi iS(p'+q)\Gamma_\xi iS(p')\right) \qquad (2.15)$$

with $p' = (p_0 + iA_4, \boldsymbol{p})$ and the dressed quark propagator $S(p)$ in the Hartree approximation. The trace ${\rm tr}_{\rm c.f.d}$ is taken in color, flavor and Dirac spaces. The solution to Eq. (2.14) is

$$\chi_{\xi\xi} \ = \ \frac{\Pi_{\xi\xi}}{1-2G_{\rm S}(\Phi)\Pi_{\xi\xi}}. \qquad (2.16)$$

The $\Pi_{\xi\xi}$ are explicitly obtained by

$$\begin{aligned}\Pi_{\sigma\sigma} &= i\int\frac{d^4p}{(2\pi)^4}\mathrm{Tr}\Big[\frac{\{\gamma_\mu(p'+q)^\mu+M\}(\gamma_\nu p'^\nu+M)}{\{(p'+q)^2-M^2\}(p'^2-M^2)}\Big]\\ &= 2iN_{\mathrm{f}}[I_1+I_2-(q^2-4M^2)I_3], \qquad (2.17)\\ \Pi_{\pi\pi} &= i\int\frac{d^4p}{(2\pi)^4}\mathrm{Tr}\Big[(i\gamma_5\tau^a)\frac{\{\gamma_\mu(p'+q)^\mu+M\}}{\{(p'+q)^2-M^2\}}\times(i\gamma_5\tau^a)\frac{(\gamma_\nu p'^\nu+M)}{(p'^2-M^2)}\Big]\\ &= 2iN_{\mathrm{f}}[I_1+I_2-q^2I_3], \qquad (2.18)\end{aligned}$$

with

$$\begin{aligned}I_1 &= \int\frac{d^4p}{(2\pi)^4}\mathrm{tr_c}\Big[\frac{1}{p'^2-M^2}\Big], \qquad (2.19)\\ I_2 &= \int\frac{d^4p}{(2\pi)^4}\mathrm{tr_c}\Big[\frac{1}{(p'+q)^2-M^2}\Big], \qquad (2.20)\\ I_3 &= \int\frac{d^4p}{(2\pi)^4}\mathrm{tr_c}\Big[\frac{1}{\{(p'+q)^2-M^2\}(p'^2-M^2)}\Big], \qquad (2.21)\end{aligned}$$

where trace $\mathrm{tr_c}$ means the trace of color matrix. For finite T, the corresponding equations are obtained by the replacement

$$\begin{aligned}&p_0\to i\omega_n=i(2n+1)\pi T,\\ &\int\frac{d^4p}{(2\pi)^4}\to iT\sum_{n=-\infty}^{\infty}\int\frac{d^3\boldsymbol{p}}{(2\pi)^3}. \qquad (2.22)\end{aligned}$$

In this thesis, we refer to the summation over n as "Matsubara summation" and the integral over $\boldsymbol{p}$ as "internal-momentum integration".

We need to regularize the momentum $\boldsymbol{p}$ integrals in the thermodynamic potential Ω_{EPNJL} of Eq. (2.10) and in the three functions I_1, I_2, I_3. Usually, the three-dimensional momentum-cutoff regularization

$$\int\frac{d^3\boldsymbol{p}}{(2\pi)^3}\to\int_{|\boldsymbol{p}|\le\Lambda}\frac{d^3\boldsymbol{p}}{(2\pi)^3} \qquad (2.23)$$

is taken in NJL-type effective models, where Λ is a cutoff parameter. However, the regularization breaks Lorentz invariance. In this thesis, we take the Pauli-Villars (PV) regularization [32] that preserves Lorentz invariance. The original version of PV regularization breaks chiral symmetry explicitly, since the regularization introduces auxiliary particles with heavy masses. In addition, we cannot take their masses infinity, because the present model is nonrenormalizable. This problem is solved by E. Ruiz Arriola and L.L. Salcedo in Ref. [33].

Here we explain the PV regularization for the thermodynamic potential Ω_{EPNJL} and the three functions I_1, I_2, I_3. For convenience, we divide Ω_{EPNJL} into $\Omega_{\mathrm{EPNJL}} = U_{\mathrm{M}} + \mathcal{U} + N_{\mathrm{f}}\Omega_{\mathrm{F}}(M)$, and represent I_1 and I_2 by $I(M)$ and

I_3 by $I_3(M)$. In the PV scheme, the functions $\Omega_{\rm F}(M)$, $I(M)$ and $I_3(M)$ are regularized as

$$\begin{aligned}
\Omega_{\rm F}^{\rm reg}(M) &= \sum_{\alpha=0}^{2} C_\alpha \Omega_{\rm F}(M_\alpha), \\
I^{\rm reg}(M) &= \sum_{\alpha=0}^{2} C_\alpha I(M_\alpha), \\
I_3^{\rm reg}(M) &= \sum_{\alpha=0}^{2} C_\alpha I_3(M_\alpha),
\end{aligned} \tag{2.24}$$

where $M_0 = M$ and the M_α ($\alpha = 1, 2$) mean masses of auxiliary particles. The parameters M_α and C_α should satisfy the condition

$$\sum_{\alpha=0}^{2} C_\alpha = 0, \ \sum_{\alpha=0}^{2} C_\alpha M_\alpha^2 = 0 \tag{2.25}$$

to remove the quartic, the quadratic and the logarithmic divergence in I_1, I_2, I_3, and $\Omega_{\rm F}$. We assume $(C_0, C_1, C_2) = (1, 1, -2)$ and $(M_1^2, M_2^2) = (M^2 + 2\Lambda^2, M^2 + \Lambda^2)$, following Ref. [34]. We keep the parameter Λ finite even after the subtraction (2.24), since the present model is non-renormalizable. In the present parameterization, logarithmic divergence partially remains in $\Omega_{\rm F}^{\rm reg}(M)$ even after the subtraction (2.24), but the term does not depend on the mean-field variables $(\sigma, \Phi, \bar{\Phi})$ and is irrelevant to the determination of mean-field variables for any T. Therefore we can simply drop the term.

2.3 Difficulty of screening-mass calculations

The NJL-type effective models are very useful. In fact, meson pole masses have been predicted by the models, particularly for light scalar and pseudoscalar mesons. In contrast, the evaluation of meson screening masses was quite difficult. The difficulty comes from the following two problems. One is that the NJL-type models are nonrenormalizable and thereby the regularization is necessary in the model calculations. So far, the three-dimensional momentum-cutoff regularization (2.23) was often taken. However, the regularization breaks Lorentz invariance. As a result of this breaking, the spatial correlation function $\zeta_{\xi\xi}(0, \boldsymbol{x})$ has unphysical oscillations [35]. This makes it quite difficult to determine meson screening mass ($M_\xi^{\rm scr}$) from the exponential decay of $\zeta_{\xi\xi}(0, \boldsymbol{x})$ at large distance ($r = |\boldsymbol{x}|$):

$$M_\xi^{\rm scr} \equiv -\lim_{r\to\infty} \frac{d \ln \zeta_{\xi\xi}(0, \boldsymbol{x})}{dr}. \tag{2.26}$$

Another problem is difficulty of the Fourier transformation

$$\zeta_{\xi\xi}(0, \boldsymbol{x}) = \int \frac{d^3\boldsymbol{q}}{(2\pi)^3} \chi_{\xi\xi}(0, \boldsymbol{q}^2) e^{i\boldsymbol{q}\cdot\boldsymbol{x}} = \frac{1}{4\pi^2 ir} \int_{-\infty}^{\infty} d\tilde{q}\ \tilde{q} \chi_{\xi\xi}(0, \tilde{q}^2) e^{i\tilde{q}r}\ , \tag{2.27}$$

where $\tilde{q} = \pm|\boldsymbol{q}|$. In the model approach, the correlation function $\chi_{\xi\xi}(0, \tilde{q}^2)$ is calculated first in momentum space and is Fourier transformed to the function $\zeta_{\xi\xi}(0, \boldsymbol{x})$ in coordinate space. In the integrand of Eq.(2.27), $\tilde{q}\chi_{\xi\xi}(0, \tilde{q}^2)$ is slowly damping with $\tilde{q}$, whereas $e^{i\tilde{q}r}$ is highly oscillatory particularly at large r where $M_\xi^{\rm scr}$ is determined. This property makes direct numerical calculations difficult. In general, this problem is avoidable with contour integral in complex-$\tilde{q}$ plane. However, the contour integral is still difficult because unphysical cuts are present in the vicinity of the real axis [35]; see the left panel of Fig. 2.1, where the limit of $\epsilon \to 0$ should be taken after the Fourier transformation.

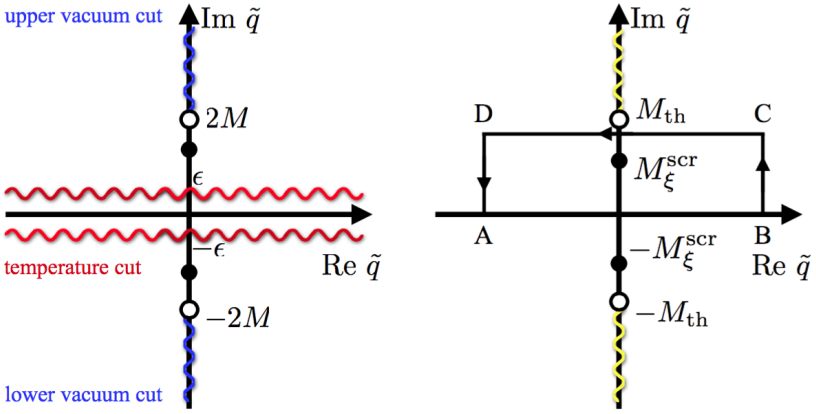

Fig. 2.1: Singularities of $\chi_{\xi\xi}(0, \tilde{q}^2)$ in the complex-$\tilde{q}$ plane based on the previous formulation [35] (left) and the present formulation (right). The wavy lines denote cuts and the open points represent the branch points of cuts. The closed points correspond to poles.

2.4 Meson screening mass in EPNJL model

The meson screening mass $M_\xi^{\rm scr}$ is determined from the exponential damping of $\zeta_{\xi\xi}(0, \boldsymbol{x})$ that is the Fourier transform of $\chi_{\xi\xi}(0, \tilde{q}^2)$, as shown in Eq. (2.27). In the previous formalism [35], however, heavy numerical calculations are required in the Fourier transform. We first explain the difficulty in the previous formalism [35]. After making the PV regularization and taking Matsubara (n) summation before the $\boldsymbol{p}$ integral in Eq. (2.22), the function $I_3^{\rm reg}(0, \tilde{q}^2)$ in $\chi_{\xi\xi}(0, \tilde{q}^2)$ contains a term $I_3^{\rm reg} = I_{3,\rm vac}^{\rm reg} + I_{3,\rm tem}^{\rm reg}$ defined by

$$I_{3,\rm vac}^{\rm reg}(0, \tilde{q}^2) = \frac{-iN_c}{16\pi^2} \sum_{\alpha=0}^{2} C_\alpha \left[\ln M_\alpha^2 + f_{\rm vac}\left(\frac{2M_\alpha}{\tilde{q}}\right)\right], \tag{2.28}$$

$$f_{\rm vac}(x) = \sqrt{1+x^2} \ln\left(\frac{\sqrt{1+x^2}+1}{\sqrt{1+x^2}-1}\right) \tag{2.29}$$

and

$$I^{\rm reg}_{3,{\rm tem}}(0,\tilde{q}^2) = \frac{iN_c}{16\pi^2}\sum_{\alpha=0}^{2} C_\alpha \int_0^\infty dp\ f_{\rm tem}(p,\tilde{q})\left(F_p^- + F_p^+\right), \tag{2.30}$$

$$f_{\rm tem}(p,\tilde{q}) = \frac{1}{E_p}\frac{p}{\tilde{q}}\ln\left(\frac{(\tilde{q}-2p)^2+\epsilon^2}{(\tilde{q}+2p)^2+\epsilon^2}\right), \tag{2.31}$$

where the Fermi distribution functions $F_p^\pm$ are defined as

$$F_p^\pm = \frac{1}{N_c}\sum_{j=1}^{N_{\rm c}} \frac{1}{\exp\left[\beta(E_p \pm iA_4^{jj})\right]+1} \tag{2.32}$$

with number $N_{\rm c}$ of colors. In Eq. (2.31), the ϵ^2 term is added to make the p integral well-defined at $\tilde{q} = \pm 2p$, but this requires the limit of $\epsilon \to 0$ finally. As shown in the left panel of Fig. 2.1, $f_{\rm vac}(2M_\alpha/\tilde{q})$ has the vacuum cuts and $f_{\rm tem}(p,\tilde{q})$ possesses temperature cuts in the complex $\tilde{q}$ plane. In the upper-half plane where contour integral is performed, the cuts contribute to the $\tilde{q}$ integral in addition to the pole at $\tilde{q} = iM_\xi^{\rm scr}$ determined by

$$\left[1 - 2G_{\rm S}(\Phi)\Pi_{\xi\xi}(0,\tilde{q}^2)\right]\big|_{\tilde{q}=iM_\xi^{\rm scr}} = 0. \tag{2.33}$$

It is not easy to evaluate the temperature-cut contribution, since in Eq. (2.27) the integrand is slowly damping and highly oscillating with $\tilde{q}$ near the real axis in the complex $\tilde{q}$ plane. Furthermore we have to take the limit of $\epsilon \to 0$ finally.

The problem mentioned above can be solved by taking the n summation after making the $\boldsymbol{p}$ integral, as shown below. Following this procedure, we get $I_3^{\rm reg}(0,\tilde{q}^2)$ as an n-summation of analytic functions:

$$\begin{aligned} I_3^{\rm reg}(0,\tilde{q}^2) &= \frac{iT}{2\pi^2}\sum_{j=1}^{N_{\rm c}}\sum_{n=-\infty}^{\infty}\sum_{\alpha=0}^{2} C_\alpha \int_0^1 dx \int_0^\infty d\tilde{k}\frac{\tilde{k}^2}{[\tilde{k}^2 + (x-x^2)\tilde{q}^2 + M_{j,n,\alpha}^2]^2} \\ &= \frac{iT}{4\pi\tilde{q}}\sum_{j,n,\alpha} C_\alpha \sin^{-1}\left(\frac{\frac{\tilde{q}}{2}}{\sqrt{\frac{\tilde{q}^2}{4}+M_{j,n,\alpha}^2}}\right) \end{aligned} \tag{2.34}$$

with

$$M_{j,n,\alpha}(T) = \sqrt{M_\alpha^2 + \{(2n+1)\pi T + A_4^{jj}\}^2}. \tag{2.35}$$

We have numerically checked that the convergence of the n summation is quite fast in Eq. (2.34). In the upper-half plane, each term of $I_3^{\rm reg}(0,\tilde{q}^2)$ has a cut starting from $2iM_{j,n,\alpha}$ on the imaginary axis. The cut is shown in the right panel of Fig. 2.1. The lowest branch point is

$$\tilde{q} = iM_{\rm th} \equiv 2iM_{j=1,n=0,\alpha=0} \tag{2.36}$$

Hence $M_{\rm th}$ is regarded as "threshold mass", because that the meson screening-mass spectrum becomes continuous above the point.

When $M_\xi^{\rm scr} < M_{\rm th}$, the pole at $\tilde{q} = iM_\xi^{\rm scr}$ is isolated from the cut well. This means that one can take the contour (A→B→C→D→A) shown in the right panel of Fig. 2.1. The $\tilde{q}$ integral of $\tilde{q}\chi_{\xi\xi}(0,\tilde{q}^2)e^{i\tilde{q}r}$ on the real axis in Eq. (2.27) is then obtainable from the residue at the pole and the line integral from point C to point D. The former behaves as $\exp[-M_\xi^{\rm scr}r]/r$ at large r and the latter as $\exp[-M_{\rm th}r]/r$. The behavior of $\zeta_{\xi\xi}(0,\boldsymbol{x})$ at large $r = |\boldsymbol{x}|$ is thus determined by the pole. Therefore, we can evaluate the screening mass from the location of the pole in the complex-$\tilde{q}$ plane without performing the $\tilde{q}$ integral. In the high-T limit, the threshold mass tends to $2\pi T$. This result is consistent with that of perturbative QCD [36].

2.5 Numerical Results

First, we show that the EPNJL model with PV regularization well describes the chiral symmetry restoration. As already mentioned in Sec. 2.2, the original version of PV regularization breaks chiral symmetry explicitly, since the regularization introduces auxiliary particles with heavy masses. This problem is solved in Ref. [33] and NJL model with the improved PV-regularization well describes empirical value of chiral condensate at $T = 0$ in Ref. [37]. We should check whether the PV regularization also works at finite T. We analyze 2-flavor LQCD data on the chiral condensate of Ref. [38] and the Polyakov loop of Ref. [39] by using the EPNJL model with the PV regularization. In model calculations, we have three adjustable parameters T_0, α_1 and α_2. We determine these parameters so as to reproduce pseudocritical temperature $T_c^{\rm deconf,2f} \approx 173 \pm 8$ MeV of the deconfinement transition. The EPNJL model with the PV regularization yields the same quality of agreement with the LQCD data as the EPNJL model with the three-dimensional momentum-cutoff regularization [26].

The pion screening mass $M_\pi^{\rm scr}$ obtained by state-of-the-art *2+1 flavor*-LQCD simulations [30] is well analyzed by the present *2-flavor* EPNJL model simply, since the meson is composed of u and d quarks only and has no s-quark component. In the LQCD simulations [30], the chiral transition temperature is $T_c^{\chi,\rm 3f} = 196$ MeV, although it is $T_c^{\chi,\rm 3f} = 154 \pm 9$ MeV in finer 2+1-flavor LQCD simulations [40,41] close to the continuum limit. Therefore, we rescale the LQCD results of Ref. [30] with a factor 154/196 in order to reproduce $T_c^{\chi,\rm 3f} = 154 \pm 9$ MeV. The model parameters, m_0 and T_0, are refitted so as to reproduce the rescaled 2+1-flavor LQCD data, i.e., $M_\pi = 175$ MeV at vacuum and $T_c^{\chi,\rm 3f} = 154 \pm 9$ MeV; the resulting values are $m_0 = 10.3$ MeV and $T_0 = 156$ MeV. The variation of m_0 from the original value 6.3 MeV to 10.3 MeV little changes the values of σ and Φ.

As shown in Fig. 2.3, the $M_\pi^{\rm scr}$ calculated with the EPNJL model (solid line) well reproduces the LQCD results (open circles), when $\alpha_1 = \alpha_2 = 0.31$. In the PNJL model with $\alpha_1 = \alpha_2 = 0$, the model result (dotted line) largely

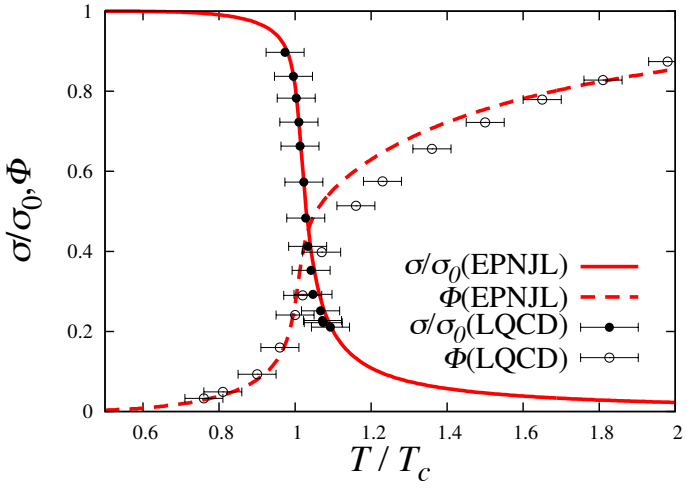

Fig. 2.2: T dependence of chiral condensate and Polyakov loop in the 2-flavor system. In model calculations, we use $T_0 = 200$ MeV and $\alpha_1 = \alpha_2 = 0.2$. LQCD data are taken from Ref. [38] for the chiral condensate and Ref. [39] for the Polyakov loop. The chiral condensates are normalized by the zero temperature value σ_0.

underestimates the LQCD results, indicating that the entangle coupling is important. The dashed line denotes the sigma-meson screening mass $M_\sigma^{\rm scr}$ obtained by the EPNJL model with $\alpha_1 = \alpha_2 = 0.31$. The solid and dashed lines are lower than the threshold mass $M_{\rm th}$ (dot-dashed line). This ensures that the $M_\pi^{\rm scr}$ and $M_\sigma^{\rm scr}$ determined from the location of the single pole in the complex-$\tilde{q}$ plane agree with those from the exponential decay of $\zeta_{\xi\xi}(0, \boldsymbol{x})$ at large r. The chiral restoration takes place at $T \approx T_c^{\chi\text{-}3{\rm f}} = 154$ MeV, since $M_\pi^{\rm scr} = M_\sigma^{\rm scr}$ there. After the restoration, the screening masses rapidly approach the threshold mass and finally $2\pi T$. The threshold mass is thus an important concept to understand T dependence of screening masses.

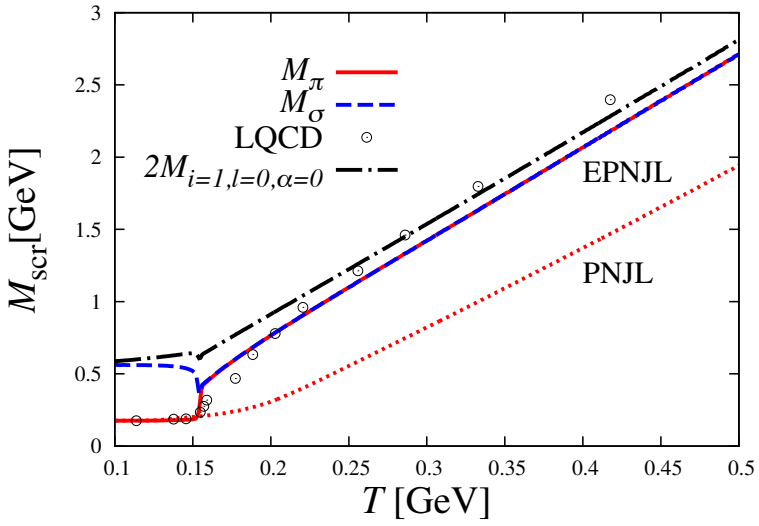

Fig. 2.3: T dependence of pion and sigma-meson screening masses. In model calculations, we use $T_0 = 156$ MeV for the PNJL and EPNJL models. The parameters α_1 and α_2 in the EPNJL model are set to $\alpha_1 = \alpha_2 = 0.31$. LQCD data are taken from Ref. [30] for pion screening mass. $M_\pi^{\rm scr}$ and $M_\sigma^{\rm scr}$ calculated by the EPNJL model are denoted by the solid and dashed lines, respectively, whereas $M_\pi^{\rm scr}$ calculated with the PNJL model is shown by the dotted line. The $M_\pi^{\rm scr}$ obtained by 2+1-flavor LQCD simulations are denoted by the open circles. The dot-dashed line stands for the threshold mass.

2.6 Short Summary

We have proposed a practical method of calculating meson screening masses $M_\xi^{\rm scr}(T)$ in NJL-type effective models. The method is based on the following two procedures:

(1) The PV regularization,

(2) A new prescription of calculating the spatial correlation function for meson screening mass.

In the three-dimensional momentum cutoff regularization commonly used, artificial oscillations appear in the spatial mesonic correlation function, since the regularization breaks Lorentz invariance in momentum space. In the PV regularization taken in this thesis, such artificial oscillations do not appear, because the PV regularization possesses Lorentz invariance.

In the previous formalism [35] for the correlation function $\zeta_{\xi\xi}(0, \boldsymbol{x})$ in coordinate $\boldsymbol{x}$ space, it is calculated by Fourier transformation from the correlation function $\chi_{\xi\xi}(0, \tilde{q}^2)$ in momentum $\tilde{q}$ space. However, the Fourier transformation is quite difficult, because it demands $\tilde{q}$ integration of highly oscillating function in the long distance limit ($|\boldsymbol{x}| \to \infty$) where the meson

screening mass is evaluated. In principle, we can avoid the difficulty by performing the Fourier transformation as a contour integral in the complex-$\tilde{q}$ plane. In the previous formalism [35] where the Matsubara summation is taken before the internal-momentum integration in the Fourier transformation, temperature cuts appear near the real-$\tilde{q}$ axis in the complex-$\tilde{q}$ plane and the evaluation of the cuts still demands heavy numerical calculations. In our formalism, *we take the Matsubara summation after the internal-momentum integration* in the Fourier transformation, and thereby such temperature cuts do not appear. Cuts and a pole appearing in our formalism are located only on the imaginary-$\tilde{q}$ axis in the complex-$\tilde{q}$ plane. We can then obtain the meson screening mass as a pole of $\chi_{\xi\xi}(0, \tilde{q}^2)$, when the pole is located below the cuts. The lowest branch point can be regarded as the threshold mass $M_{\rm th}(T)$. Therefore, we can easily evaluate the meson screening mass $M_\xi^{\rm scr}(T)$ when $M_\xi^{\rm scr}(T) < M_{\rm th}(T)$.

First, we have proposed the new version of EPNJL model that is based on the PV regularization instead of the three-dimensional momentum-cutoff regularization commonly used. We have then applied the prescription (2) to the EPNJL model in order to analyze T dependence of pion and sigma-meson screening masses and shown that the model well explains recent 2+1 flavor LQCD results on T dependence of pion screening mass and the value of $T_c^{\chi,{\rm 3f}}$, when $\alpha_1 = \alpha_2 = 0.31$ and $T_0 = 156$ MeV.

Chapter 3

$U(1)_{\rm A}$ symmetry restoration

We consider the effective $U(1)_{\rm A}$-symmetry restoration with the 2+1-flavor EPNJL model. For this purpose, T dependence is introduced for the coupling strength K of the Kobayashi-Maskawa-'t Hooft (KMT) determinant interaction: $K = K(T)$. The $K(T)$ is determined from state-of-the-art LQCD results on T dependence of screening masses for pion and its $U(1)_{\rm A}$ partner (a_0 meson). The $K(T)$ thus obtained is strongly suppressed in the vicinity of the pseudocritical temperature of chiral transition. The EPNJL model with the $K(T)$ well reproduces meson susceptibilities calculated by LQCD simulations. By using this reliable model, we predict light-quark mass (m_l) and strange-quark mass (m_s) dependence of chiral transition particularly around the physical point $(m_l, m_s) = (6.2\ \text{MeV}, 175\ \text{MeV})$. We show that the chiral transition is the second order at the "light-quark chiral-limit" point $(m_l, m_s) = (0\ \text{MeV}, 175\ \text{MeV})$. We find that a tricritical point appears in the southwest direction from the physical point. The location we find is $(m_l, m_s) = (0\ \text{MeV}, 127\ \text{MeV})$.

3.1 $U(1)_{\rm A}$ symmetry and Columbia plot

As already mentioned in Sec. 1.1.3, global $U(1)_{\rm A}$ symmetry is explicitly broken by the quantum anomaly through the topologically nontrivial gauge configurations (instantons and antiinstantons). At high T, instanton density ($dn_{\rm inst}(T)$) is suppressed by Debye screening in the medium. Pisarski and Yaffe calculated the suppression $S(T) \equiv dn_{\rm inst}(T)/dn_{\rm inst}(0)$ perturbatively in high T [42], say $T \gtrsim 2T_c^\chi$ for the pseudocritical temperature T_c^χ of chiral transition, and $S(T)$ was obtained by

$$\begin{aligned} S(T) &= \exp\Big[-\pi^2\rho^2 T^2 \Big(\frac{2}{3}N_c + \frac{1}{3}N_f\Big)\Big] \\ &= \exp[-T^2/b^2] \end{aligned} \tag{3.1}$$

with the instanton radius ρ. The typical value of ρ is about 1/3 fm, and hence the suppression parameter b is about $0.70T_c^\chi$ for $N_c = N_f = 3$ of

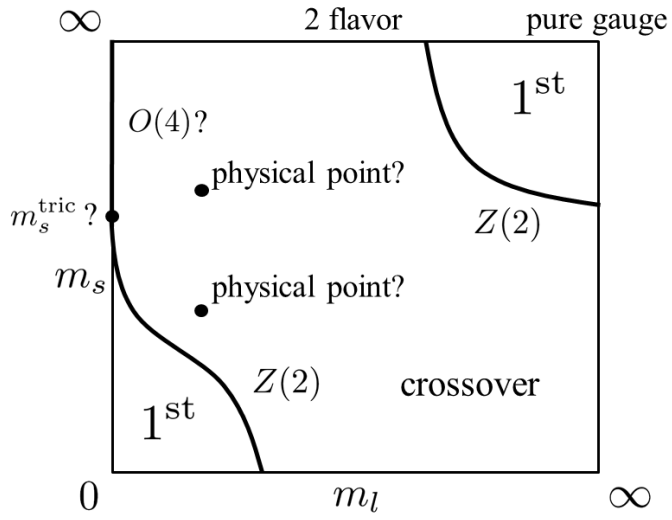

Fig. 3.1: A schematic phase diagram of 2+1-flavor QCD as a function of light-quark mass m_l and strange-quark mass m_s (Columbia plot). A tricritical point may appear on the m_s axis; the location is shown by $(m_l, m_s) = (0, m_s^{\rm tric})$. The solid lines denote second-order transitions belonging to the universality class labeled, where the labels $Z(2)$ and $O(4)$ represent the 3d Ising and the 3d $O(4)$ class, respectively.

our interest [43]; note that 2+1-flavor LQCD simulations show $T_c^\chi = 154 \pm 9$ MeV [40, 41, 44]. The suppression $S(T)$ in Eq. (3.1) is stronger as T increases, and consequently global $U(1)_{\rm A}$ symmetry is effectively restored at higher T in the vacuum expectation value. This phenomenon is called "effective restoration of $U(1)_{\rm A}$ symmetry", since $U(1)_{\rm A}$ symmetry is always broken in the current-operator level as shown in Eq. (1.23).

Figure 3.1 shows the current status of our knowledge on the 2+1-flavor phase diagram as a function of light-quark mass m_l and strange-quark mass m_s. The phase diagram is usually called "Columbia plot". The lower left (upper right) corner corresponds to QCD in the massless limit (pure Yang–Mills limit), and QCD shows a first-order phase transition associated with the breaking of chiral (Z_3) symmetry there [45, 46]. Varying m_l and m_s, we can see that these first-order transitions become second order of 3d Ising ($Z(2)$) universality class, as shown by the solid lines [45, 46].

However, the order of chiral transition and its universality class has not been determined on the vertical line of $m_l = 0$ and $m_s > 0$, and it is considered to be related to the correlation between the $U(1)_{\rm A}$- and chiral-symmetry restorations. In the two-flavor chiral limit of $(m_l, m_s) = (0, \infty)$ at the upper left corner, for example, the order may be second order belonging to $O(4)$ class if the $U(1)_{\rm A}$ symmetry is broken at $T = T_c^\chi$, since $U(2)_{\rm R} \times U(2)_{\rm L}$

symmetry is broken into $SU(2)_{\rm L} \times SU(2)_{\rm R}$ isomorphic to $O(4)$ in the situation and the transition is then expected to be in the 3d $O(4)$ universality class [45,46]. When $U(1)_{\rm A}$ and chiral symmetries are restored simultaneously at $T = T_c^{\chi}$, it was suggested in Ref. [45] that the chiral transition becomes the first order. Recently, however, it was pointed out in Ref. [47] that the second order is still possible. In this case, the transition belongs to not $O(4)$ but $U(2)_{\rm L} \times U(2)_{\rm R}$ universality class. Many LQCD simulations were made so far to clarify the order and its universality class in the two-flavor chiral limit of $(m_l, m_s) = (0, \infty)$ and the light-quark chiral limit where m_l vanishes with m_s fixed at the physical value, but these are still controversial; see Refs. [48–59].

Very recently, the effective restoration of $U(1)_{\rm A}$ symmetry was studied with state-of-the-art LQCD simulations by analyzing T dependence of pion and a_0-meson screening masses [30] and also by meson susceptibilities [60,61]. The effective restoration of $U(1)_{\rm A}$ symmetry thus becomes an important current issue.

3.2 Model setting

3.2.1 EPNJL model

We consider the 2+1-flavor EPNJL model [25, 26]. The Lagrangian density in Minkowski space is

$$\begin{aligned}\mathcal{L} =& \bar{\psi}(i\gamma_\nu D^\nu - \hat{m}_0)\psi + G_{\rm S}(\Phi)\sum_{a=0}^{8}[(\bar{\psi}\lambda_a\psi)^2 + (\bar{\psi}i\gamma_5\lambda_a\psi)^2] \\ & - K(T)\Big[\det_{f,f'}\bar{\psi}_f(1+\gamma_5)\psi_{f'} + \det_{f,f'}\bar{\psi}_f(1-\gamma_5)\psi_{f'}\Big] \\ & - \mathcal{U}(\Phi[A], \bar{\Phi}[A], T), \end{aligned} \tag{3.2}$$

where $D^\nu = \partial^\nu + iA^\nu$ with $A^\nu = \delta^\nu_0 g(A^0)_a t_a/2 = -\delta^\nu_0 ig(A_4)_a t_a/2$ for the gauge coupling g, the vector $\psi = (\psi_u, \psi_d, \psi_s)^{\rm T}$ means quark fields, and the λ_a (t_a) are the Gell-Mann matrices in flavor (color) space and $\lambda_0 = \sqrt{2/3}\,\boldsymbol{I}_{\rm F}$ for the unit matrix $\boldsymbol{I}_{\rm F}$ in flavor space. The determinant in Eq. (3.2) is taken in flavor space. For the 2+1-flavor system, the current quark masses $\hat{m}_0 = {\rm diag}(m_u, m_d, m_s)$ satisfy the relation $m_s > m_l \equiv m_u = m_d$. In the EPNJL model, the coupling strength $G_{\rm S}(\Phi)$ of the scalar-type four-quark interaction depends on the Polyakov loop Φ and its Hermitian conjugate $\bar{\Phi}$ as

$$G_{\rm S}(\Phi) = G_{\rm S}(0)\left[1 - \alpha_1\Phi\bar{\Phi} - \alpha_2(\Phi^3 + \bar{\Phi}^3)\right]. \tag{3.3}$$

This entanglement coupling is invariant under the charge conjugation and the Z_3 transformation. When $\alpha_1 = \alpha_2 = 0$, the EPNJL model is reduced to the PNJL model. We set $\alpha_2 = 0$ for simplicity, since the α_2 term yields the same effect as the α_1 term in the present analysis. As shown later in Sec.

3.3, the value of α_1 is determined from LQCD data on pion and a_0-meson screening masses; the resulting value is $\alpha_1 = 1.0$.

The EPNJL model exhibits the $U(1)_{\rm A}$ anomaly through the Kobayashi-Maskawa-'t Hooft (KMT) determinant interaction with the coupling strength $K(T)$ [4, 62]. Here we assume that the coupling strength K of the KMT interaction is proportional to the instanton density, and hence K gets smaller as T increases: $K = K(T)$. For T dependence of $K(T)$, we consider the following form phenomenologically:

$$K(T) = \begin{cases} K(0) & (T < T_1) \\ K(0)e^{-(T-T_1)^2/b^2} & (T \geq T_1) \end{cases} . \tag{3.4}$$

For high T satisfying $T \gg T_1$, the form (3.4) is reduced to Eq. (3.1). As shown later in Sec. 3.3, the values of T_1 and b will be well determined from LQCD data on pion and a_0-meson screening masses; the resulting values are $T_1 = 0.79T_c^\chi = 121$ MeV and $b = 0.23T_c^\chi = 36$ MeV.

After the Pisarski-Yaffe discussion on $S(T)$, T dependence of the instanton density was estimated theoretically by the instanton-liquid model [43], but the estimation is applicable only for $T \gtrsim 2T_c^\chi$. For this reason, in Ref. [31], the Woods-Saxon form $(1 + e^{(T-T_1')/b'})^{-1}$ with two parameters T_1' and b' was used phenomenologically for $K(T)/K(0)$. The present form (3.4) has T dependence similar to the Woods-Saxon form.

In the EPNJL model, the time component of A_μ is treated as a homogeneous and static background field, which is mainly governed by the Polyakov-loop potential $\mathcal{U}$. In the Polyakov gauge, Φ and $\bar{\Phi}$ are obtained by

$$\Phi = \frac{1}{3}{\rm tr_c}(L), \qquad \bar{\Phi} = \frac{1}{3}{\rm tr_c}(L^*) \tag{3.5}$$

with $L = \exp[iA_4/T] = \exp[i{\rm diag}(A_4^{11}, A_4^{22}, A_4^{33})/T]$ for real variables A_4^{jj} satisfying $A_4^{11} + A_4^{22} + A_4^{33} = 0$. For zero quark chemical potential where $\Phi = \bar{\Phi}$, one can set $A_4^{33} = 0$ and determine the others as $A_4^{22} = -A_4^{11} = \cos^{-1}[(3\Phi - 1)/2]$.

We use the logarithm-type Polyakov-loop potential of Ref. [18] as $\mathcal{U}$. The parameter set in $\mathcal{U}$ has already been determined from LQCD data at finite T in the pure gauge limit. The potential has a parameter T_0 and yields a first-order deconfinement phase transition at $T = T_0$. The parameter used to be set to $T_0 = 270$ MeV, since LQCD data show the phase transition at $T = 270$ MeV in the pure gauge limit. In full QCD with dynamical quarks, however, the EPNJL model with this value of T_0 is found not to explain the LQCD results. Nowadays, T_0 is then rescaled to reproduce the LQCD results. In this chapter, we take $T_0 = 180$ MeV so that the present model can reproduce LQCD results on the pseudocritical temperature $T_c^{\rm deconf}$ of the deconfinement transition; actually, $T_c^{\rm deconf} = 165$ MeV in the present model, while $T_c^{\rm deconf} = 170 \pm 7$ MeV in LQCD [63].

Applying the mean-field approximation (MFA) for Eq. (3.2) leads to the linearized Lagrangian density

$$\mathcal{L}^{\rm MFA} = \bar{\psi} S^{-1} \psi - U_{\rm M} - \mathcal{U}(\Phi[A], \bar{\Phi}[A], T) \tag{3.6}$$

with the quark propagator

$$S = (i\gamma_\nu \partial^\nu - \gamma_0 A^0 - \hat{M})^{-1}, \tag{3.7}$$

where $\hat{M} = {\rm diag}(M_u, M_d, M_s)$ with

$$\begin{aligned} M_u &= m_u - 4G_{\rm S}(\Phi)\sigma_u + 2K(T)\sigma_d\sigma_s, \\ M_d &= m_d - 4G_{\rm S}(\Phi)\sigma_d + 2K(T)\sigma_s\sigma_u, \\ M_s &= m_s - 4G_{\rm S}(\Phi)\sigma_s + 2K(T)\sigma_u\sigma_d, \end{aligned}$$

and σ_f means the chiral condensate $\langle\bar{\psi}_f\psi_f\rangle$ for flavor f. The mesonic potential $U_{\rm M}$ is

$$U_{\rm M} = 2G_{\rm S}(\Phi)(\sigma_u^2 + \sigma_d^2 + \sigma_s^2) - 4K(T)\sigma_u\sigma_d\sigma_s.$$

Making the path integral over quark fields, one can get the thermodynamic potential (per unit volume) as

$$\begin{aligned} \Omega_{\rm EPNJL} = U_{\rm M} + \mathcal{U} - 2\sum_{f=u,d,s}\int\frac{d^3\boldsymbol{p}}{(2\pi)^3}\Big[3E_{\boldsymbol{p},f} \\ + \frac{1}{\beta}\ln\ [1 + 3(\Phi + \bar{\Phi}e^{-\beta E_{\boldsymbol{p},f})}e^{-\beta E_{\boldsymbol{p},f}} + e^{-3\beta E_{\boldsymbol{p},f}}] \\ + \frac{1}{\beta}\ln\ [1 + 3(\bar{\Phi} + \Phi e^{-\beta E_{\boldsymbol{p},f}})e^{-\beta E_{\boldsymbol{p},f}} + e^{-3\beta E_{\boldsymbol{p},f}}]\Big] \end{aligned} \tag{3.8}$$

with $E_{\boldsymbol{p},f} = \sqrt{\boldsymbol{p}^2 + M_f^2}$ and $\beta = 1/T$. Mean-field variables (σ_l, σ_s, Φ and $\bar{\Phi}$) are determined to minimize $\Omega_{\rm EPNJL}$, where isospin symmetry is assumed for the light-quark sector, i.e., $\sigma_l \equiv \sigma_u = \sigma_d$.

3.2.2 Mesonic correlation functions

We extend the formalism of Chapter 2 for pion and a_0-meson correlation functions from the 2-flavor system to the 2+1-flavor system. The current operator of ξ meson is

$$J_\xi(x) = \bar{\psi}(x)\Gamma_\xi\psi(x) - \langle\bar{\psi}(x)\Gamma_\xi\psi(x)\rangle, \tag{3.9}$$

where $\Gamma_\pi = i\gamma_5\lambda_3$ for π meson and $\Gamma_{a_0} = \lambda_3$ for a_0 meson. The mesonic correlation function $\zeta_{\xi\xi'}(t, \boldsymbol{x})$ in coordinate space $x = (t, \boldsymbol{x})$ is defined by

$$\zeta_{\xi\xi'}(t, \boldsymbol{x}) \equiv \langle 0|{\rm T}\left(J_\xi(t, \boldsymbol{x})J_{\xi'}^\dagger(0)\right)|0\rangle \tag{3.10}$$

and the corresponding mesonic correlation function $\chi_{\xi\xi'}(q_0^2, \tilde{q}^2)$ in momentum space $q = (q_0, \boldsymbol{q})$ is by

$$\chi_{\xi\xi'}(q_0^2, \tilde{q}^2) = i \int d^4x e^{iq\cdot x} \zeta_{\xi\xi'}(t, \boldsymbol{x}), \tag{3.11}$$

where $\tilde{q} = \pm|\boldsymbol{q}|$ and the operator T stands for the time-ordered product. Applying the random-phase (ring) approximation for $\chi_{\xi\xi'}$, we can get the Schwinger-Dyson equation

$$\chi_{\xi\xi'} = \Pi_{\xi\xi'} + 2 \sum_{\xi''\xi'''} \Pi_{\xi\xi''} G_{\xi''\xi'''} \chi_{\xi'''\xi'} \tag{3.12}$$

for $\chi_{\xi\xi'}$, where $G_{\xi\xi'}$ is the effective four-quark interaction and $\Pi_{\xi\xi'}$ is the one-loop polarization function defined by

$$\Pi_{\xi\xi'}(q_0^2, \tilde{q}^2) \equiv (-i) \int \frac{d^4p}{(2\pi)^4} \mathrm{tr}_{\mathrm{c,f,d}} \left(\Gamma_\xi i S(p'+q) \Gamma_{\xi'} i S(p') \right) \tag{3.13}$$

with $p' = (p_0 + iA_4, \boldsymbol{p})$, where the trace $\mathrm{tr}_{\mathrm{c,f,d}}$ is taken in color, flavor and Dirac spaces. Here the matrix $S(p)$ is the quark propagator in momentum space that is calculated from Eq. (3.7). For $\xi = \pi$ and a_0, the $G_{\xi\xi'}$ and $\Pi_{\xi\xi'}$ satisfy that $G_{\xi\xi'} = G_\xi \delta_{\xi\xi'}$ and $\Pi_{\xi\xi'} = \Pi_\xi \delta_{\xi\xi'}$, since isospin symmetry is assumed and the random phase approximation is taken. Because of these properties, we can easily solve the Schwinger-Dyson equation for $\xi = \pi$ and a_0. The solution is

$$\chi_{\xi\xi} = \frac{\Pi_\xi}{1 - 2G_\xi \Pi_\xi} \tag{3.14}$$

with the effective couplings G_π and G_{a_0} defined by

$$G_{a_0} = G_{\mathrm{S}}(\Phi) + \frac{1}{2} K(T) \sigma_s, \tag{3.15}$$

$$G_\pi = G_{\mathrm{S}}(\Phi) - \frac{1}{2} K(T) \sigma_s. \tag{3.16}$$

Taking the trace $\mathrm{tr}_{\mathrm{c,f,d}}$ for flavor and Dirac spaces in Eq. (3.13), we get the explicit forms of Π_π and Π_{a_0} as

$$\begin{aligned}
\Pi_{a_0} &= i \sum_{f,f'} (\lambda_3)_{f'f} (\lambda_3)_{ff'} \\
&\times \int \frac{d^4p}{(2\pi)^4} \mathrm{tr}_{\mathrm{c,d}} \Big[\frac{\{\gamma_\mu (p'+q)^\mu + M_f\} (\gamma_\nu p'^\nu + M_{f'})}{\{(p'+q)^2 - M_f^2\}(p'^2 - M_{f'}^2)} \Big] \\
&= 4i[I_1 + I_2 - (q^2 - 4M_l^2) I_3], \qquad (3.17) \\
\Pi_\pi &= i \sum_{f,f'} (\lambda_3)_{f'f} (\lambda_3)_{ff'} \\
&\times \int \frac{d^4p}{(2\pi)^4} \mathrm{tr}_{\mathrm{c,d}} \Big[(i\gamma_5) \frac{\{\gamma_\mu (p'+q)^\mu + M_f\}}{\{(p'+q)^2 - M_f^2\}} (i\gamma_5) \frac{(\gamma_\nu p'^\nu + M_{f'})}{(p'^2 - M_{f'})^2} \Big] \\
&= 4i[I_1 + I_2 - q^2 I_3], \qquad (3.18)
\end{aligned}$$

where the operator $\mathrm{tr}_{\rm c,d}$ means the trace in color and Dirac spaces. At $T=0$, the functions I_1, I_2 and I_3 are represented by

$$I_1 = \int \frac{d^4p}{(2\pi)^4}\mathrm{tr}_{\rm c}\Big[\frac{1}{p'^2-M_l^2}\Big], \tag{3.19}$$

$$I_2 = \int \frac{d^4p}{(2\pi)^4}\mathrm{tr}_{\rm c}\Big[\frac{1}{(p'+q)^2-M_l^2}\Big], \tag{3.20}$$

$$I_3 = \int \frac{d^4p}{(2\pi)^4}\mathrm{tr}_{\rm c}\Big[\frac{1}{\{(p'+q)^2-M_l^2\}(p'^2-M_l^2)}\Big], \tag{3.21}$$

where the operator $\mathrm{tr}_{\rm c}$ corresponds to the trace in color space and $M_l \equiv M_u = M_d$. When we consider the finite-T system, the replacements

$$p_0 \to i\omega_n = i(2n+1)\pi T,$$
$$\int \frac{d^4p}{(2\pi)^4} \to iT\sum_{n=-\infty}^{\infty}\int \frac{d^3\boldsymbol{p}}{(2\pi)^3} \tag{3.22}$$

should be taken in I_1, I_2 and I_3.

We then use the PV regularization [32,35], as already mentioned in Chapter 2. For convenience, we divide $\Omega_{\rm EPNJL}$ into $\Omega_{\rm EPNJL} = U_{\rm M}+\mathcal{U}+\sum_f \Omega_{\rm F}(M_f)$, and represent I_1 and I_2 by $I(M_l)$ and I_3 by $I_3(M_l)$. In the PV scheme, the functions $\Omega_{\rm F}(M_f)$, $I(M_l)$ and $I_3(M_l)$ are regularized as

$$\Omega_{\rm F}^{\rm reg}(M_f) = \sum_{\alpha=0}^{2} C_\alpha \Omega_{\rm F}(M_{f;\alpha}),$$
$$I^{\rm reg}(M_l) = \sum_{\alpha=0}^{2} C_\alpha I(M_{l;\alpha}),$$
$$I_3^{\rm reg}(M_l) = \sum_{\alpha=0}^{2} C_\alpha I_3(M_{l;\alpha}), \tag{3.23}$$

where $M_{f;0} = M_f$ and the $M_{f;\alpha}$ ($\alpha \geq 1$) mean masses of auxiliary particles. The parameters $M_{f;\alpha}$ and C_α should satisfy the condition $\sum_{\alpha=0}^{2} C_\alpha = \sum_{\alpha=0}^{2} C_\alpha M_{f;\alpha}^2 = 0$. In actual calculations, we then take $(C_0, C_1, C_2) = (1, 1, -2)$ and $(M_{f;1}^2, M_{f;2}^2) = (M_f^2 + 2\Lambda^2, M_f^2 + \Lambda^2)$. We keep the parameter Λ finite even after the subtraction (3.23), because the present model is non-renormalizable. For the parameters $m_l, m_s, G_{\rm S}(0), K(0)$ and Λ, we take those of Ref. [37]: $m_l = 6.2$ MeV, $m_s = 175.0$ MeV, $G_{\rm S}(0)\Lambda^2 = 2.35$ and $K(0)\Lambda^5 = 27.8$ for $\Lambda = 795$ MeV. This parameter set reproduces mesonic observables at $T=0$, i.e., the pion and kaon decay constants ($f_\pi = 92$ MeV and $f_K = 105$ MeV) and their masses ($M_\pi(0) = 141$ MeV and $M_K(0) = 512$ MeV) and the η'-meson mass ($M_{\eta'}(0) = 920$ MeV). In the present work, we analyze LQCD data of Ref. [30] for pion and a_0-meson screening masses. In the LQCD simulations, the pion mass $M_\pi(0)$ at vacuum ($T=0$) is 175 MeV and slightly larger than the experimental value 138 MeV. We then change m_l to 9.9 MeV in the EPNJL model in order to reproduce $M_\pi(0) = 175$ MeV.

3.2.3 Meson pole mass

The meson pole mass $M_\xi^{\rm pole}$ is a pole of $\chi_{\xi\xi}(q_0^2, \tilde{q}^2)$ in the complex q_0 plane. Taking the rest frame $q = (q_0, \mathbf{0})$ for convenience, one can get the equation for $M_\xi^{\rm pole}$ as

$$\left[1 - 2G_\xi \Pi_\xi(q_0^2, 0)\right]\Big|_{q_0 = M_\xi^{\rm pole} - i\Gamma_\xi/2} = 0, \tag{3.24}$$

where Γ_ξ is the decay width to quark-antiquark pair continuum. The method of solving Eq. (3.24) for $M_\xi^{\rm pole}$ and Γ_ξ has already been established in Ref. [8].

3.2.4 Meson screening mass

We derive the equations for pion and a_0-meson screening masses, following Chapter 2. This is an extension of the method from 2 flavors to 2+1 flavors.

As mentioned in Sec. 1, it is not easy to make the Fourier transform from $\chi_{\xi\xi}(0, \tilde{q}^2)$ to $\zeta_{\xi\xi}(0, \boldsymbol{x})$ particularly at large $r = |\boldsymbol{x}|$. When the direct integration on the real $\tilde{q}$ axis is difficult, in general we can consider a contour integral in the complex $\tilde{q}$ plane by using the Cauchy's integral theorem. However, $\chi_{\xi\xi}(0, \tilde{q}^2)$ has logarithmic cuts in the vicinity of the real $\tilde{q}$ axis [35], and heavy numerical calculations are necessary for evaluating the cut effects [35]. In our previous work [64] in Chapter 2, we showed that the logarithmic cuts are removable. Actually, our formulation has no logarithmic cut, because the Matsubara summation over n is taken after the $\boldsymbol{p}$ integration in Eq. (3.22). We then obtain $I_3^{\rm reg}(0, \tilde{q}^2)$ as an infinite series of analytic functions:

$$\begin{aligned} I_3^{\rm reg}(0, \tilde{q}^2) &= iT \sum_{j=1}^{N_c} \sum_{n=-\infty}^{\infty} \sum_{\alpha=0}^{2} C_\alpha \int \frac{d^3\boldsymbol{p}}{(2\pi)^3} \Big[\frac{1}{\boldsymbol{p}^2 + M_{j,n,\alpha}^2} \frac{1}{(\boldsymbol{p}+\boldsymbol{q})^2 + M_{j,n,\alpha}^2} \Big] \\ &= \frac{iT}{2\pi^2} \sum_{j,n,\alpha} C_\alpha \int_0^1 dx \int_0^\infty dk \frac{k^2}{[k^2 + (x - x^2)\tilde{q}^2 + M_{j,n,\alpha}^2]^2} \\ &= \frac{iT}{4\pi\tilde{q}} \sum_{j,n,\alpha} C_\alpha \sin^{-1}\Big(\frac{\frac{\tilde{q}}{2}}{\sqrt{\frac{\tilde{q}^2}{4} + M_{j,n,\alpha}^2}} \Big) \end{aligned} \tag{3.25}$$

with

$$M_{j,n,\alpha}(T) = \sqrt{M_\alpha^2 + \{(2n+1)\pi T + A_4^{jj}\}^2}, \tag{3.26}$$

where $M_\alpha \equiv M_{u;\alpha} = M_{d;\alpha}$. We have numerically confirmed that the convergence of n-summation is quite fast in Eq. (3.25). Each term of $I_3^{\rm reg}(0, \tilde{q}^2)$ has two physical cuts on the imaginary axis in the complex-$\tilde{q}$ plane. One is an upward vertical line starting from $\tilde{q} = 2iM_{j,n,\alpha}$ and the other is a downward vertical line from $\tilde{q} = -2iM_{j,n,\alpha}$. The lowest branch point is $\tilde{q} = 2iM_{j=1,n=0,\alpha=0}$ in the upper-half plane where we consider the contour integration. We call $2M_{j=1,n=0,\alpha=0}$ "the threshold mass $M_{\rm th}$".

We can obtain the meson screening mass $M_\xi^{\rm scr}$ as a pole of $\chi_{\xi\xi}(0,\tilde{q}^2)$:

$$\left[1-2G_\xi \Pi_\xi(0,\tilde{q}^2)\right]\big|_{\tilde{q}=iM_{\xi,\rm scr}}=0. \tag{3.27}$$

If the pole at $\tilde{q}=iM_\xi^{\rm scr}$ is well isolated from the cut, i.e., the condition $M_\xi^{\rm scr}<M_{\rm th}$ is well satisfied, one can determine the screening mass from the pole location without making the $\tilde{q}$ integral. In the high-T limit, the condition becomes $M_\xi^{\rm scr}<2\pi T$.

3.2.5 Meson susceptibility

Here, the meson susceptibility $\chi_\xi^{\rm sus}$ is considered for $\xi=\pi, a_0, \eta$ and σ. In LQCD simulations of Refs. [60, 61], the $\chi_\xi^{\rm sus}$ are defined in Euclidean space-time $x_{\rm E}=(\tau,\boldsymbol{x})$ as

$$\chi_\xi^{\rm sus}=\frac{1}{2}\int d^4x_{\rm E}\ \langle J_\xi(\tau,\boldsymbol{x})J_\xi^\dagger(0,\boldsymbol{0})\rangle. \tag{3.28}$$

In the LQCD simulations, it is assumed that J_σ and J_η have no s-quark component for simplicity: namely, $J_\sigma=\sum_{f=u,d}\bar{\psi}_f\psi_f-\langle\sum_{f=u,d}\bar{\psi}_f\psi_f\rangle$ and $J_\eta=\sum_{f=u,d}\bar{\psi}_f i\gamma_5\psi_f-\langle\sum_{f=u,d}\bar{\psi}_f i\gamma_5\psi_f\rangle$. For consistency, we take the same assumption also in the model analysis, and denote "the mesons with no s-quark (ns) component" by $\sigma_{\rm ns}$ and $\eta_{\rm ns}$. The factor $1/2$ is introduced to define the $\chi_\xi^{\rm sus}$ as single-flavor quantities.

The $\chi_\xi^{\rm sus}$ is related to the Matsubara Green's function $\chi_{\xi\xi}^{\rm E}(q_4^2,\boldsymbol{q}^2)$ in the momentum representation as

$$\chi_\xi^{\rm sus}=\frac{1}{2}\chi_{\xi\xi}^{\rm E}(q_4^2,\boldsymbol{q}^2)\big|_{q_4=0,\boldsymbol{q}=\boldsymbol{0}}, \tag{3.29}$$

and $\chi_{\xi\xi}^{\rm E}$ is obtainable from Eq. (3.14) for π and a_0 mesons. For $\eta_{\rm ns}$ meson, we have to consider a mixing between $\eta_{\rm ns}$ and $\eta_{\rm s}=\bar{\psi}_s i\gamma_5\psi_s$. As a result of this mixing, one can obtain $\chi_{\eta_{\rm ns}\eta_{\rm ns}}$ as [8]

$$\chi_{\eta_{\rm ns}\eta_{\rm ns}}=\frac{(1-2G_{\eta_{\rm s}\eta_{\rm s}}\Pi_{\eta_{\rm s}\eta_{\rm s}})\Pi_{\eta_{\rm ns}\eta_{\rm ns}}}{\det\left[\boldsymbol{I}-2\boldsymbol{G}\boldsymbol{\Pi}\right]}, \tag{3.30}$$

where $\mathbf{I}$ is the unit matrix and

$$\boldsymbol{G}=\begin{pmatrix} G_{\eta_{\rm s}\eta_{\rm s}} & G_{\eta_{\rm s}\eta_{\rm ns}} \\ G_{\eta_{\rm ns}\eta_{\rm s}} & G_{\eta_{\rm ns}\eta_{\rm ns}}\end{pmatrix},\quad \boldsymbol{\Pi}=\begin{pmatrix} \Pi_{\eta_{\rm s}\eta_{\rm s}} & 0 \\ 0 & \Pi_{\eta_{\rm ns}\eta_{\rm ns}}\end{pmatrix} \tag{3.31}$$

for the elements

$$G_{\eta_{\rm s}\eta_{\rm s}} = G_{\rm S}(\Phi), \tag{3.32}$$

$$G_{\eta_{\rm ns}\eta_{\rm ns}} = G_{\rm S}(\Phi)+\frac{1}{2}K(T)\sigma_s, \tag{3.33}$$

$$G_{\eta_{\rm s}\eta_{\rm ns}} = G_{\eta_{\rm ns}\eta_{\rm s}}=\frac{\sqrt{2}}{2}K(T)\sigma_l. \tag{3.34}$$

In the isospin-symmetric case we consider, the polarization functions $\Pi_{\eta_s\eta_s}$ and $\Pi_{\eta_{ns}\eta_{ns}}$ have the same form as Π_π:

$$\Pi_{\eta_s\eta_s} = \Pi_\pi(M_s), \tag{3.35}$$

$$\Pi_{\eta_{ns}\eta_{ns}} = \Pi_\pi(M_l), \tag{3.36}$$

where note that $\Pi_\pi(M_s)$ is a function of not M_l but M_s. Similarly, $\chi_{\sigma_{ns}\sigma_{ns}}$ is obtainable from Eq. (3.30) with $K(T)$ replaced by $-K(T)$ and Π_π by Π_{a_0}.

3.3 Numerical Results

3.3.1 Meson screening masses

The EPNJL model has three adjustable parameters, α_1 in the entanglement coupling $G_S(\Phi)$ and b and T_1 in the KMT interaction $K(T)$. These parameters can be clearly determined from LQCD data [30] for pion and a_0-meson screening masses, $M_\pi^{\rm scr}$ and $M_{a_0}^{\rm scr}$, as shown below.

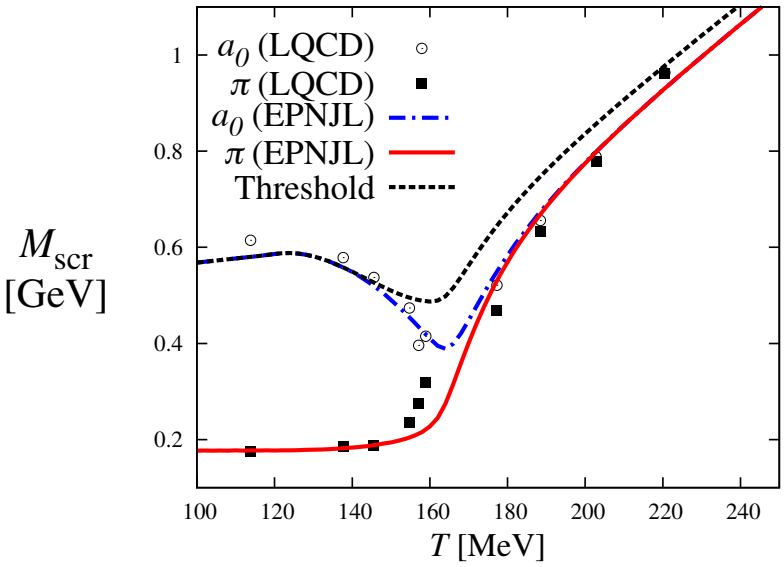

Fig. 3.2: T dependence of pion and a_0-meson screening masses, $M_\pi^{\rm scr}$ and $M_{a_0}^{\rm scr}$. The solid (dot-dash) line denotes $M_\pi^{\rm scr}$ ($M_{a_0}^{\rm scr}$) calculated by the EPNJL model, whereas the dotted line corresponds to the threshold mass. LQCD data are taken from Ref. [30]; closed squares (open circles) correspond to the 2+1-flavor data for $M_\pi^{\rm scr}$ ($M_{a_0}^{\rm scr}$). In Ref. [30], T_c^χ was considered 196 MeV, but it was refined to 154 ± 9 MeV [40, 41]. The latest value is taken in this figure.

Figure 3.2 shows T dependence of $M_\pi^{\rm scr}$ and $M_{a_0}^{\rm scr}$. Best fitting is obtained, when $\alpha_1 = 1.0$, $T_1 = 0.79T_c^\chi = 121$ MeV and $b = 0.23T_c^\chi = 36$ MeV. In fact, the EPNJL results (solid and dot-dash lines) with this parameter set well

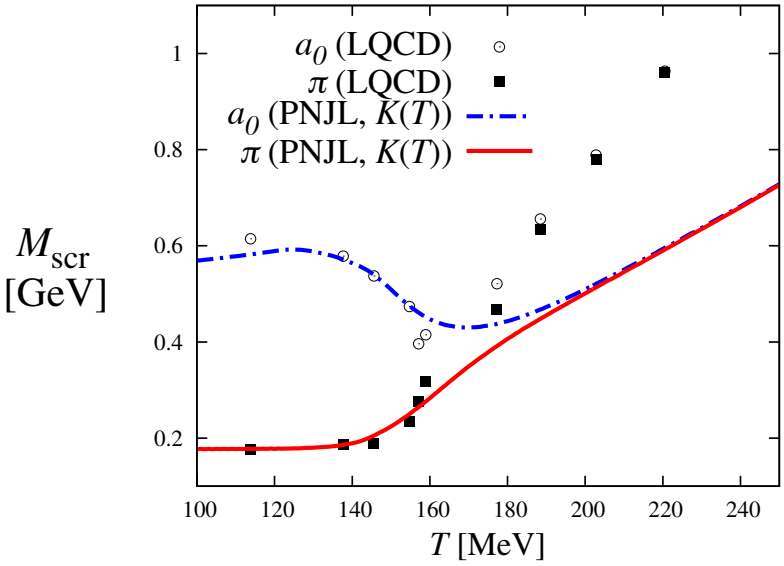

Fig. 3.3: Effects of T-dependent KMT interaction on pion and a_0-meson screening masses. The solid (dot-dash) line denotes $M_\pi^{\rm scr}$ ($M_{a_0}^{\rm scr}$) calculated by the PNJL model with T-dependent coupling $K(T)$. See Fig. 3.2 for LQCD data.

account for LQCD data [30] for both $M_\pi^{\rm scr}$ and $M_{a_0}^{\rm scr}$. The parameters thus obtained indicate the strong suppression of $K(T)$ in the vicinity of T_c^χ. The mass difference $\Delta M_{\rm scr}(T) = M_{a_0}^{\rm scr}(T) - M_\pi^{\rm scr}(T)$ is sensitive to $K(T)$ because of Eqs. (3.15) and (3.16), and hence the values of b and T_1 are well determined from $\Delta M_{\rm scr}(T)$.

When $\alpha_1 = 0$, the EPNJL model is reduced to the PNJL model. The results of the PNJL model are shown in Fig. 3.3 for comparison. The PNJL results cannot reproduce LQCD data particularly in the region $T \gtrsim 180$ MeV. The slope of the solid and dot-dash lines in the region is thus sensitive to the value of α_1. Namely, the value of α_1 is well determined from the slope.

In Fig. 3.2, the solid and dot-dash lines are lower than the threshold mass $2M_{j=1,n=0,\alpha=0}$ (dotted line). This guarantees that the $M_\pi^{\rm scr}$ and $M_{a_0}^{\rm scr}$ determined from the pole location in the complex-$\tilde{q}$ plane agree with those from the exponential decay of $\zeta_{\xi\xi}(0,\boldsymbol{x})$ at large $r = |\boldsymbol{x}|$.

In the EPNJL model with the present parameter, the chiral susceptibility χ_{ll} for light quarks has a peak at $T = 163$ MeV, as shown later in Fig. 3.11(a). This indicates $T_c^\chi = 163$ MeV. The model result is consistent with LQCD data $T_c^\chi = 154 \pm 9$ MeV of Refs. [40, 41] close to the continuum limit. For the deconfinement transition, meanwhile, the parameter T_0 is adjusted to reproduce LQCD data on $T_c^{\rm deconf}$, as already mentioned in Sec. 3.2. In fact, the Polyakov-loop susceptibility $\bar{\chi}_{\Phi\bar{\Phi}}$ has a peak at $T = 165$ MeV in the EPNJL model, as shown in Fig. 3.11(b). The model result $T_c^{\rm deconf} = 165$ MeV is consistent with LQCD data $T_c^{\rm deconf} = 170 \pm 7$ MeV of Ref. [63] close

to the continuum limit.

Figure 3.4 shows T dependence of the renormalized chiral condensate $\Delta_{l,s}$ defined by

$$\Delta_{l,s} \equiv \frac{\sigma_l(T) - \frac{m_l}{m_s}\sigma_s(T)}{\sigma_l(0) - \frac{m_l}{m_s}\sigma_s(0)}, \tag{3.37}$$

and the Polyakov loop Φ. The present EPNJL model well reproduces LQCD data [40] for the magnitude of $\Delta_{l,s}$ in addition to the value of T_c^{χ}. The present model overestimates LQCD data for the magnitude of Φ, although it yields a result consistent with LQCD for $T_c^{\rm deconf}$. The overestimation in the magnitude of Φ is a famous problem in the PNJL model. Actually, many PNJL calculations have this overestimation. This is considered to come from the fact that the definition of the Polyakov loop is different between LQCD and the PNJL model [65, 66]. In LQCD the definition is $\Phi_{\rm LQCD} = \langle {\rm tr}_c\, \mathcal{T} \exp[i\int_0^{1/T} d\tau A_4(\tau, \boldsymbol{x})]\rangle/3$, while in the PNJL model based on the Polyakov gauge and the mean-field approximation the definition is $\Phi_{\rm PNJL} = {\rm tr}_c \exp[i\langle A_4\rangle/T]/3$, although both are order parameters of Z_3 symmetry [65, 66]; see for example Ref. [14, 67] as a trial to solve this problem.

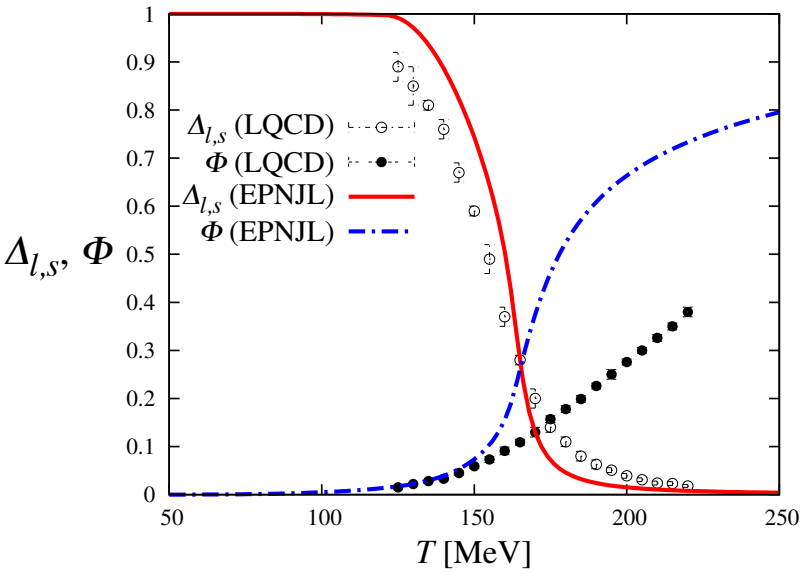

Fig. 3.4: T dependence of $\Delta_{l,s}$ and Φ. The solid (dot-dash) line corresponds to results of the EPNJL model for $\Delta_{l,s}$ (Φ). LQCD data for 2+1 flavors are taken from Ref. [40].

Now we investigate effects of T-dependent KMT interaction $K(T)$ on $M_\pi^{\rm scr}$ and $M_{a_0}^{\rm scr}$. In Fig. 3.5, T-dependence of $K(T)$ is switched off; namely, the results of the EPNJL model with $K(T) = K(0)$ are shown. One can see that T-dependence of $K(T)$ reduces the mass difference $\Delta M^{\rm scr} = M_{a_0}^{\rm scr} - M_\pi^{\rm scr}$ significantly in a range $150 \lesssim T \lesssim 180$ MeV, comparing Fig. 3.5 with Fig. 3.2. At $T = 176$ MeV where the first-order chiral and deconfinement transitions

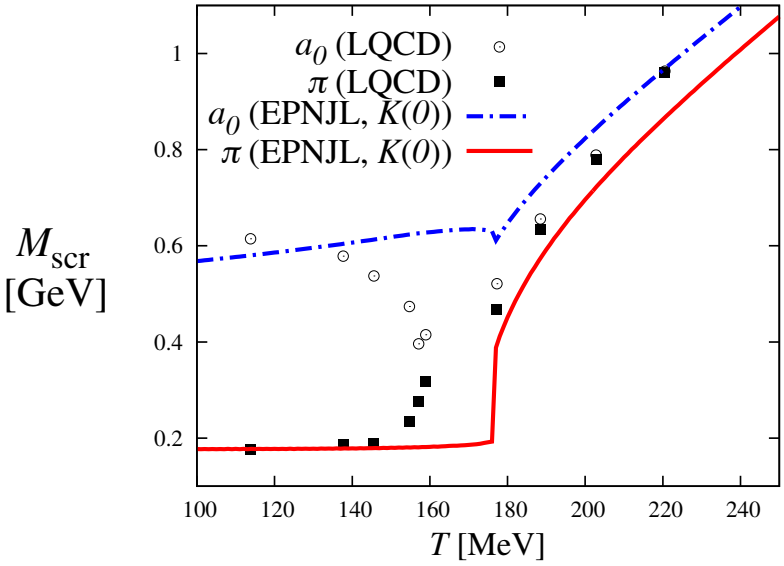

Fig. 3.5: Effects of T-dependent KMT interaction on pion and a_0-meson screening masses. The solid (dot-dash) line denotes $M_\pi^{\rm scr}$ ($M_{a_0}^{\rm scr}$) calculated by the EPNJL model with $K(T) = K(0)$. See Fig. 3.2 for LQCD data.

take place, $M_\pi^{\rm scr}$ has a jump while $M_{a_0}^{\rm scr}$ has a cusp. Meson screening mass is thus a good indicator for the first-order transitions.

In Fig. 3.6, both T dependence of $K(T)$ and the entanglement of $G_{\rm S}(\Phi)$ are switched off. Namely, the results of the standard PNJL model with a constant K are shown. The model cannot reproduce LQCD data, as expected.

Figure 3.7 shows three types of EPNJL calculations for the mass difference $\Delta M_{\rm scr}(T)$. The mass difference plays a role of the order parameter of the effective restoration of $U(1)_A$ symmetry. The full-fledged EPNJL calculations (solid line) with both T-dependent K and the entanglement coupling $G_{\rm S}(\Phi)$ well reproduce LQCD data, while the standard PNJL model (dotted line) with constant K largely overestimates the data.

The present model has T dependence implicitly in $G_{\rm S}(\Phi)$ through Φ and explicitly in $K(T)$. As a model opposite to the present one, one may consider the case that $K(T) = K(0)$ and $G_{\rm S}$ has T dependence explicitly, i. e., $G_{\rm S} = G_{\rm S}(T)$. We can determine $G_{\rm S}(T)$ so as to reproduce LQCD data for $\Delta_{l,s}$; however, this model overestimates LQCD data for $\Delta M_{\rm scr}$. Thus the present model is well designed.

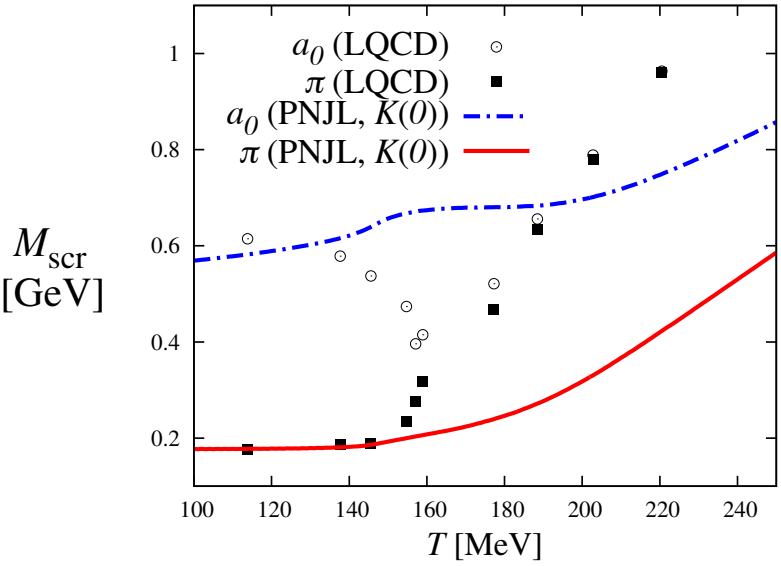

Fig. 3.6: Effects of the entanglement coupling $G_{\rm S}(\Phi)$ on pion and a_0-meson screening masses. The solid (dot-dash) line denotes $M_\pi^{\rm scr}$ ($M_{a_0}^{\rm scr}$) calculated by the standard PNJL model with constant K, i.e., the EPNJL model with $K(T) = K(0)$ and $\alpha_1 = 0$. See Fig. 3.2 for LQCD data.

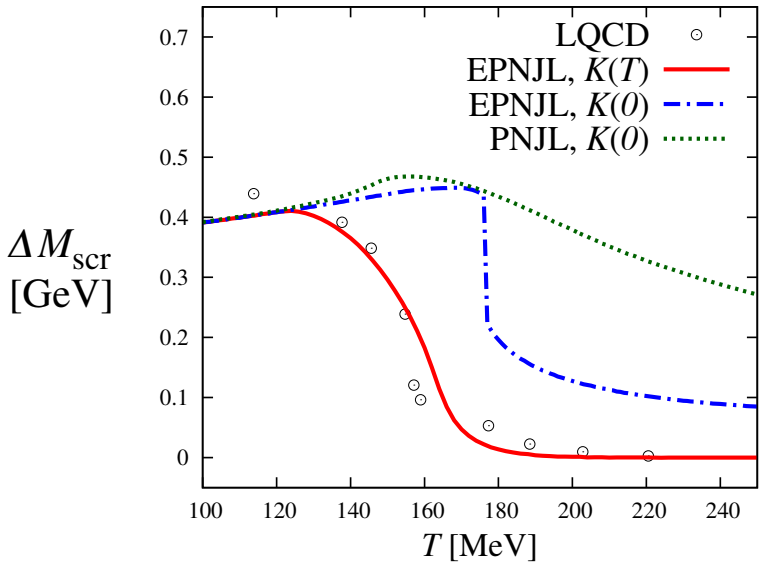

Fig. 3.7: Mass difference $\Delta M_{\rm scr}(T)$ between pion and a_0-meson screening masses. The solid, dot-dash and dotted lines denote results of the EPNJL model, the EPNJL model with $K(T) = K(0)$ and the standard PNJL model with $K(T) = K(0)$, respectively. See Fig. 3.2 for LQCD data.

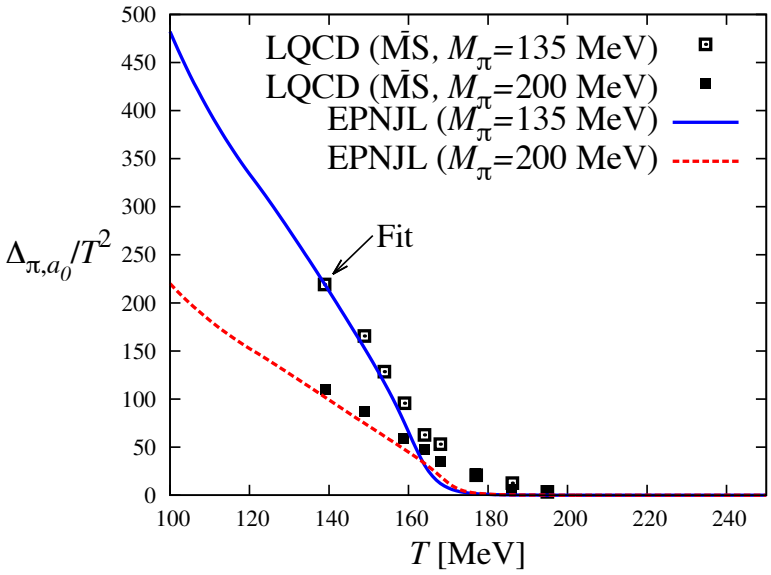

Fig. 3.8: T dependence of the difference Δ_{π,a_0} between π and a_0 meson susceptibilities for two cases of $M_\pi(0) = 135$ and 200 MeV.

3.3.2 Meson susceptibilities

The validity of $K(T)$ is investigated by comparing LQCD data with the model results for meson susceptibilities $\chi_\xi^{\rm sus}$ ($\xi = \pi, a_0, \eta_{\rm ns}, \sigma_{\rm ns}$). LQCD data based on domain-wall fermions [61] are available for two cases of pion mass $M_\pi(0)$ at vacuum being the physical value 135 MeV and a slightly heavier value 200 MeV. In order to reproduce these values with the EPNJL model, we take $m_l = 5.68$ MeV for the first case and 12.8 MeV for the second one.

We consider the difference $\Delta_{\pi,a_0} = \chi_\pi^{\rm sus} - \chi_{a_0}^{\rm sus}$ as an order parameter of the effective $U(1)_A$-symmetry restoration. Figure 3.8 shows T dependence of $\Delta_{\pi,a_0}/T^2$ for two cases of $M_\pi(0) = 135$ and 200 MeV. Since the $\chi_\xi^{\rm sus}$ have ultraviolet divergence, they are renormalized with the $\overline{\rm MS}$ scheme in LQCD. For this reason, one cannot compare the LQCD data with the results of the EPNJL model directly. We then multiply the model results by a constant so as to reproduce LQCD data at $T = 139$ MeV for the case of $M_\pi(0) = 135$ MeV. The model results thus renormalized well reproduce LQCD data for any T in both cases of $M_\pi(0) = 135$ and 200 MeV, as shown in Fig. 3.8.

Similar analyses are made for T dependence of $\Delta_{\pi,\sigma} = \chi_\pi^{\rm sus} - \chi_{\sigma_{\rm ns}}^{\rm sus}$ and $\Delta_{\eta,a_0} = \chi_{\eta_{\rm ns}}^{\rm sus} - \chi_{a_0}^{\rm sus}$ that are related to $SU(2)_L \times SU(2)_R$ symmetry. Figures 3.9 and 3.10 show T dependence of $\Delta_{\pi,\sigma}/T^2$ and $\Delta_{\eta,a_0}/T^2$ for $M_\pi(T) = 135$ MeV and 200 MeV, respectively. In both the figures, the EPNJL model well reproduces T dependence of LQCD results. The present model with the $K(T)$ of Eq. (3.4) is thus reasonable.

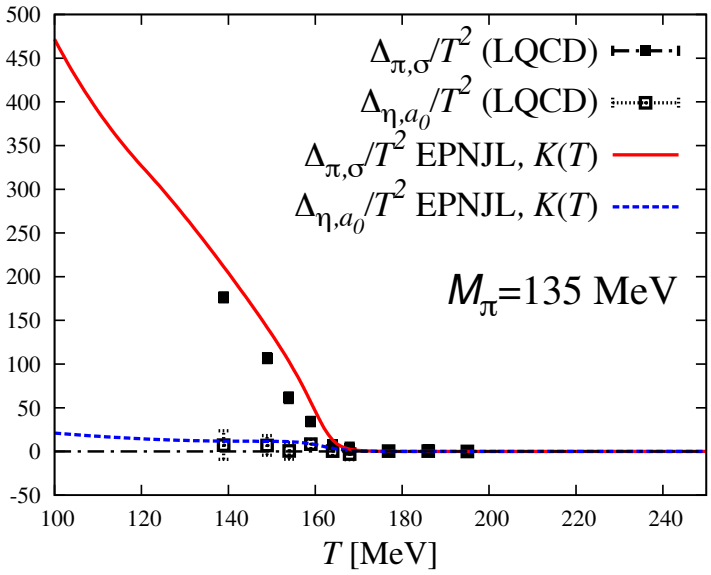

Fig. 3.9: T dependence of $\Delta_{\pi,\sigma}$ and Δ_{η,a_0} for $M_\pi(0) = 135$ MeV.

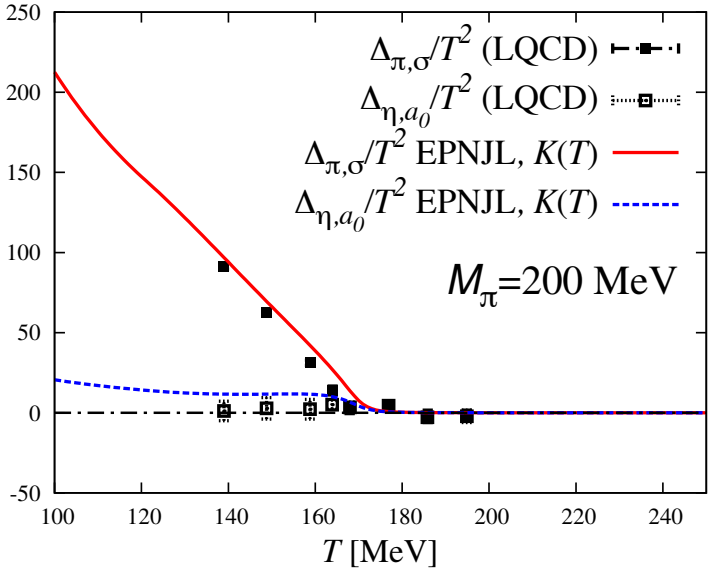

Fig. 3.10: T dependence of $\Delta_{\pi,\sigma}$ and Δ_{η,a_0} for $M_\pi(0) = 200$ MeV.

3.3.3 The order of chiral transition near the physical point

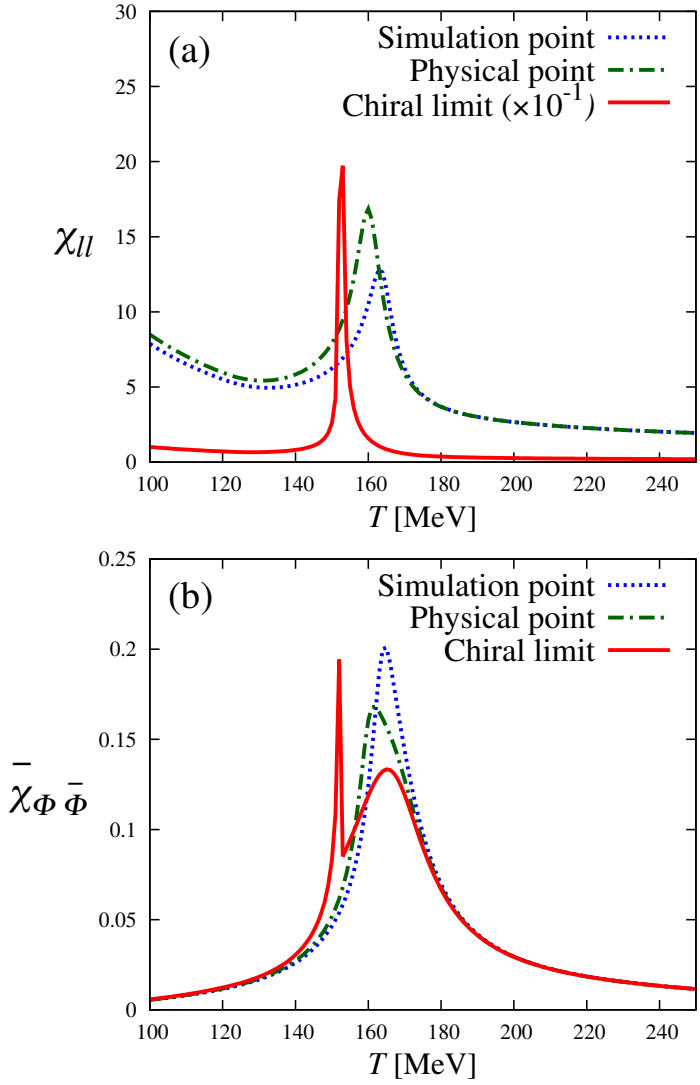

Fig. 3.11: T dependence of (a) chiral susceptibility χ_{ll} and (b) Polyakov-loop susceptibility $\bar{\chi}_{\Phi\bar{\Phi}}$ at S-point, P-point and C_l-point. Here χ_{ll} and $\bar{\chi}_{\Phi\bar{\Phi}}$ are dimensionless and their definition is the same as in the LQCD formulation. Calculations are done by the EPNJL model with the present parameter set. The dotted, dot-dash and solid lines stand for the results at S-point, P-point and C_l-point, respectively. At C_l-point, χ_{ll} is divided by 10 and diverges at $T = T_c^{\chi} = 153$ MeV

Finally we consider the order of chiral transition near the physical point $(m_l^{\rm phys}, m_s^{\rm phys}) = (6.2\ {\rm MeV}, 175\ {\rm MeV})$ in the m_l–m_s plane, First we vary m_l from 9.9 to 0 MeV with m_s fixed at 175 MeV.

Following the Ref. [68], we calculate the chiral susceptibility χ_{ll} for light quarks and the Polyakov-loop susceptibility $\bar{\chi}_{\Phi\bar{\Phi}}$ defined by $\bar{\chi}_{\Phi\bar{\Phi}} \equiv (\chi_{\Phi\Phi} +$

$2\chi_{\Phi\bar{\Phi}} + \chi_{\bar{\Phi}\bar{\Phi}})/4$. Figure 3.11 presents T dependence of χ_{ll} and $\bar{\chi}_{\Phi\bar{\Phi}}$ in three points, "simulation point (S-point)" of $(m_l, m_s) = (9.9\ \text{MeV}, 175\ \text{MeV})$, "physical point (P-point)" of $(m_l, m_s) = (6.2\ \text{MeV}, 175\ \text{MeV})$ and "light-quark chiral-limit point (C_l point)" of $(m_l, m_s) = (0\ \text{MeV}, 175\ \text{MeV})$. The transition temperatures, T_c^{χ} and T_c^{deconf}, are determined from the peak positions of χ_{ll} and $\bar{\chi}_{\Phi\bar{\Phi}}$, and depend on m_l and m_s. However, as shown in Fig. 3.11 (a), the T_c^{χ} thus determined is 163 MeV for S-point and 160 MeV for P-point, and hence the value little varies between the two points. For C_l-point, χ_{ll} diverges at $T = T_c^{\chi} = 153$ MeV. The chiral transition is thus second order at C_l-point at least in the mean-field level. This result suggests that the effective $U(1)_{\text{A}}$ restoration is not completed at $T = T_c^{\chi}$. This suggestion is supported by LQCD data at S-point in Fig. 3.7 where $\Delta M_{\text{scr}}(T_c^{\chi})$ is about a half of $\Delta M_{\text{scr}}(0)$.

As shown in Fig. 3.11 (b), m_l dependence of T_c^{deconf} is even smaller; namely, $T_c^{\text{deconf}} = 165$ MeV for S-point and C_l-point and 163 MeV for P-point. For C_l-point, $\bar{\chi}_{\Phi\bar{\Phi}}$ has a sharp peak at $T = 153$ MeV. It is just a result of the propagation of divergence from χ_{ll} to $\bar{\chi}_{\Phi\bar{\Phi}}$ [69], and never means that a second-order deconfinement takes place there.

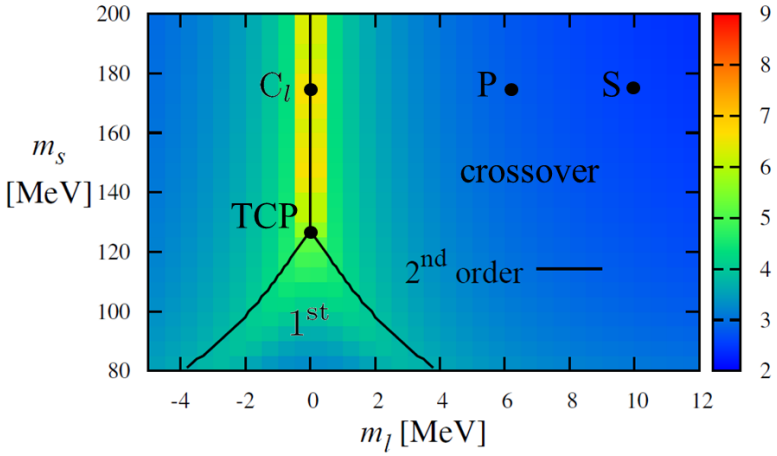

Fig. 3.12: Order of chiral transition near physical point in the m_l–m_s plane. The value of $\log[\chi_{ll}(T_c^{\chi})]$ is shown by a change in hue. Simulation point, physical point, light-quark chiral-limit point and tricritical point are denoted by S, P, C_l and TCP. The solid lines stand for second-order chiral transitions.

Next, both m_l and m_s are varied near P-point. Figure 3.12 shows the values of $\log[\chi_{ll}(T_c^{\chi})]$ near P-point in the m_l–m_s plane. The values are denoted by a change in hue. Three second-order chiral transitions (solid lines) meet

at $(m_l^{\rm tric}, m_s^{\rm tric}) \approx (0, 0.726 m_s^{\rm phys}) = (0\ {\rm MeV}, 127\ {\rm MeV})$. This is nothing but the tricritical point (TCP) of chiral phase transition.

3.4 Short Summary

In this chapter, we have investigated chiral dynamics in the m_l-m_s plane (Columbia plot). For this purpose, we have introduced the effective $U(1)_{\rm A}$-symmetry restoration to the 2+1-flavor EPNJL model by considering the T-dependent coupling strength $K(T)$ of the KMT interaction. The $K(T)$ was well determined from state-of-the-art LQCD data on T dependence of the difference between pion and a_0-meson screening masses. The $K(T)$ thus obtained is strongly suppressed around the pseudocritical temperature of chiral transition.

In order to check the validity of the $K(T)$, we have analyzed LQCD data on T dependence of meson susceptibilities of $U(1)_{\rm A}$ partner (π and a_0 mesons) and chiral partner (π and $\sigma_{\rm ns}$ mesons). We have found good agreement between LQCD results and the EPNJL model ones.

By using this reliable model, we have investigated the Columbia plot near the physical point $(m_l, m_s) = (m_l^{\rm phys}, m_s^{\rm phys}) = (6.2\ {\rm MeV}, 175\ {\rm MeV})$. We have showed that chiral transition is the second order at the light-quark chiral limit point $(m_l, m_s) = (0, m_s^{\rm phys}) = (0, 175\ {\rm MeV})$. We have also found that a tricritical point (TCP) exists on the line of $m_l = 0$ in the m_l-m_s plane. The TCP is located in the southwest direction from physical point. The location we predicted is $(m_l, m_s) \approx (0, 0.726 m_s^{\rm phys}) = (0\ {\rm MeV}, 127\ {\rm MeV})$.

Chapter 4

Model prediction for meson pole masses

In this chapter, we predict ξ-meson pole masses $M_\xi^{\rm pole}(T)$ from ξ-meson screening masses $M_\xi^{\rm scr}(T)$ calculated with LQCD simulations by proposing a practical effective model. First, we construct the effective model that reproduces LQCD data on T dependence of scalar and pseudoscalar meson screening masses. We consider a new version of PNJL model with T-dependent coupling strengths of four-quark and six-quark Kobayashi-Maskawa-'t Hooft interactions. The T-dependent coupling strengths are well determined from LQCD data on the chiral-symmetry restoration and the effective $U(1)_{\rm A}$-symmetry restoration. We show that our model well reproduces LQCD data on $M_\xi^{\rm scr}(T)$ for both scalar and pseudoscalar mesons, particularly in $T \gtrsim T_c^\chi$, without introducing new adjustable parameters. Using the effective model, we predict T dependence of $M_\xi^{\rm pole}(T)$ for scalar and pseudoscalar mesons. For η' meson, we find that the model prediction is consistent with the experimental value at finite T extracted from indirect measurements in heavy-ion collisions. Finally, we show that the relation $M_\xi^{\rm scr}(T) - M_\xi^{\rm pole}(T) \approx M_{\xi'}^{\rm scr}(T) - M_{\xi'}^{\rm pole}(T)$ is considerably good when ξ and ξ' belong to scalar mesons, and suggest that the relation $M_\xi^{\rm scr}(T)/M_{\xi'}^{\rm scr}(T) \approx M_\xi^{\rm pole}(T)/M_{\xi'}^{\rm pole}(T)$ is satisfied within 20% error when ξ and ξ' belong to pseudoscalar mesons and also when ξ and ξ' belong to scalar mesons.

4.1 Formalism

4.1.1 Model setting

We extend the 2+1-flavor PNJL model [9–24] by introducing T dependence to the coupling strengths for four- and six-quark interactions: Namely, $G_{\rm S} = G_{\rm S}(T)$ and $G_{\rm D} = G_{\rm D}(T)$. The Lagrangian density in Minkowski space is

defined as

$$\begin{aligned}\mathcal{L} =&\bar{\psi}(i\gamma_\nu D^\nu - \hat{m}_0)\psi + G_{\rm S}(T)\sum_{a=0}^{8}[(\bar{\psi}\lambda_a\psi)^2 + (\bar{\psi}i\gamma_5\lambda_a\psi)^2] \\ &- G_{\rm D}(T)\Big[\det_{f,f'}\bar{\psi}_f(1+\gamma_5)\psi_{f'} + \det_{f,f'}\bar{\psi}_f(1-\gamma_5)\psi_{f'}\Big] \\ &- \mathcal{U}(\Phi[A],\bar{\Phi}[A],T),\end{aligned} \tag{4.1}$$

where the gauge fields A^ν are introduced through the covariant derivative $D^\nu = \partial^\nu + iA^\nu$ and are assumed to be $A^\nu = g\delta^\nu_0(A^0)_a t_a/2 = -ig\delta^\nu_0(A_4)_a t_a/2$ for the gauge coupling g. The quark fields $\psi = (\psi_u, \psi_d, \psi_s)^{\rm T}$ have current quark masses $\hat{m}_0 = {\rm diag}(m_u, m_d, m_s)$ satisfying $m_s > m_l \equiv m_u = m_d$ in the 2+1-flavor system. The matrices λ_a (t_a) for $a = 1, ..., 8$ are the Gell-Mann matrices in flavor (color) space. Furthermore, λ_0 is related to the unit matrix $\boldsymbol{I}_{\rm F}$ in flavor space as $\lambda_0 = \sqrt{2/3}\,\boldsymbol{I}_{\rm F}$, and $\det_{f,f'}$ stands for the determinant in flavor space.

Following our discussion in Chapter 3, we determine T dependence of $G_{\rm D}(T)$ in order to reproduce LQCD data on the $U(1)_{\rm A}$-symmetry restoration. The T-dependent strength $G_{\rm D}(T)$ thus determined is defined by

$$G_{\rm D}(T) = \begin{cases} G_{\rm D}(0) & (T < T_1) \\ G_{\rm D}(0)e^{-(T-T_1)^2/b_1^2} & (T \geq T_1) \end{cases} . \tag{4.2}$$

As mentioned above, we also introduce T dependence to the coupling strength $G_{\rm S}$ of four-quark interaction. We assume that $G_{\rm S}(T)$ has the same function form as $G_{\rm D}(T)$:

$$G_{\rm S}(T) = \begin{cases} G_{\rm S}(0) & (T < T_2) \\ G_{\rm S}(0)e^{-(T-T_2)^2/b_2^2} & (T \geq T_2) \end{cases} . \tag{4.3}$$

One can determine the parameter set (T_1, b_1) from LQCD data on $\Delta M^{\rm scr}_{a_0,\pi}(T)$ and the set (T_2, b_2) from LQCD data on $\Delta_{l,s}(T)$. We tabulate the resultant values in Table 4.1. We will show the detail of the parameter fitting in Sec. 4.2.1. In Chapter 3, we used the EPNJL model with a T-dependent KMT interaction of form (4.2). The present values of T_1 and b_1, shown in Table 4.1, are close to the ones in the EPNJL model.

Table 4.1: Model parameters in coupling strengths $G_{\rm S}(T)$ and $G_{\rm D}(T)$.

T_1 [MeV]	b_1 [MeV]	T_2 [MeV]	b_2 [MeV]
121	43.5	131	83.3

As shown in Chapter 2, the Polyakov loop Φ and its Hermitian conjugate $\bar{\Phi}$ are obtained by

$$\Phi = \frac{1}{3}{\rm tr}_{\rm c}(L), \qquad \bar{\Phi} = \frac{1}{3}{\rm tr}_{\rm c}(L^*) \tag{4.4}$$

with the Polyakov-loop operator

$$L = \exp[iA_4/T] = \exp[i \times \mathrm{diag}(A_4^{11}, A_4^{22}, A_4^{33})/T] \tag{4.5}$$

for real variables A_4^{jj} satisfying $A_4^{11} + A_4^{22} + A_4^{33} = 0$. For the case of $\mu = 0$ where $\Phi = \bar{\Phi}$, note that we can set $A_4^{33} = 0$ and determine the others as $A_4^{22} = -A_4^{11} = \cos^{-1}[(3\Phi - 1)/2]$.

Again, we take the logarithm-type Polyakov-loop potential of Ref. [18] as $\mathcal{U}$. The parameter T_0 included in $\mathcal{U}$ is used as an adjustable parameter. In the present case, we take $T_0 = 180$ MeV so that the PNJL model can reproduce 2+1-flavor LQCD data on T dependence of pion screening mass at $T \gtrsim T_c^\chi = 154 \pm 9$ MeV, where the value of T_c^χ is determined from LQCD simulations [40, 41].

Making the mean-field approximation (MFA) to Eq. (4.1), one can obtain the linearized Lagrangian density

$$\mathcal{L}^{\mathrm{MFA}} = \bar{\psi} S^{-1} \psi - U_{\mathrm{M}} - \mathcal{U}(\Phi[A], \bar{\Phi}[A], T), \tag{4.6}$$

where the quark propagator

$$S = (i\gamma_\nu \partial^\nu - \gamma_0 A^0 - \hat{M})^{-1} \tag{4.7}$$

depends on the chiral condensates $\sigma_f = \langle \bar{\psi}_f \psi_f \rangle$ $(f = u, d, s)$ through the effective-mass matrix $\hat{M} = \mathrm{diag}(M_u, M_d, M_s)$ with

$$\begin{aligned} M_u &= m_u - 4G_{\mathrm{S}}(T)\sigma_u + 2G_{\mathrm{D}}(T)\sigma_d\sigma_s, \\ M_d &= m_d - 4G_{\mathrm{S}}(T)\sigma_d + 2G_{\mathrm{D}}(T)\sigma_s\sigma_u, \\ M_s &= m_s - 4G_{\mathrm{S}}(T)\sigma_s + 2G_{\mathrm{D}}(T)\sigma_u\sigma_d. \end{aligned}$$

The mesonic potential U_{M} is defined by

$$U_{\mathrm{M}} = 2G_{\mathrm{S}}(T)(\sigma_u^2 + \sigma_d^2 + \sigma_s^2) - 4G_{\mathrm{D}}(T)\sigma_u\sigma_d\sigma_s.$$

Making the path integral over quark fields in the mean-field action, one can get the thermodynamic potential (per unit volume)

$$\begin{aligned} \Omega_{\mathrm{PNJL}} = U_{\mathrm{M}} + \mathcal{U} - 2 \sum_{f=u,d,s} \int \frac{d^3\boldsymbol{p}}{(2\pi)^3} \Big[& 3E_{\boldsymbol{p},f} \\ & + \frac{1}{\beta} \ln \left[1 + 3(\Phi + \bar{\Phi} e^{-\beta E_{\boldsymbol{p},f}}) e^{-\beta E_{\boldsymbol{p},f}} + e^{-3\beta E_{\boldsymbol{p},f}}\right] \\ & + \frac{1}{\beta} \ln \left[1 + 3(\bar{\Phi} + \Phi e^{-\beta E_{\boldsymbol{p},f}}) e^{-\beta E_{\boldsymbol{p},f}} + e^{-3\beta E_{\boldsymbol{p},f}}\right] \Big] \end{aligned} \tag{4.8}$$

with $E_{\boldsymbol{p},f} = \sqrt{\boldsymbol{p}^2 + M_f^2}$ and $\beta = 1/T$. Mean-field variables (σ_l, σ_s, Φ and $\bar{\Phi}$) are determined to minimize Ω_{PNJL}, where isospin symmetry is assumed for the light-quark sector, i.e., $\sigma_l \equiv \sigma_u = \sigma_d$ and $M_l = M_u = M_d$.

On the right-hand side of Eq. (4.8), the first term (vacuum term) diverges. The three-dimensional momentum-cutoff regularization is often used to avoid the divergence. However, the regularization breaks Lorentz invariance. This breaking induces an unphysical oscillation in the spatial correlation function $\zeta_{\xi\xi}(0, \boldsymbol{x})$ [35]. Furthermore, the basic relation $M_\xi^{\rm pole}(0) = M_\xi^{\rm scr}(0)$ is not satisfied as a result of the Lorentz-symmetry breaking. We then use the Pauli-Villars (PV) regularization [32,35] since it preserves Lorentz invariance. This PV regularization has a parameter Λ with mass dimension; see Sec. 4.1.3 for further explanation.

Table 4.2: Model parameters determined from physical quantities at vacuum. Set (A) is the realistic parameter set that is determined from experimental or empirical values at vacuum. In set (B), m_l and m_s are slightly changed from set (A) so as to become consistent with the lattice setting ($m_l/m_s = 1/10$ and $M_\pi^{\rm pole}(0) = 176$ MeV) of LQCD simulations of Ref. [30, 70].

	m_l [MeV]	m_s [MeV]	$G_{\rm S}(0)\Lambda^2$	$G_{\rm D}(0)\Lambda^5$	Λ [MeV]
set (A) :	8	191	2.72	40.4	660
set (B) :	13	130	2.72	40.4	660

The present model has five parameters $(m_l, m_s, G_{\rm S}(0), G_{\rm D}(0), \Lambda)$ in addition to T_0, (T_1, b_1) and (T_2, b_2). The five parameters can be determined from experimental data or empirical values at vacuum. The determination of the five parameters should be made before the determination of T_0, (T_1, b_1) and (T_2, b_2). We first assume $m_l = 8$ MeV and then determine the values of $(m_s, G_{\rm S}(0), G_{\rm D}(0), \Lambda)$ so as to reproduce experimental data on $f_\pi = 92.4$ MeV, $M_\pi^{\rm pole} = 138$ MeV, $M_K^{\rm pole} = 495$ MeV and $M_{\eta'}^{\rm pole} = 958$ MeV, where f_π is the pion decay constant. The resulting parameter values are shown as set (A) in Table 4.2. When we compare model results with LQCD data, we refit the values of m_l and m_s so as to become consistent with the lattice setting. The parameter set with such a parameter tuning is referred to as set (B) in this thesis; see Sec. 4.1.4 for the detail.

Table 4.3 shows physical quantities at vacuum calculated with the parameter set (A) of Table 4.2 and the corresponding experimental or empirical values. Numbers with asterisk are inputs of the present parameter fitting. The parameter set (A) reproduces available experimental data reasonably well. In addition, the results of set (A) are close to those of the parameter set in Ref. [8] for meson pole masses for $\eta, a_0, \kappa, \sigma, f_0$, the mixing angle θ_η between η_0 and η_8 states, the mixing angle θ_σ between σ_0 and σ_8 states, the effective s-quark mass M_s, and the kaon decay constant f_K.

Table 4.3: Physical quantities at vacuum calculated with the parameter set (A) of Table 4.2 and the corresponding experimental or empirical values. Numbers with asterisk are inputs of the present parameter fitting. Experimental data are taken from Refs. [1, 71]. The effective light-quark mass $M_l \approx 336$ MeV is estimated from experimental data on baryon magnetic moments [71]. Since we impose the isospin symmetry, we estimate experimental values of averaged pion and kaon masses as $M_\pi \equiv (M_{\pi^0}^{\rm exp} + M_{\pi^+}^{\rm exp} + M_{\pi^-}^{\rm exp})/3 = (134.97 + 2 \times 139.57)/3 = 138.0$ MeV and $M_K \equiv (M_{K^0}^{\rm exp} + M_{\bar{K}^0}^{\rm exp} + M_{K^+}^{\rm exp} + M_{K^-}^{\rm exp})/4 = (2 \times 497.61 + 2 \times 493.68)/4 = 495.6$ MeV. Experimental data on the decay constants f_π and f_K are taken for charged pion and kaon.

	M_π [MeV]	M_K [MeV]	$M_{\eta'}$ [MeV]	f_π [MeV]	f_K [MeV]
Cal.	138*	495*	958*	92.4*	96.2
Exp.	138.0	495.6	957.8	92.2	110.5
	M_η [MeV]	M_{a_0} [MeV]	M_κ [MeV]	M_σ [MeV]	M_{f_0} [MeV]
Cal.	487	813	1016	674	1185
Exp.	547.8	980±20	800	400∼550	980±20
	θ_η	θ_σ	M_l [MeV]	M_s [MeV]	
Cal.	$-7.40°$	$17.6°$	336	544	
Exp.	$-11.4°$	–	336	–	

4.1.2 Meson pole masses

We consider pseudoscalar mesons ($\xi = \pi, K, \eta, \eta'$) and scalar ones ($\xi = a_0, \kappa, \sigma, f_0$), and recapitulate the formalism of Ref. [8]. The current operator for ξ meson is expressed by

$$J_\xi(x) = \bar{\psi}(x) \Gamma_\xi \psi(x) - \langle \bar{\psi}(x) \Gamma_\xi \psi(x) \rangle \tag{4.9}$$

with $\Gamma_\xi = \boldsymbol{I}_{\rm C} \otimes \Gamma_{\rm D} \otimes \Gamma_{\rm F}$, where $\boldsymbol{I}_{\rm C}$ is the unit matrix in color space. The matrix $\Gamma_{\rm D}$ in Dirac space is $\Gamma_{\rm D} = \boldsymbol{I}_{\rm D}$ for the scalar channel and $\Gamma_{\rm D} = i\gamma_5$ for the pseudoscalar channel, where $\boldsymbol{I}_{\rm D}$ is the unit matrix in Dirac space. The matrix $\Gamma_{\rm F}$ in flavor space is

$$\Gamma_{\rm F} = \begin{cases} \lambda_3 & \text{for} \quad \pi, \quad a_0 \\ (\lambda_4 \pm i\lambda_5)/\sqrt{2} & \text{for} \quad K, \quad \kappa \\ \lambda_{\rm s} & \text{for} \quad \eta_{\bar{s}s}, \quad \sigma_{\bar{s}s} \\ \lambda_{\rm ns} & \text{for} \quad \eta_{\bar{l}l}, \quad \sigma_{\bar{l}l} \end{cases}, \tag{4.10}$$

where $\lambda_{\rm ns} = {\rm diag}(1, 1, 0)$ and $\lambda_{\rm s} = {\rm diag}(0, 0, \sqrt{2})$.

Mesons η and η' are described as mixed states of $\eta_{\bar{s}s}$ and $\eta_{\bar{l}l}$ states, and σ and f_0 are by the superposition of $\sigma_{\bar{s}s}$ and $\sigma_{\bar{l}l}$ states: Namely,

$$\begin{pmatrix} \eta' \\ \eta \end{pmatrix} = O(\theta_\eta^{ls}) \begin{pmatrix} \eta_{\bar{s}s} \\ \eta_{\bar{l}l} \end{pmatrix}, \quad \begin{pmatrix} f_0 \\ \sigma \end{pmatrix} = O(\theta_\sigma^{ls}) \begin{pmatrix} \sigma_{\bar{s}s} \\ \sigma_{\bar{l}l} \end{pmatrix} \tag{4.11}$$

with the orthogonal matrix $O(\theta)$

$$O(\theta) = \begin{pmatrix} \cos\theta & \sin\theta \\ -\sin\theta & \cos\theta \end{pmatrix}, \tag{4.12}$$

where the mixing angle θ_η^{ls} (θ_σ^{ls}) represents the $\eta_{\bar{s}s}$-$\eta_{\bar{l}l}$ ($\sigma_{\bar{s}s}$-$\sigma_{\bar{l}l}$) mixture and is obtained by diagonalizing coupled meson propagators for $\eta_{\bar{l}l}$ and $\eta_{\bar{s}s}$ ($\sigma_{\bar{l}l}$ and $\sigma_{\bar{s}s}$) states [8]. The Fourier transform $\chi_{\xi\xi'}(q_0^2, \boldsymbol{q}^2)$ of mesonic correlation function $\zeta_{\xi\xi'}(t, \boldsymbol{x}) \equiv \langle 0|\mathrm{T}\left(J_\xi(x)J_{\xi'}^\dagger(0)\right)|0\rangle$ in Minkowski space $x = (t, \boldsymbol{x})$ is described by

$$\chi_{\xi\xi'}(q_0^2, \boldsymbol{q}^2) = \chi_{\xi\xi'}(q_0^2, \tilde{q}^2) = i\int d^4x e^{iq\cdot x}\zeta_{\xi\xi'}(t, \boldsymbol{x}) \tag{4.13}$$

with (external) momentum $q = (q_0, \boldsymbol{q})$, where the symbol T stands for the time-ordered product and $\tilde{q} = \pm|\boldsymbol{q}|$. The random-phase (ring) approximation leads to the Schwinger-Dyson equation

$$\chi_{\xi\xi'} = \Pi_{\xi\xi'} + 2\sum_{\xi'',\ \xi'''} \Pi_{\xi\xi''}G_{\xi''\xi'''}\chi_{\xi'''\xi'} \tag{4.14}$$

for $\chi_{\xi\xi'}$, where $G_{\xi\xi'}$ is an effective four-quark interaction acting between mesons ξ and ξ'. The one-loop polarization function $\Pi_{\xi\xi'}$ is defined by

$$\Pi_{\xi\xi'}(q_0^2, \boldsymbol{q}^2) \equiv (-i)\int \frac{d^4p}{(2\pi)^4}\mathrm{tr}_{\mathrm{c,f,d}}\left(\Gamma_\xi iS(p'+q)\Gamma_{\xi'}iS(p')\right) \tag{4.15}$$

with internal momentum $p = (p_0, \boldsymbol{p})$, where $p' = (p_0 + iA_4, \boldsymbol{p})$ and the trace $\mathrm{tr}_{\mathrm{c,f,d}}$ is taken in color, flavor and Dirac spaces. The quark propagator $S(p)$ is diagonal in flavor space: $S(p) = \mathrm{diag}(S_u, S_d, S_s)$. The polarization function $\Pi_{\xi\xi'}(q_0^2, \boldsymbol{q}^2)$ can be classified with quark and anti-quark flavors f and f' as

$$\begin{aligned} \Pi_{\mathrm{S}}^{ff'} &= (-2i)\int \frac{d^4p}{(2\pi)^4}\mathrm{tr}_{\mathrm{c,d}}\left(iS_f(p'+q)iS_{f'}(p')\right) \\ &= 4i[I_1^f + I_2^{f'} - \left\{q^2 - (M_f + M_{f'})^2\right\}I_3^{ff'}] \end{aligned} \tag{4.16}$$

for the scalar mesons and

$$\begin{aligned} \Pi_{\mathrm{P}}^{ff'} &= (-2i)\int \frac{d^4p}{(2\pi)^4}\mathrm{tr}_{\mathrm{c,d}}\left((i\gamma_5)iS_f(p'+q)(i\gamma_5)iS_{f'}(p')\right) \\ &= 4i[I_1^f + I_2^{f'} - \left\{q^2 - (M_f - M_{f'})^2\right\}I_3^{ff'} \end{aligned} \tag{4.17}$$

for the pseudoscalar mesons, where the trace $\mathrm{tr}_{\mathrm{c,d}}$ is taken in color and Dirac spaces and

$$I_1^f = \int \frac{d^4p}{(2\pi)^4}\mathrm{tr}_{\mathrm{c}}\Big[\frac{1}{p'^2 - M_f^2}\Big], \tag{4.18}$$

$$I_2^f = \int \frac{d^4p}{(2\pi)^4}\mathrm{tr}_{\mathrm{c}}\Big[\frac{1}{(p'+q)^2 - M_f^2}\Big], \tag{4.19}$$

$$I_3^{ff'} = \int \frac{d^4p}{(2\pi)^4}\mathrm{tr}_{\mathrm{c}}\Big[\frac{1}{\{p'^2 - M_f^2\}((p'+q)^2 - M_{f'}^2)}\Big]. \tag{4.20}$$

For finite T, the replacement

$$
\begin{aligned}
& p_0 \to i\omega_n = i(2n+1)\pi T, \\
& \int \frac{d^4p}{(2\pi)^4} \to iT \sum_{n=-\infty}^{\infty} \int \frac{d^3\boldsymbol{p}}{(2\pi)^3}
\end{aligned}
\tag{4.21}
$$

should be taken.

Here we explain the PV regularization for the thermodynamic potential $\Omega_{\rm PNJL}$ of Eq. (4.8) and the three integrals $I_1^f, I_2^f, I_3^{ff'}$. For later convenience, $\Omega_{\rm PNJL}$ is divided into $\Omega_{\rm PNJL} = U_{\rm M} + \mathcal{U} + \sum_{f=u,d,s} \Omega_{\rm F}(M_f)$, while I_1^f and I_2^f are represented by $I(M_f)$ and $I_3^{ff'}$ is by $I_{ff'}(M_f, M_{f'})$. In the PV scheme, the functions $\Omega_{\rm F}(M_f)$, $I(M_f)$ and $I_{ff'}(M_f, M_{f'})$ are regularized as

$$
\begin{aligned}
\Omega_{\rm F}^{\rm reg}(M_f) &= \sum_{\alpha=0}^{2} C_\alpha \Omega_{\rm F}(M_{f;\alpha}), \\
I^{\rm reg}(M_f) &= \sum_{\alpha=0}^{2} C_\alpha I(M_{f;\alpha}), \\
I_{ff'}^{\rm reg}(M_f, M_{f'}) &= \sum_{\alpha=0}^{2} C_\alpha I_{ff'}(M_{f;\alpha}, M_{f';\alpha}),
\end{aligned}
\tag{4.22}
$$

where $M_{f;0} = M_f$ and the $M_{f;\alpha}$ ($\alpha = 1, 2$) denote the masses of auxiliary particles. The parameters $M_{f;\alpha}$ and C_α should satisfy the condition $\sum_{\alpha=0}^{2} C_\alpha = \sum_{\alpha=0}^{2} C_\alpha M_{f;\alpha}^2 = 0$ to remove the quartic, the quadratic and the logarithmic divergence in $I_1, I_2, I_3^{ff'}$, and $\Omega_{\rm F}$. Logarithmic divergence partially remains in $\Omega_{\rm F}^{\rm reg}(M_f)$ even after the subtraction of Eq. (4.22), but the term does not depend on the mean-field variables $(\sigma_l, \sigma_s, \Phi, \bar{\Phi})$ and is not relevant to the determination of mean-field variables for any T. Hence we can simply drop the term. We take $(C_0, C_1, C_2) = (1, 1, -2)$ and $(M_{f;1}^2, M_{f;2}^2) = (M_f^2 + 2\Lambda^2, M_f^2 + \Lambda^2)$, following Ref. [34]. We keep the parameter Λ finite even after the subtraction (4.22), since the present model is non-renormalizable.

π, a_0, K, κ mesons

For $\xi = \pi, a_0, K$ and κ mesons, the effective four-quark interactions $G_{\xi\xi'}$ and the polarization functions $\Pi_{\xi\xi'}$ are diagonal, i.e., $G_{\xi\xi'} = G_\xi \delta_{\xi\xi'}$, $\Pi_{\xi\xi'} = \Pi_\xi \delta_{\xi\xi'}$, since we assume isospin symmetry in the light-quark sector and take the random-phase approximation. We then can easily solve the Schwinger-Dyson equation (4.14) as

$$
\chi_{\xi\xi} = \frac{\Pi_\xi}{1 - 2G_\xi \Pi_\xi}
\tag{4.23}
$$

for $\xi = \pi, a_0, K$ and κ, where the effective couplings G_ξ are obtained by

$$G_{a_0} = G_{\rm S}(T) + \frac{1}{2}G_{\rm D}(T)\sigma_s, \tag{4.24}$$

$$G_{\pi} = G_{\rm S}(T) - \frac{1}{2}G_{\rm D}(T)\sigma_s, \tag{4.25}$$

$$G_{\kappa} = G_{\rm S}(T) + \frac{1}{2}G_{\rm D}(T)\sigma_l, \tag{4.26}$$

$$G_{K} = G_{\rm S}(T) - \frac{1}{2}G_{\rm D}(T)\sigma_l \tag{4.27}$$

and the one-loop polarization functions Π_ξ are written by

$$\Pi_{a_0} = \Pi^{ll}_{\rm S}, \quad \Pi_\pi = \Pi^{ll}_{\rm P}, \quad \Pi_\kappa = \Pi^{sl}_{\rm S}, \quad \Pi_K = \Pi^{sl}_{\rm P}. \tag{4.28}$$

The meson pole mass $M_\xi^{\rm pole}$ and its decay width Γ_ξ are determined from a pole position of $\chi_{\xi\xi}(q_0^2, \vec{q}^2)$ in the lower half-plane of the complex q_0 plane. Taking the rest frame $q = (q_0, \mathbf{0})$ for convenience, we can get the equation

$$\left[1 - 2G_\xi \Pi_\xi(q_0^2, 0)\right]\Big|_{q_0 = M_\xi^{\rm pole} - i\Gamma_\xi/2} = 0 \tag{4.29}$$

for $M_\xi^{\rm pole}$ and Γ_ξ. In the present model, Γ_ξ becomes finite when the meson can decay into a quark-antiquark pair. Here, we take the approximation $\Gamma_\xi / 2M_\xi^{\rm pole} \ll 1$, following Ref. [12]. We numerically confirm the approximation is good for $T \leq 250$ MeV of our interest.

η, η', σ, f_0 mesons

The pole masses of η and η' (σ and f_0) mesons are determined by solving the coupled-channel equations (4.14) for $\eta_{\bar{l}l}$ and $\eta_{\bar{s}s}$ ($\sigma_{\bar{l}l}$ and $\sigma_{\bar{s}s}$). For later convenience, we introduce the correlation functions $\chi_{\xi\xi'}$ with the matrix form

$$\boldsymbol{\chi}_\xi = \begin{pmatrix} \chi_{\xi_{\bar{s}s}\xi_{\bar{s}s}} & \chi_{\xi_{\bar{s}s}\xi_{\bar{l}l}} \\ \chi_{\xi_{\bar{l}l}\xi_{\bar{s}s}} & \chi_{\xi_{\bar{l}l}\xi_{\bar{l}l}} \end{pmatrix} \quad (\xi = \eta, \sigma). \tag{4.30}$$

The Schwinger-Dyson equation for $\boldsymbol{\chi}_\xi$ is obtained from Eq. (4.14) as

$$\boldsymbol{\chi}_\xi = \boldsymbol{\Pi}_\xi + 2\boldsymbol{\Pi}_\xi \boldsymbol{G}_\xi \boldsymbol{\chi}_\xi \tag{4.31}$$

with the coupling matrix $\boldsymbol{G}_\xi$ and the polarization-function matrix $\boldsymbol{\Pi}_\xi$,

$$\boldsymbol{G}_\xi = \begin{pmatrix} G_{\xi_{\bar{s}s}\xi_{\bar{s}s}} & G_{\xi_{\bar{s}s}\xi_{\bar{l}l}} \\ G_{\xi_{\bar{l}l}\xi_{\bar{s}s}} & G_{\xi_{\bar{l}l}\xi_{\bar{l}l}} \end{pmatrix}, \quad \boldsymbol{\Pi}_\xi = \begin{pmatrix} \Pi_{\xi_{\bar{s}s}} & 0 \\ 0 & \Pi_{\xi_{\bar{l}l}} \end{pmatrix}. \tag{4.32}$$

The solution to Eq. (4.31) is

$$\chi_{\xi_{\bar{s}s}\xi_{\bar{s}s}} = \frac{(1 - 2G_{\xi_{\bar{l}l}\xi_{\bar{l}l}}\Pi_{\xi_{\bar{l}l}})\Pi_{\xi_{\bar{s}s}}}{\det\left[\boldsymbol{I} - 2\boldsymbol{\Pi}_\xi \boldsymbol{G}_\xi\right]}, \tag{4.33}$$

$$\chi_{\xi_{\bar{l}l}\xi_{\bar{l}l}} = \frac{(1 - 2G_{\xi_{\bar{s}s}\xi_{\bar{s}s}}\Pi_{\xi_{\bar{s}s}})\Pi_{\xi_{\bar{l}l}}}{\det\left[\boldsymbol{I} - 2\boldsymbol{\Pi}_\xi \boldsymbol{G}_\xi\right]}, \tag{4.34}$$

$$\chi_{\xi_{\bar{s}s}\xi_{\bar{l}l}} = \chi_{\xi_{\bar{l}l}\xi_{\bar{s}s}} = \frac{2G_{\xi_{\bar{l}l}\xi_{\bar{s}s}}\Pi_{\xi_{\bar{s}s}}\Pi_{\xi_{\bar{l}l}}}{\det\left[\boldsymbol{I} - 2\boldsymbol{\Pi}_\xi \boldsymbol{G}_\xi\right]}, \tag{4.35}$$

where $\boldsymbol{I}$ is the unit matrix and the symbol det is determinant taken in the $\xi_{\bar{l}l}$ and $\xi_{\bar{s}s}$ channels. The matrix elements of $\boldsymbol{G}_\eta$ and $\boldsymbol{G}_\sigma$ are explicitly obtained by

$$\begin{aligned} G_{\eta_{\bar{s}s}\eta_{\bar{s}s}} &= G_{\rm S}(T), \quad G_{\eta_{\bar{l}l}\eta_{\bar{l}l}} = G_{\rm S}(T) + \frac{1}{2}G_{\rm D}(T)\sigma_s, \\ G_{\eta_{\bar{s}s}\eta_{\bar{l}l}} &= G_{\eta_{\bar{l}l}\eta_{\bar{s}s}} = \frac{\sqrt{2}}{2}G_{\rm D}(T)\sigma_l, \end{aligned} \tag{4.36}$$

$$\begin{aligned} G_{\sigma_{\bar{s}s}\sigma_{\bar{s}s}} &= G_{\rm S}(T), \quad G_{\sigma_{\bar{l}l}\sigma_{\bar{l}l}} = G_{\rm S}(T) - \frac{1}{2}G_{\rm D}(T)\sigma_s, \\ G_{\sigma_{\bar{s}s}\sigma_{\bar{l}l}} &= G_{\sigma_{\bar{l}l}\sigma_{\bar{s}s}} = -\frac{\sqrt{2}}{2}G_{\rm D}(T)\sigma_l, \end{aligned} \tag{4.37}$$

and the matrix elements of $\boldsymbol{\Pi}_\eta, \boldsymbol{\Pi}_\sigma$ are by

$$\Pi_{\sigma_{\bar{l}l}} = \Pi^{ll}_{\rm S}, \quad \Pi_{\sigma_{\bar{s}s}} = \Pi^{ss}_{\rm S}, \tag{4.38}$$

$$\Pi_{\eta_{\bar{l}l}} = \Pi^{ll}_{\rm P}, \quad \Pi_{\eta_{\bar{s}s}} = \Pi^{ss}_{\rm P}. \tag{4.39}$$

The masses of η and η' (σ and f_0) are determined as poles of $\boldsymbol{\chi}_\eta$ ($\boldsymbol{\chi}_\sigma$), that is, as zero points of the determinant in Eqs. (4.33)-(4.35):

$$\det\left[\boldsymbol{I} - 2\boldsymbol{\Pi}_\xi(q_0^2, 0)\ \boldsymbol{G}_\xi\right]\Big|_{q_0 = M_\xi^{\rm pole} - i\Gamma_\xi/2} = 0. \tag{4.40}$$

Two poles are found in the lower half-plane of the complex q_0 plane. The lighter and heavier pole masses correspond to η and η' (σ and f_0) meson masses, respectively.

4.1.3 Meson screening masses

We extend the method of Chapter 2 for evaluating $M_\xi^{\rm scr}(T)$ from the single-channel system to the multi-channel system. Following Chapter 2, we start with the reason why the derivation of $M_\xi^{\rm scr}(T)$ was not easy in NJL-type effective models before the work of Chapter 2. The $M_\xi^{\rm scr}$ is defined with the spatial correlator $\zeta_{\xi\xi}(0, \boldsymbol{x})$ in the long-distance limit ($r = |\mathbf{x}| \to \infty$):

$$M_\xi^{\rm scr} = -\lim_{r\to\infty} \frac{d\ln\zeta_{\xi\xi}(0, \boldsymbol{x})}{dr}, \tag{4.41}$$

where

$$\zeta_{\xi\xi}(0, \mathbf{x}) = \frac{1}{4\pi^2 ir}\int_{-\infty}^{\infty} d\tilde{q}\ \tilde{q}\chi_{\xi\xi}(0, \tilde{q}^2)e^{i\tilde{q}r}. \tag{4.42}$$

Equation (4.42) has two problems in the $\tilde{q}$ integration. The first problem is from the regularization taken. As already mentioned in Chapter 2, the three-dimensional momentum cutoff commonly used breaks Lorentz invariance even in $T = 0$. This induces an unphysical oscillation in $\zeta_{\xi\xi}(0, \boldsymbol{x})$ particularly at large r [35]. We can easily solve this problem by using the PV regularization. Hence we take the PV regularization. As easily found from Eq. (4.42), direct numerical calculations of the $\tilde{q}$ integration are quite

difficult at large r because of highly oscillation of the integrand. This is the second problem. In order to solve this problem, one can consider analytic continuation of $\chi_{\xi\xi}(0,\tilde{q}^2)$ to the complex $\tilde{q}$ plane. In general, the integration can be made easily with the Cauchy's integral theorem. However, the complex function $\chi_{\xi\xi}(0,\tilde{q}^2)$ has logarithmic cuts in the vicinity of the real $\tilde{q}$ axis; see Fig. 2.1 in Chapter 2. This demands time-consuming numerical calculations to evaluate the contribution of logarithmic cuts [35]. As already shown in Chapters 2 and 3, these logarithmic cuts are avoidable by taking the Matsubara summation over n after the $\boldsymbol{p}$ integration in Eq. (4.21). Consequently, we obtain the regularized function $I^{ff'}_{3,\mathrm{reg}}$ as an infinite series of analytic functions:

$$
\begin{aligned}
I^{ff'}_{3,\mathrm{reg}}(0,\tilde{q}^2) &= iT\sum_{j=1}^{N_c}\sum_{n=-\infty}^{\infty}\sum_{\alpha=0}^{2} C_\alpha \int \frac{d^3\boldsymbol{p}}{(2\pi)^3}\Big[\frac{1}{\boldsymbol{p}^2+\mathcal{M}_f^2}\frac{1}{(\mathbf{p}+\mathbf{q})^2+\mathcal{M}_{f'}^2}\Big] \\
&= \frac{iT}{2\pi^2}\sum_{j,n,\alpha} C_\alpha \int_0^1 dx \int_0^\infty dk\, \frac{k^2}{[k^2+(x-x^2)\tilde{q}^2+(1-x)\mathcal{M}_f^2+x\mathcal{M}_{f'}^2]^2} \\
&= \frac{T}{8\pi\tilde{q}}\sum_{j,n,\alpha} C_\alpha \mathrm{Log}\left(\frac{\mathcal{M}_f+\mathcal{M}_{f'}+i\tilde{q}}{\mathcal{M}_f+\mathcal{M}_{f'}-i\tilde{q}}\right) \qquad (4.43)
\end{aligned}
$$

with

$$
\mathcal{M}_f(T) = \sqrt{M_{f,\alpha}^2+\{(2n+1)\pi T+A_4^{jj}\}^2}, \qquad (4.44)
$$

where "Log" denotes the principle value of the logarithm. The function $iI^{ff'}_{3,\mathrm{reg}}$ is real for real $\tilde{q}$, when $q_0=0$. This means that mesons do not decay into a quark and an antiquark. The function $I^{ff'}_{3,\mathrm{reg}}$ is obtained as an infinite series, but we have numerically confirmed that the sequence of partial sums converges rapidly. In the last form of Eq. (4.43), each term has two physical cuts on the imaginary axis; one is an upward vertical line starting from the branch point $\tilde{q}=i\,(\mathcal{M}_f+\mathcal{M}_{f'})$ and the other is a downward vertical line from the branch point $\tilde{q}=-i\,(\mathcal{M}_f+\mathcal{M}_{f'})$. In the upper half-plane where the contour integration is taken, the lowest branch point is $\tilde{q}=i\,(\mathcal{M}_f+\mathcal{M}_{f'})_{j=1,n=0,\alpha=0}$.

The screening mass M_ξ^{scr} is determined as a pole of $\chi_{\xi\xi}(0,\tilde{q}^2)$ in the upper half-plane. The pole should be located below the lowest branch point:

$$
M_\xi^{\mathrm{scr}} < M_{\mathrm{th}} \equiv (\mathcal{M}_f+\mathcal{M}_{f'})_{j=1,n=0,\alpha=0}\,, \qquad (4.45)
$$

where M_{th} can be considered as "threshold mass" in the sense that meson is in $q\bar{q}$ continuum states when $M_\xi^{\mathrm{scr}} > M_{\mathrm{th}}$. For $\xi=\pi, a_0, K, \kappa$ channels, we can obtain the M_ξ^{scr} by solving the equation

$$
\big[1-2G_\xi \Pi_\xi(0,\tilde{q}^2)\big]\big|_{\tilde{q}=iM_\xi^{\mathrm{scr}}} = 0, \qquad (4.46)
$$

when $M_\xi^{\mathrm{scr}} < M_{\mathrm{th}}$. As T increases, M_ξ^{scr} (pole) approaches M_{th} (the lowest branch point) from below [64, 72], as shown in Fig. 2.1 of Chapter 2. Meanwhile, M_{th} also tends to $2\pi T$ in the high-T limit, because of $A_4^{jj}\to 0$ in Eq. (4.44). Therefore, M_ξ^{scr} approaches $2\pi T$ as T becomes high.

Now we consider the channel mixing. The formalism on meson screening masses is the same as that on meson pole masses. Only the difference is that the external momentum is set to $q = (0, \boldsymbol{q})$. The coupled equations for the $M_\xi^{\rm scr}$ are

$$\det\left[\boldsymbol{I} - 2\boldsymbol{\Pi}_\xi(0, \tilde{q}^2)\ \boldsymbol{G}_\xi\right]\big|_{\tilde{q}=iM_\xi^{\rm scr}} = 0, \tag{4.47}$$

where $\tilde{q} = \pm|\boldsymbol{q}|$ for real $\mathbf{q}$ and it is assume to be a complex value in the actual calculations of $M_\xi^{\rm scr}$. Here note that $M_{\rm th} = 2(\mathcal{M}_l)_{j=1,n=0,\alpha=0}$ for η, σ mesons. For η', f_0 mesons, we consider $M_{\rm th} = 2(\mathcal{M}_s)_{j=1,n=0,\alpha=0}$ as the threshold mass. Strictly speaking, η' (f_0) can decay into a light-quark pair by the channel mixing. However, such a contribution is unphysical for $T \le T_c^{\rm deconf}$ because of color confinement and small for $T \ge T_c^{\rm deconf}$ because of small channel mixing.

4.1.4 Model tuning for LQCD-data analyses

We use LQCD data of Ref. [30] for the $M_\xi^{\rm scr}(T)$ and of Ref. [70] for $\Delta_{l,s}(T)$, since the same lattice setting is taken in the two simulations. In Refs. [30,70], the quark-mass ratio is $m_l/m_s = 1/10$, and the π-meson mass at $T = 0$ is $M_\pi^{\rm pole}(0) = 176$ MeV that is slightly heavier than the experimental value 138 MeV. In model calculations, we then change quark masses from $(m_l, m_s) = (8\ {\rm MeV}, 191\ {\rm MeV})$ to $(m_l, m_s) = (13\ {\rm MeV}, 130\ {\rm MeV})$ to become consistent with the lattice setting. This parameter set is tabulated as set (B) in Table 4.2.

In LQCD simulations of Refs. [30, 70], the chiral-transition temperature T_c^χ is measured to be 196 MeV, but the value established in state-of-art LQCD simulations of Refs. [40, 41] is $T_c^\chi = 154 \pm 9$ MeV. Therefore, we rescale the values of T and $M_\xi^{\rm scr}$ in Refs. [30, 70] to reproduce $T_c^\chi = 154 \pm 9$ MeV.

In LQCD simulations of Ref. [30] for pseudoscalar mesons (η, η') and scalar ones (σ, f_0), the quark-line disconnected diagrams are neglected and thereby the $\eta_{\bar{s}s}$ ($\sigma_{\bar{s}s}$) channel is decoupled with the $\eta_{\bar{l}l}$ ($\sigma_{\bar{l}l}$) channel. Eventually, LQCD data are available only for $\eta_{\bar{s}s}$- and $\sigma_{\bar{s}s}$-meson screening masses. We then switch off the channel mixing in model calculations by setting $G_{\xi_{\bar{s}s}\xi_{\bar{l}l}} = G_{\xi_{\bar{l}l}\xi_{\bar{s}s}} = 0$ for $\xi = \eta, \sigma$, when we analyze the LQCD data on $\eta_{\bar{s}s}$ and $\sigma_{\bar{s}s}$ mesons.

Particularly for η- and η'-meson masses at $T = 0$, it is shown in Ref. [73] that the disconnected diagrams are necessary to reproduce the experimental values, although the diagrams are neglected in finite-T LQCD simulations of Ref. [30] for $M_\xi^{\rm scr}(T)$. The disconnected diagrams contribute to both diagonal and off-diagonal elements of the correlation-function matrix $\boldsymbol{\chi}_\xi$ in Eq. (4.30), whereas the connected diagrams do to only the diagonal elements. The channel mixing induced by the off-diagram elements is thus one of effects induced by the disconnected diagrams. We can then divide the disconnected-diagrams

effects into the channel-mixing effect and *the remaining disconnected-diagram effects acting on the diagonal elements of* $\boldsymbol{\chi}_\xi$. Model calculations with the parameter set (A) include the channel-mixing effect explicitly and the remaining disconnected-diagram effects implicitly, since the set (A) is so determined as to reproduce experimental data on meson pole masses at $T = 0$, particularly on $M_{\eta'}^{\rm pole}(0)$. Hence, we can consider that model calculations with the parameter set (B) also include the channel-mixing effect explicitly and the remaining disconnected-diagram effects implicitly, whereas LQCD calculations do not have any disconnected-diagram effects. Although the channel mixing can be switched off in the model calculations to evaluate $\eta_{\bar{s}s}$- and $\sigma_{\bar{s}s}$-meson screening masses, it should be noted that the model calculations include the remaining disconnected-diagram effects implicitly.

4.2 Numerical Results

4.2.1 Parameter fitting

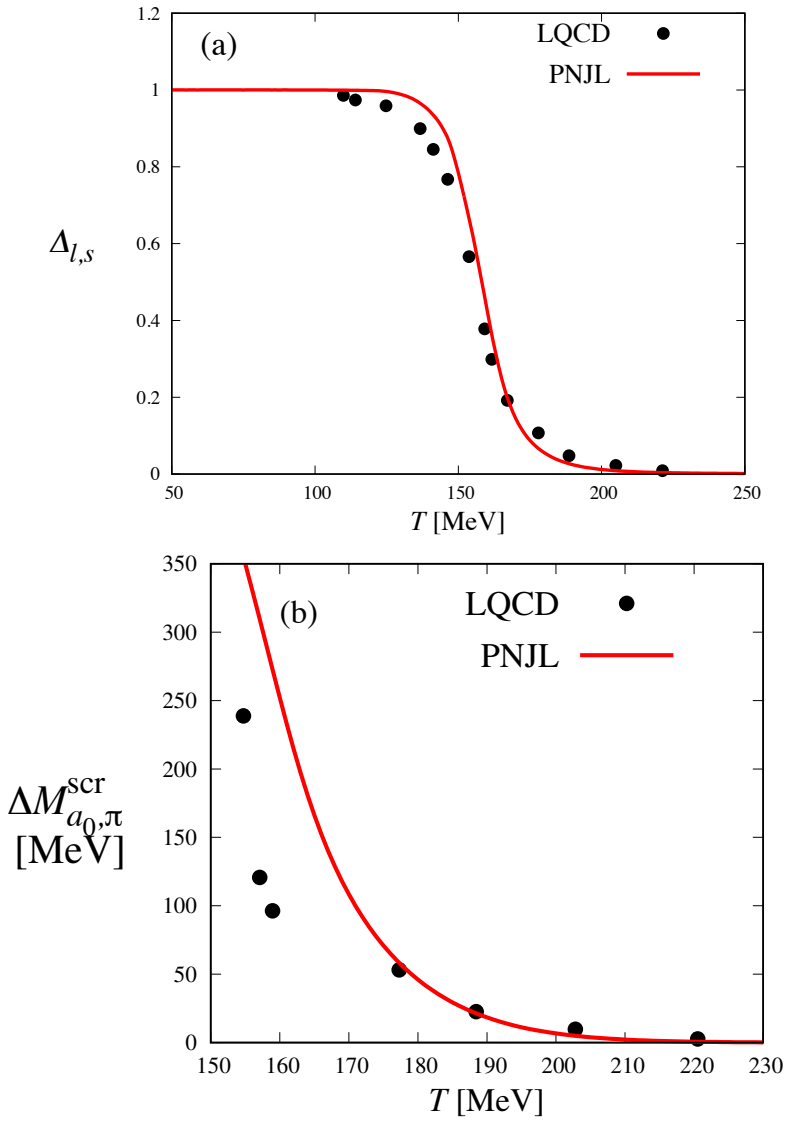

Fig. 4.1: T dependence of (a) $\Delta_{l,s}$ and (b) $\Delta M^{\rm scr}_{a_0,\pi}$. Model results are shown by solid lines, while LQCD data are denoted by closed circles. The parameter set (B) is taken in model calculations. LQCD data are taken from Refs. [30, 70].

As shown in Eqs. (4.2) and (4.3), the present model has adjustable parameters (T_1, b_1) in the KMT coupling strength $G_{\rm D}(T)$ and (T_2, b_2) in the four-quark coupling strength $G_{\rm S}(T)$. The parameters (T_1, b_1) are determined from LQCD data associated with the $U(1)_{\rm A}$-symmetry restoration, i.e., $\Delta M^{\rm scr}_{a_0,\pi} = M^{\rm scr}_{a_0} - M^{\rm scr}_{\pi}$ in $T > 1.1T_c^{\chi} = 170$ MeV where only the $U(1)_{\rm A}$-symmetry breaking survives [61, 72]. Similarly, the parameters (T_2, b_2) are

determined from LQCD data associated with the chiral-symmetry restoration, i.e., the pseudocritical temperature $T_c^\chi = 154 \pm 9$ MeV [40, 41] and the renormalized chiral condensate

$$\Delta_{l,s}(T) = \frac{\sigma_l(T) - \frac{m_l}{m_s}\sigma_s(T)}{\sigma_l(0) - \frac{m_l}{m_s}\sigma_s(0)}. \tag{4.48}$$

Figure 4.1 shows the results of the present parameter fitting for (a) $\Delta_{l,s}(T)$ and (b) $\Delta M^{\rm scr}_{a_0,\pi}(T)$. Note that the parameter set (B) is taken in model calculations. Nice agreement is seen between model results (solid lines) and LQCD data (closed circles), when $(T_1, b_1) = (121, 43.5)$ and $(T_2, b_2) = (131, 83.3)$ in units of MeV. These values are tabulated in Table 4.1.

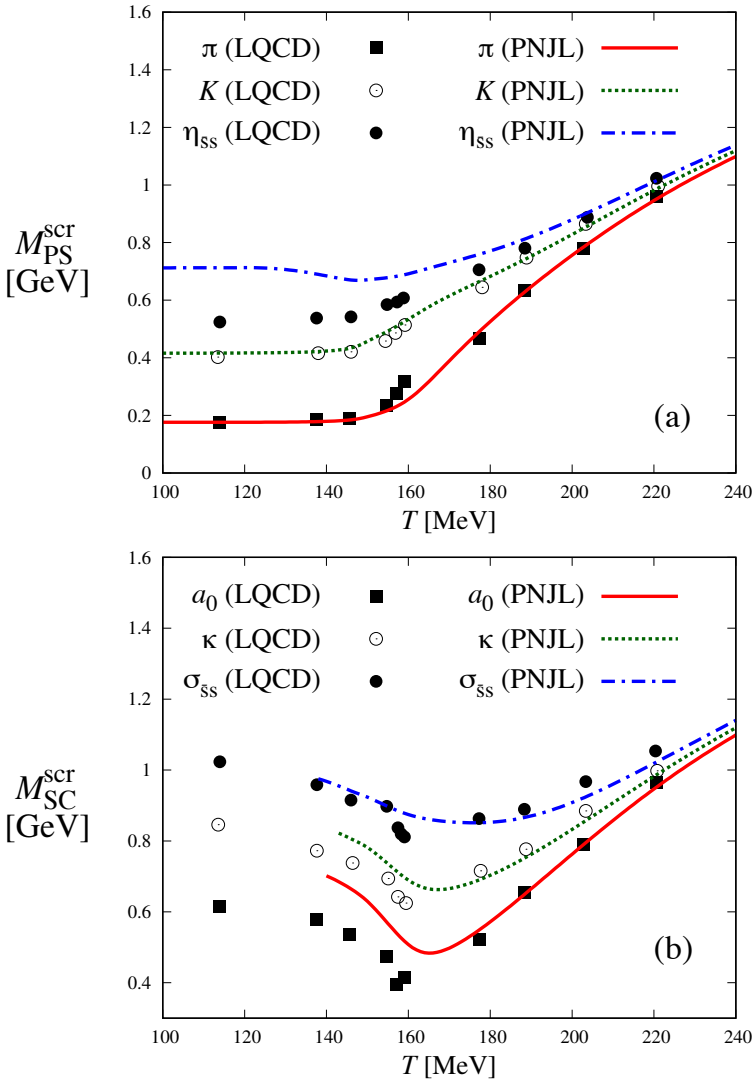

Fig. 4.2: T dependence of meson screening masses for (a) pseudoscalar mesons $\pi, K, \eta_{\bar{s}s}$ and (b) scalar mesons $a_0, \kappa, \sigma_{\bar{s}s}$. Model results are denoted by lines and LQCD data are by symbols. The parameter set (B) is taken in model calculations. LQCD data are taken from from Ref. [30].

4.2.2 Meson screening masses

Here, we consider T dependence of meson screening masses $M_\xi^{\rm scr}(T)$ for pseudoscalar and scalar mesons and analyze LQCD data of Ref. [30], using the present model with the parameter set (B). In the model calculations the channel mixing is switched off, since the disconnected diagrams are neglected in LQCD simulations of Ref. [30].

Figure 4.2 shows T dependence of the $M_\xi^{\rm scr}(T)$ for (a) pseudoscalar mesons ($\xi = \pi, K, \eta_{\bar{s}s}$) and for (b) scalar mesons ($\xi = a_0, \kappa, \sigma_{\bar{s}s}$). The lines stand for model results, and the symbols correspond to LQCD data of Ref. [30]. As mentioned in Sec. 4.1.3, in model calculations the $M_\xi^{\rm scr}(T)$ are derivable when $M_\xi^{\rm scr}(T) < M_{\rm th}$. For the a_0-meson case, for example, the condition is satisfied for $T > 139$ MeV. The solid line representing $M_{a_0}^{\rm scr}(T)$ is then drawn in $T > 139$ MeV. The same procedure is taken for the other lines. In both LQCD data and our model results, all the meson masses tend to $2\pi T$ with respect to increasing T; see Sec. 4.1.3 for the proof. Owing to this property, in $T > 1.04T_c^\chi = 160$ MeV, model results well reproduce LQCD data for all the mesons. In $T < 1.04T_c^\chi = 160$ MeV, agreement between model results and LQCD data is good for pseudoscalar π, K mesons and pretty good for scalar $a_0, \kappa, \sigma_{\bar{s}s}$ mesons. For pseudoscalar $\eta_{\bar{s}s}$ meson, the model result overestimates LQCD data by about $10\% \sim 30\%$ in $T < 1.04T_c^\chi = 160$ MeV, but the deviation becomes small rapidly as T increases from 160 MeV. The deviation in $T < 1.04T_c^\chi = 160$ MeV may come from the remaining disconnected-diagram effects acting on the diagonal elements of $\boldsymbol{\chi}_\eta$. This implies that the channel-mixing effect is also important for $\eta_{\bar{s}s}$ meson in $T < 1.04T_c^\chi = 160$ MeV. This statement is confirmed with model calculations in Sec. 4.2.5. In addition, this statement is consistent with the statement of Ref. [74] that the disconnected diagrams may be suppressed at least for $T \gg T_c^\chi$ by the Debye screening and the weakly interacting nature of the deconfinement phase.

For later discussion, we evaluate the $M_\xi^{\rm scr}(T)$ also in the realistic case, taking the parameter set (A) and taking account of the channel mixing in model calculations. Figure 4.3 shows the results for (a) pseudoscalar mesons π, K, η, η' and for (b) scalar mesons a_0, κ, σ, f_0. As mentioned in Fig. 4.2, all the meson screening masses tend to $2\pi T$. This property is independent of quark masses. At high T, the $M_\xi^{\rm scr}(T)$ calculated with the realistic parameter set (A) are close to those with the set (B). The difference between the former and the latter appear only in $T < T_c^\chi = 154 \pm 9$ MeV.

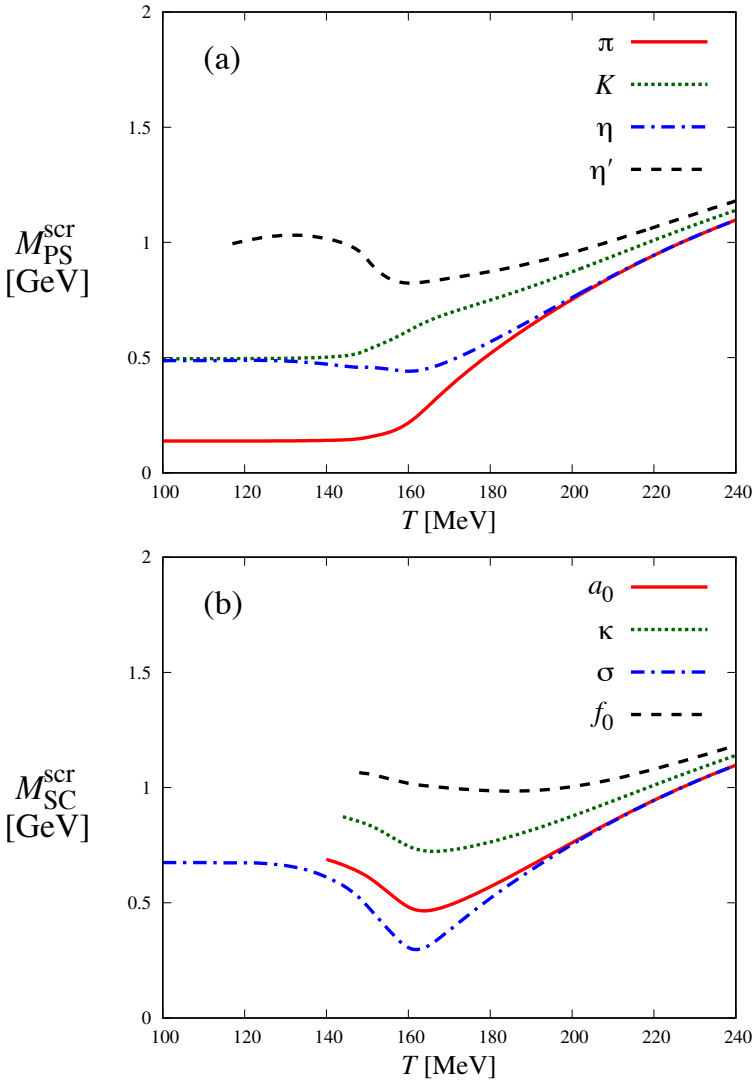

Fig. 4.3: T dependence of meson screening masses for (a) pseudoscalar mesons π, K, η, η' and (b) scalar mesons a_0, κ, σ, f_0 calculated with the realistic parameter set (A). Model results are denoted by lines. In model calculations, the channel mixing is taken into account.

4.2.3 Meson pole masses

Now we predict meson pole masses in the realistic case, taking the parameter set (A) and taking account of the channel mixing in model calculations. The results are shown for pseudoscalar mesons π, K, η, η' in Fig. 4.4(a) and for scalar mesons a_0, κ, σ, f_0 in Fig. 4.4(b). For η' meson, the pole mass in medium with finite T was deduced from heavy-ion collision measurements as $M_{\eta'}^{\rm pole}(T) = 340^{+375}_{-245}$ MeV [6]. In the analyses, $T = 177$ MeV is taken as the default value and T is varied systematically between 140 and 220 MeV. We then denote the experimental data [6] by the rectangle (140 MeV $\leq T \leq$ 220 MeV, 95 MeV $\leq M_{\eta'}^{\rm pole} \leq$ 715 MeV) with the thin dotted vertical line

standing for the default value $T = 177$ MeV. Our model result is consistent with the experimental data. In general, $M_\xi^{\rm pole}$ is not smooth when the $q\bar{q}$-production threshold is opened. This threshold effect is seen at $T = 190$ MeV, e.g., for η' meson.

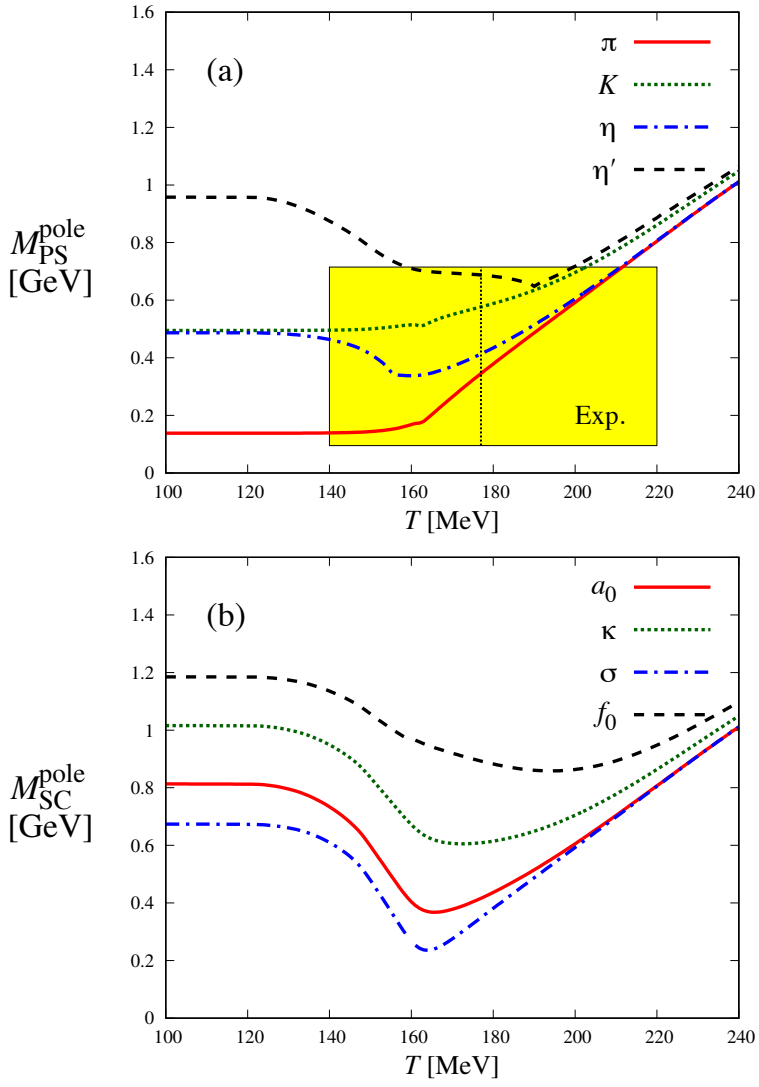

Fig. 4.4: Model prediction on T dependence of meson pole masses for (a) pseudoscalar mesons π, K, η, η' and (b) scalar mesons a_0, κ, σ, f_0. In model calculations, the parameter set (A) is taken and the channel mixing is taken into account. Model results are denoted by lines. For η' meson in panel (a), the experimental data [6] is shown by the rectangle with the thin dotted vertical line $T = 177$ MeV; see the text for the explanation.

4.2.4 Relation between pole and screening masses

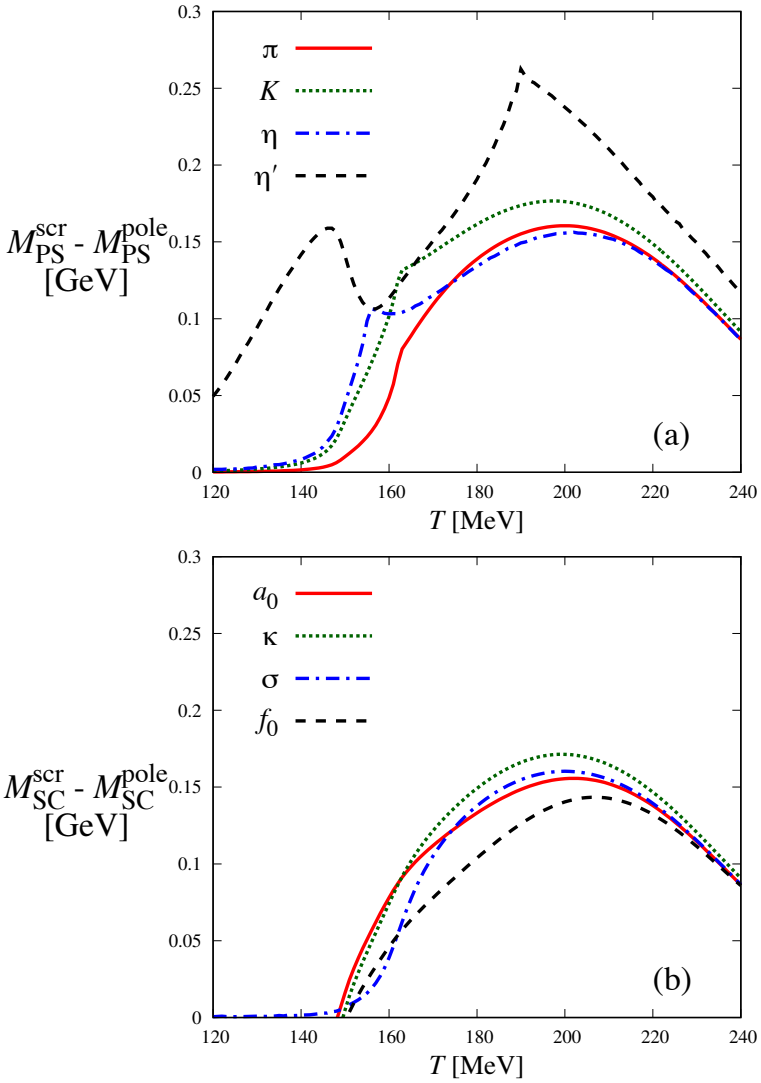

Fig. 4.5: Difference between screening and pole masses for (a) pseudoscalar mesons π, K, η, η' and (b) scalar mesons a_0, κ, σ, f_0. Model results are denoted by lines. In model calculations, the parameter set (A) is taken and the channel mixing is taken into account.

Figure 4.5 shows T dependence of the difference $M_\xi^{\rm scr}(T) - M_\xi^{\rm pole}(T)$ for (a) pseudoscalar mesons π, K, η, η' and for (b) scalar mesons a_0, κ, σ, f_0, where the parameter set (A) is taken and the channel mixing is taken into account in model calculations. Whenever T dependence of the difference is not smooth, it is due to the threshold effect. For pseudoscalar mesons, the difference tends to become larger for heavier meson. For scalar mesons, meanwhile, the difference is universal approximately:

$$M_\xi^{\rm scr}(T) - M_\xi^{\rm pole}(T) \approx M_{\xi'}^{\rm scr}(T) - M_{\xi'}^{\rm pole}(T) \tag{4.49}$$

for $\xi \neq \xi'$. The deviation is about 35 MeV around $T = 200$ MeV. If $M_\xi^{\rm scr}(T)$, $M_{\xi'}^{\rm scr}(T)$ and $M_{\xi'}^{\rm pole}(T)$ are obtained with LQCD simulations, one can estimate T dependence of $M_\xi^{\rm pole}(T)$ from them by using Eq. (4.49).

Next, the relation between $M_\xi^{\rm pole}(T)$ and $M_\xi^{\rm scr}(T)$ is considered through the ratios $M_\xi^{\rm pole}(T)/M_{\xi'}^{\rm pole}(T)$ and $M_\xi^{\rm scr}(T)/M_{\xi'}^{\rm scr}(T)$, where ξ' is assumed to be a scalar (pseudoscalar) meson when ξ is a scalar (pseudoscalar) meson. The identity

$$\frac{M_\xi^{\rm pole}(T)}{M_{\xi'}^{\rm pole}(T)} = \frac{M_\xi^{\rm scr}(T)}{M_{\xi'}^{\rm scr}(T)} \tag{4.50}$$

is satisfied at both $T = 0$ and ∞. The identity at $T = 0$ comes from the fact that $M_\xi^{\rm scr}(0) = M_\xi^{\rm pole}(0)$ for any meson. The identity at $T = \infty$ can be proven as follows. As mentioned in Sec. 4.1.3, in the large-T limit all the $M_\xi^{\rm scr}(T)$ tend to $2\pi T$. Therefore, the ratio $M_\xi^{\rm scr}/M_{\xi'}^{\rm scr}$ becomes 1 in the limit. Similarly, the ratio $M_\xi^{\rm pole}/M_{\xi'}^{\rm pole}$ approaches 1 with respect to increasing T as a consequence of the *effective* $SU(3)_{\rm V}$-symmetry restoration. $SU(3)_{\rm V}$ symmetry is broken by the fact $m_s \neq m_l$ in vacuum, but it is restored *effectively* at high T because the symmetry breaking is the order of $(m_s - m_l)/T$ there; precisely speaking, for the flavor-singlet states, the symmetry is broken also by the quark-line disconnected diagrams, but the diagrams are suppressed by the Debye screening and the weakly interacting nature at high T [74].

Figure 4.6 shows the ratios as a function of T for (a) pseudoscalar mesons ($\xi = K, \eta, \eta'$, $\xi' = \pi$) and for (b) scalar mesons ($\xi = \kappa, \sigma, f_0$, $\xi' = a_0$). Qualitatively, the two ratios have similar T dependence each other for both pseudoscalar and scalar mesons: Namely,

$$\frac{M_\xi^{\rm pole}(T)}{M_{\xi'}^{\rm pole}(T)} \simeq \frac{M_\xi^{\rm scr}(T)}{M_{\xi'}^{\rm scr}(T)}. \tag{4.51}$$

Quantitatively, the relation (4.51) is well satisfied within 20% error for pseudoscalar and scalar mesons. The relation is useful, because it allows us to estimate $M_\xi^{\rm pole}(T)$ for lighter ξ-meson from $M_{\xi'}^{\rm pole}(T)$ for heavier ξ'-meson and $M_\xi^{\rm scr}(T)/M_{\xi'}^{\rm scr}(T)$ that may be obtainable with state-of-art LQCD simulations.

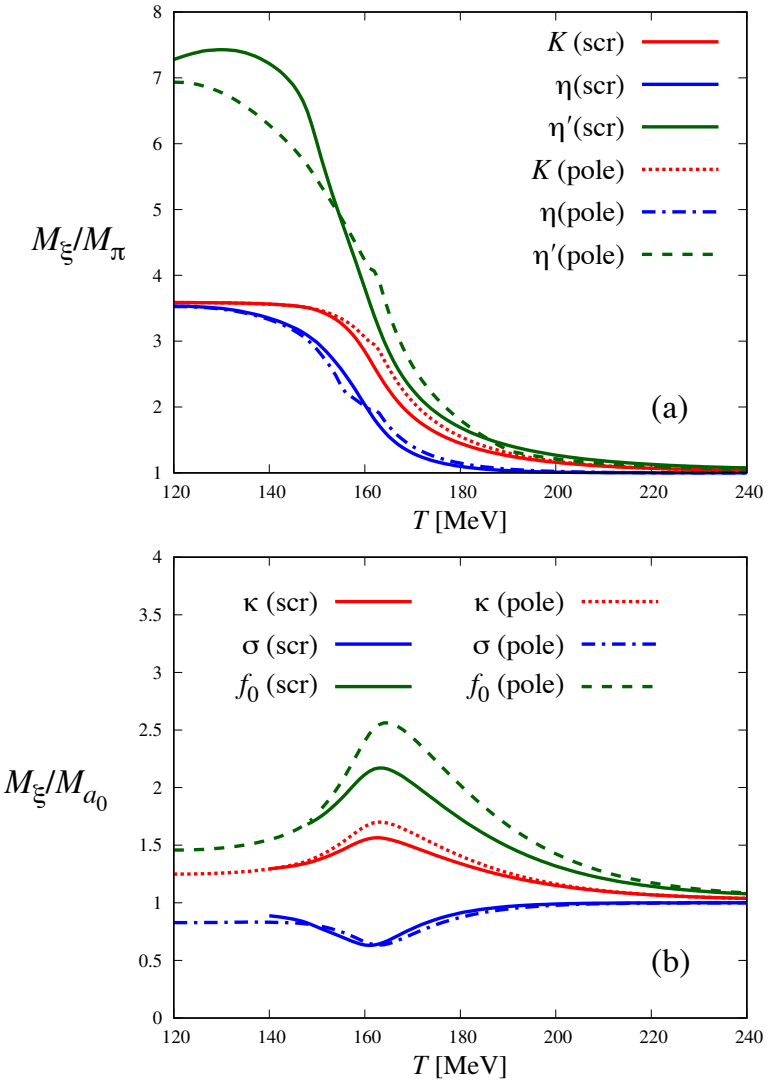

Fig. 4.6: T dependence of $M_\xi^{\rm pole}/M_{\xi'}^{\rm pole}$ and $M_\xi^{\rm scr}/M_{\xi'}^{\rm scr}$ for (a) pseudoscalar mesons ($\xi = K, \eta, \eta',\ \xi' = \pi$) and (b) scalar mesons ($\xi = \kappa, \sigma, f_0,\ \xi' = a_0$). The ratios $M_\xi^{\rm scr}/M_{\xi'}^{\rm scr}$ are denoted by solid lines, and the ratios $M_\xi^{\rm pole}/M_{\xi'}^{\rm pole}$ are by dotted, dashed and dot-dashed lines. In model calculations, the parameter set (A) is taken and the channel mixing is taken into account.

4.2.5 Discussion

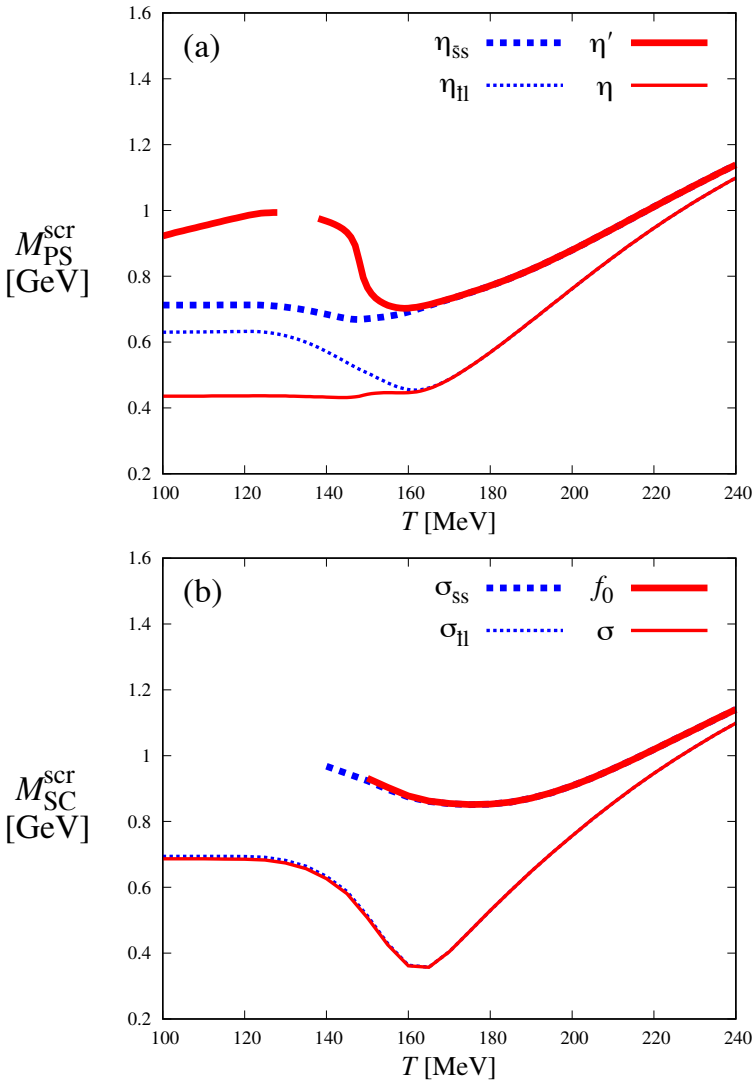

Fig. 4.7: T dependence of channel-mixing effects on (a) η- and η'-meson screening masses and (b) σ- and f_0-meson screening masses. In panel (a) (panel (b)), the thin and thick solid lines denote screening masses of η and η' (σ and f_0) mesons, respectively, and the thin and thick dashed lines correspond to screening masses of $\eta_{\bar{l}l}$ and $\eta_{\bar{s}s}$ ($\sigma_{\bar{l}l}$ and $\sigma_{\bar{s}s}$) channels, respectively. The parameter set (B) is taken in model calculations.

T dependence of the channel-mixing effect is investigated within model calculations. The parameter set (B) is taken in model calculations. In Fig. 4.7(a), the thin and thick solid lines denote the results of model calculations with the channel mixing for η- and η'-meson screening masses, respectively. Note that the lines are drawn when the condition $M_\xi^{\rm scr}(T) < M_{\rm th}$ is satisfied. When the channel mixing is switched off, the thin and thick solid lines are changed into the thin and thick dashed lines that stand for $\eta_{\bar{l}l}$- and $\eta_{\bar{s}s}$-meson screen-

ing masses, respectively. As expected in Sec. 4.2.2, the channel-mixing effect is large for η- and η'-meson screening masses in $T < 1.04T_c^\chi = 160$ MeV. This is a result of the fact that the mass difference between the thin and thick dashed lines is small there; for example, the difference is 113 MeV at $T = 140$ MeV. For $T > 1.04T_c^\chi = 160$ MeV, meanwhile, the channel-mixing effect is negligible, since $G_{\eta_{\bar{s}s}\eta_{\bar{l}l}} = G_{\eta_{\bar{l}l}\eta_{\bar{s}s}} = G_{\rm D}(T)\sigma_l/\sqrt{2}$ is quite small in Eq. (4.32) because of $\sigma_l \approx 0$. In Fig. 4.7(b), the thin and thick solid lines stand for the results of model calculations with the channel mixing for σ- and f_0-meson screening masses, respectively, while the thin and thick dashed lines correspond to the results of model calculations without the channel mixing for $\sigma_{\bar{l}l}$- and $\sigma_{\bar{s}s}$-meson screening masses, respectively. In the case of σ and f_0 mesons, the channel-mixing effect is negligible for any T. This stems from the fact that the mass difference between the thin and thick dashed lines is large in $T < 1.04T_c^\chi = 160$ MeV (e.g., the difference is 335 MeV at $T = 140$ MeV) and $G_{\sigma_{\bar{s}s}\sigma_{\bar{l}l}} = G_{\sigma_{\bar{l}l}\sigma_{\bar{s}s}} = -G_{\rm D}(T)\sigma_l/\sqrt{2} \approx 0$ because of $\sigma_l \approx 0$ in $T > 1.04T_c^\chi = 160$ MeV. Therefore, the channel mixing as the characteristics of the disconnected diagrams is important only for η- and η'-meson screening masses in $T < 1.04T_c^\chi = 160$ MeV. The discussion made above for the channel-mixing effect on η, η', σ, f_0-meson *screening* masses is confirmed to be true also on η, η', σ, f_0-meson *pole* masses.

4.3 Short Summary

We have predicted T dependence of $M_\xi^{\rm pole}(T)$ from T dependence of $M_\xi^{\rm scr}(T)$ calculated with LQCD simulations as the first-principle calculation of QCD. For this purpose, we have considered a new version of the PNJL model with the following three improvements:

(1) The PV regularization was taken in the model. The use of the regularization is essential for the calculation of $M_\xi^{\rm scr}(T)$ in order to avoid artificial oscillations in mesonic correlation functions in coordinate space. This regularization also guarantees the identity $M_\xi^{\rm scr}(T) = M_\xi^{\rm pole}(T)$ at $T = 0$.

(2) We introduced the T-dependent coupling strength $G_{\rm S}(T)$ to four-quark interaction in order to describe the chiral-symmetry restoration. The $G_{\rm S}(T)$ was determined from the renormalized chiral condensate calculated with LQCD simulations.

(3) We introduced the T-dependent coupling strength $G_{\rm D}(T)$ to six-quark KMT interaction in order to describe the $U(1)_{\rm A}$-symmetry restoration. The $G_{\rm D}(T)$ was determined from pion and a_0-meson screening masses calculated with LQCD simulations, particularly in $T \gtrsim T_c^\chi$.

First, we have shown that the effective model well reproduces LQCD data on T dependence of $M_\xi^{\rm scr}(T)$ for both scalar and pseudoscalar mesons. We have then predicted T dependence of $M_\xi^{\rm pole}(T)$ for scalar and pseudoscalar mesons, using the PNJL model mentioned above. Particularly for η' meson, we have shown that our model prediction agrees with the experimental results at finite T extracted from indirect measurements in heavy-ion collisions. Finally, we have found that the relation $M_\xi^{\rm scr}(T) - M_\xi^{\rm pole}(T) \approx M_{\xi'}^{\rm scr}(T) - M_{\xi'}^{\rm pole}(T)$ is pretty good when ξ and ξ' are scalar mesons and also found that the relation $M_\xi^{\rm scr}(T)/M_{\xi'}^{\rm scr}(T) \approx M_\xi^{\rm pole}(T)/M_{\xi'}^{\rm pole}(T)$ is satisfied within 20% error not only when ξ and ξ' are pseudoscalar mesons and but also when ξ and ξ' are scalar mesons. The relations indicate that one can determine T dependence of $M_\xi^{\rm pole}(T)$ from $M_\xi^{\rm scr}(T), M_{\xi'}^{\rm scr}(T)$ and $M_{\xi'}^{\rm pole}(T)$. In state-of-arts LQCD calculations, $M_{\xi'}^{\rm pole}(T)$ may be obtainable for heavier mesons such as D meson. In preliminary model calculations, we have checked that the two relations are well satisfied also for mesons composed of charm quark.

Chapter 5

Summary and Outlook

The purpose of this thesis is to predict meson pole masses $M_\xi^{\rm pole}(T)$ reliably from the corresponding meson screening masses $M_\xi^{\rm scr}(T)$ calculated with LQCD simulations. We had the following three problems in order to accomplish the purpose:

(I) In principle, T dependence of $M_\xi^{\rm pole}(T)$ can be determined from measurements in heavy-ion collisions. However, the measurements are indirect, so that the experimental results have large uncertainty in general. In fact, η'-meson pole mass was recently measured at finite T, but the results have large errors mainly coming from data analyses.

(II) LQCD simulation is the first-principle calculation of QCD. However, the calculation of $M_\xi^{\rm pole}(T)$ is quite difficult compared with $M_\xi^{\rm scr}(T)$, because the imaginary-time size is limited up to $1/T$. The difficulty is more serious as T increases. In fact, pole-mass calculations are usually done under the quench approximation (without dynamical quarks), and/or the small lattice size. Meanwhile, meson screening masses are calculated, without the quench approximation and small lattice size, in the wide temperature range $T \lesssim 800$ MeV [30].

(III) In effective models, screening-mass calculations were quite difficult compared with pole-mass calculation, because it required time-consuming numerical calculations.

First, we solved problem (III) in Chapter 2 by considering the following two prescriptions:

(1) The Pauli-Villars (PV) regularization is taken.

(2) A new prescription is proposed in calculating the spatial correlation function for meson screening mass. In the new prescription, the internal-momentum integration is done before the Matsubara summation.

These two prescriptions extremely reduce numerical costs, as shown in Sec. 2.4 of Chapter 2.

Second, we solved problems (I) and (II) by proposing new versions of EPNJL and PNJL models that reproduce LQCD data on $M_\xi^{\rm scr}(T)$:

(A) In the new version of EPNJL model proposed in Chapter 3, T dependence was introduced to the coupling strength of six-quark KMT interaction in order to describe the $U(1)_{\rm A}$-symmetry restoration.

(B) In the new version of PNJL model proposed in Chapter 4, T dependence was introduced to the coupling strengths of four-quark and six-quark KMT interaction in order to describe the chiral-symmetry and the $U(1)_{\rm A}$-symmetry restoration simultaneously.

We recommend Model (B) for analyses of meson screening and pole masses, since Model (B) is more practical than Model (A). Therefore, we conclude that the purpose "reliable prediction of $M_\xi^{\rm pole}(T)$ from $M_\xi^{\rm scr}(T)$ calculated with LQCD" can be accomplished by Model (B) with prescriptions (1) and (2). In fact, Model (B) has successfully reproduced LQCD data on $M_\xi^{\rm scr}(T)$ for scalar and pseudoscalar mesons. We have then predicted the corresponding meson pole masses $M_\xi^{\rm pole}(T)$ by using Model (B). Especially for η' meson, we have found that the predicted value is consistent with the experimental value recently reported in Ref. [6]. Model (B) also proposed the following approximate relations between $M_\xi^{\rm pole}(T)$ and $M_\xi^{\rm scr}(T)$: (i) $M_\xi^{\rm scr}(T) - M_\xi^{\rm pole}(T) \approx M_{\xi'}^{\rm scr}(T) - M_{\xi'}^{\rm pole}(T)$ and (ii) $M_\xi^{\rm scr}(T)/M_{\xi'}^{\rm scr}(T) \approx M_\xi^{\rm pole}(T)/M_{\xi'}^{\rm pole}(T)$, when ξ'-meson has the same spin-parity as ξ-meson. Using relations (i) and (ii), one can estimate $M_\xi^{\rm pole}(T)$ from $M_\xi^{\rm scr}(T), M_{\xi'}^{\rm scr}(T)$ and $M_{\xi'}^{\rm pole}(T)$. When ξ'-meson is heavy, $M_{\xi'}^{\rm pole}(T)$ may be obtainable with latest LQCD simulations.

In this thesis, we have considered scalar and pseudoscalar mesons composed of u, d and s quarks for finite T but zero baryon density. As important future works, it is interesting to clarify properties of $M_\xi^{\rm pole}$ and $M_\xi^{\rm scr}$ particularly in the following three cases by extending the present method:

(1) Light vector mesons for finite T and baryon density,

(2) Charmed and bottomed vector mesons for finite T and baryon density,

(3) Light mesons for low T but high baryon density.

The studies (1) and (2) are fascinating from the experimental point of view. These mesons decay into photons in hot-QCD matter produced by heavy-ion collisions. Once photons are produced in hot-QCD matter, they behave as free particles there, and finally decay into a dilepton in the outside of hot-QCD matter. Therefore, the dilepton-mass spectra contain information of hot-QCD matter, and are good probes of QGP formation in experiments. In fact, thermal and medium modifications of ρ and Υ mesons have

been observed in dilepton invariant mass spectra in RHIC [75] and LHC [76]. The ρ-meson mass is considered to be related with the restoration of chiral symmetry and the Υ-meson mass may be an indicator of the Debye screening in confinement force. It is an exciting subject to extract these physics from the measurements by using our method.

The study (3) may be related to the following famous puzzle in recent two-solar-mass observations of neutron star (NS) through the Shapiro delay [77]. In the inner core of NS, high densities are realized because of gravity. Therefore, both neutrons and hyperons should appear in the core. However, the equation of state (EoS) with hyperons becomes softer from the EoS without hyperons, and consequently can not explain the two-solar-mass observations. This problem is called "Hyperon puzzle". I consider that density dependence of light meson masses may be related to the Hyperon puzzle by changing baryon-baryon interactions.

Acknowledgements

First of all, I would like to express the deepest appreciation to Prof. Masanobu Yahiro. He taught me how interesting and rich the QCD phase structures are. He always supported my research and encouraged me as a supervisor. I learned not only various ideas on physics but also mental attitudes as a researcher and a leader.

I would like to thank Prof. Hiroaki Kouno. He gave me a lot of useful comments with his great insights. His nice guidance led to my finding the profundity of phenomenological studies. I would like to extend my special thanks to my three seniors, Dr. Kouji Kashiwa, Dr. Takahiro Sasaki and Dr. Junichi Takahashi. Thank to helpful discussions with them, I could obtain much beneficial knowledge and practical techniques such as logical, computational and presentation skills. I would like to appreciate Associate Prof. Yoshifumi R. Shimizu, Assistant Prof. Takuma Matsumoto and Assistant Prof. Ken-ichi Okumura for useful comments about nuclear physics and elementary particle physics in all the seminars and their lessons. I am very grateful to all the members of theoretical nuclear physics and elementary particle physics.

I show my profound appreciation to Yuki Yamaji, Yuko Megumi, Saori Shigematsu, Hiromi Tsuchijima, Megumi Ieda, Noriko Taguchi, Mayumi Takaki, and Mariko Komori for their practical supports.

This work was supported by Grants-in-Aid for Scientific Research (No. 27-3944) from the Japan Society for the Promotion of Science (JSPS).

Finally, my gratefulness would go to my family for supporting me through all my life. Without their supports I could not have accomplished this thesis.

Bibliography

[1] K. A. Olive (Particle Data Group), Chin. Phys. C **38**, 090001 (2014).

[2] L. D. McLerran and B. Svetitsky, Phys. Rev. D **24**, 450 (1981).

[3] S. Weinberg, Phys. Rev. **11**, 3583 (1975).

[4] G. 't Hooft, Phys. Rev. Lett. **37**, 8 (1976); Phys. Rev. D **14**, 3432 (1976); **18**, 2199(E) (1978).

[5] J. Adams *et al.* (STAR Collaboration), Nucl. Phys. A **757**, 102 (2005).

[6] T. Csörgő, R. Vértesi, and J. Sziklai, Phys. Rev. Lett. **105**, 182301 (2010).

[7] H. J. Rothe, Lattice Gauge Theories: An Introduction (World Scientific Lecture Notes in Physics).

[8] S. P. Klevansky, Rev. Mod. Phys. **64**, 649 (1992); T. Hatsuda, and T. Kunihiro, Phys. Rep. **247**, 221 (1994); M. Buballa, Phys. Rep. **407**, 205 (2005).

[9] P. N. Meisinger, and M. C. Ogilvie, Phys. Lett. B **379**, 163 (1996).

[10] A. Dumitru, and R. D. Pisarski, Phys. Rev. D **66**, 096003 (2002).

[11] K. Fukushima, Phys. Lett. B **591**, 277 (2004); K. Fukushima, Phys. Rev. D **77**, 114028 (2008); Phys. Rev. D **78**, 114019 (2008).

[12] P. Costa, M. C. Ruivo, C. A. de Sousa, and Yu. L. Kalinovsky, Phys. Rev. D **71**, 116002 (2005).

[13] S. K. Ghosh, T. K. Mukherjee, M. G. Mustafa, and R. Ray, Phys. Rev. D **73**, 114007 (2006).

[14] E. Megías, E. R. Arriola, and L. L. Salcedo, Phys. Rev. D **74**, 065005 (2006).

[15] C. Ratti, M. A. Thaler, and W. Weise, Phys. Rev. D **73**, 014019 (2006).

[16] M. Ciminale, R. Gatto, G. Nardulli, and M. Ruggieri, Phys. Lett. B **657**, 64 (2007); M. Ciminale, R. Gatto, N. D. Ippolito, G. Nardulli, and M. Ruggieri, Phys. Rev. D **77**, 054023 (2008).

[17] C. Ratti, S. Rößner, M. A. Thaler, and W. Weise, Eur. Phys. J. C **49**, 213 (2007).

[18] S. Rößner, C. Ratti, and W. Weise, Phys. Rev. D **75**, 034007 (2007).

[19] H. Hansen, W. M. Alberico, A. Beraudo, A. Molinari, M. Nardi, and C. Ratti, Phys. Rev. D **75**, 065004 (2007).

[20] C. Sasaki, B. Friman, and K. Redlich, Phys. Rev. D **75**, 074013 (2007).

[21] B. -J. Schaefer, J. M. Pawlowski, and J. Wambach, Phys. Rev. D **76**, 074023 (2007).

[22] K. Kashiwa, H. Kouno, M. Matsuzaki, and M. Yahiro, Phys. Lett. B **662**, 26 (2008).

[23] P. Costa, M. C. Ruivo, C. A. de Sousa, H. Hansen, and W. M. Alberico, Phys. Rev. D **79**, 116003 (2009).

[24] M. C. Ruivo, M. Santos., P. Costa, and C. A. de Sousa, Phys. Rev. D **85**, 036001 (2012).

[25] Y. Sakai, T. Sasaki, H. Kouno, and M. Yahiro, Phys. Rev. D **82**, 076003 (2010).

[26] T. Sasaki, Y. Sakai, H. Kouno, and M. Yahiro, Phys. Rev. D **84**, 091901(R) (2011).

[27] M. D'Elia, and F. Sanfilippo, Phys. Rev. D **80**, 111501(R) (2009).

[28] P. de Forcrand, and O. Philipsen, Phys. Rev. Lett. **105**, 152001 (2010) [arXiv:1004.3144].

[29] J. B. Kogut, and D. K. Sinclair, Phys. Rev. D **70**, 094501 (2004).

[30] M. Cheng, S. Datta, A. Francis, J. van der Heide, C. Jung, O. Kaczmarek, F. Karsch, and E. Laermann *et al.*, Eur. Rhys. J. C **71**, 1564 (2011) [arXiv: 1010.1216].

[31] M. C. Ruivo, P. Costa, and C. A. de Sousa, Phys. Rev. D **86**, 116007 (2012).

[32] W. Pauli, and F. Villars, Rev. Mod. Phys. **21**, 434 (1949).

[33] E. R. Arriola, and L. L. Salcedo, Nucl. Phys. A **590**, 703 (1995).

[34] C. Itzykson, and J. -B. Zuber, 1980, *Quantum Field Theory* (McGraw-Hill, New York)

[35] W. Florkowski, Acta Phys. Pol. B **28**, 2079 (1997) [arXiv:9701223].

[36] V. L. Eletskii, and B. L. Ioffe, Sov. J. Nucl. Phys. **48**, (1988) 384.

[37] V. Bernard, and D. Vautherin, Phys. Rev. D **40**, 1615 (1989).

[38] F. Karsch, Lect. Notes Phys. **583**, 209 (2002).

[39] O. Kaczmarek and F. Zantow, Phys. Rev. D. **71**, 114510 (2005).

[40] S. Borsanyi *et al.* (Wuppertal-Budapest Collaboration), J. High Energy Phys. 09 (2010) 073 [arXiv:1005.3508].

[41] A. Bazavov *et al.* (HotQCD Collaboration), Phys. Rev. D **85**, 054503 (2012) [arXiv: 1111.1710].

[42] R. D. Pisarski, and L. G. Yaffe, Phys. Lett. B **97**, 110 (1980).

[43] E. V. Shuryak, Comments Nucl. Part. Phys. **21**, 235 (1994) [arXiv:9310253].

[44] K. Kanaya, [arXiv: 1012.4235]; [arXiv: 1012.4247].

[45] R. D. Pisarski, and F. Wilczek, Phys. Rev. D **29**, 338(R) (1984).

[46] E. Vicari, Proc. Sci., LATTICE2007 (**2007**) 23 [arXiv: 0709.1014].

[47] A. Pelissetto, and E. Vicari, Phys. Rev. D **88**, 105018 (2013).

[48] M. Fukugita, H. Mino, M. Okawa, and A. Ukawa, Phys. Rev. Lett. **65**, 816 (1990).

[49] M. Fukugita, H. Mino, M. Okawa, and A. Ukawa, Phys. Rev. D **42**, 2936 (1990).

[50] F. R. Brown, F. P. Butler, H. Chen, N. H. Christ, Z. Dong, W. Schaffer, L. I. Unger, and A. Vaccarino, Phys. Rev. Lett. **65**, 2491 (1990).

[51] F. Karsch, Phys. Rev. D **49**, 3791 (1994).

[52] F. Karsch, and E. Laermann, Phys. Rev. D **50**, 6954 (1994).

[53] Y. Iwasaki, K. Kanaya, S. Kaya, and T. Yoshie, Phys. Rev. Lett. **78**, 179 (1997).

[54] S. Aoki *et al.* (JLQCD Collaboration), Phys. Rev. D **57**, 3910 (1998).

[55] A. A. Khan *et al.* (CP-PACS Collaboration), Phys. Rev. D **63**, 034502 (2000).

[56] C. Bernard, C. DeTar, S. Gottlieb, U. M. Heller, J. Hetrick, K. Rummukainen, R. L. Sugar, and D. Toussaint, Phys. Rev. D **61**, 054503 (2000).

[57] M. D'Elia, A. Di Giacomo, and C. Pica, Phys. Rev. D **72**, 114510 (2005).

[58] S. Ejiri *et al.*, Phys. Rev. D **80**, 094505 (2009).

[59] C. Bonati, P. de Forcrand, M. D'Elia, O. Philipsen, and F. Sanfilippo, Phys. Rev. D **90**, 074030 (2014).

[60] M. I. Buchoff, M. Cheng, N. H. Christ, H. -T. Ding, C. Jung, F. Karsch, Z. Lin, and R. D. Mawhinney *et al.*, Phys. Rev. D **89**, 054514 (2014) [arXiv: 1309.4149].

[61] T. Bhattacharya, M. I. Buchoff, N. H. Christ, H. -T. Ding, R. Gupta, C. Jung, F. Karsch, and Z. Lin *et al.*, Phys. Rev. Lett. **113**, 082001 (2014) [arXiv: 1402.5175].

[62] M. Kobayashi, and T. Maskawa, Prog. Theor. Phys. **44**, 1422 (1970); M. Kobayashi, H. Kondo, and T. Maskawa, Prog. Theor. Phys. **45**, 1955 (1971).

[63] Y. Aoki, S. Borsányi, S. Dürr, Z. Fodor,S. D. Katz, S. Krieg, and K. K. Szabo, J. High Energy Phys. 06 (2009) 088 [arXiv:0903.4155].

[64] M. Ishii, T. Sasaki, K. Kashiwa, H. Kouno, and M. Yahiro, Phys. Rev. D **89**, 071901(R) (2014). [arXiv:1312.7424].

[65] J. Braun, H. Gies, and J. M. Pawlowski, Phys. Lett. B **684**, 262 (2010) [arXiv:0708.2413].

[66] F. Marhauser, and J. M. Pawlowski, [arXiv:0812.1144].

[67] E. R. Arriola, L. L. Salcedo, and E. Megías, Acta Phys. Pol. B **45**, 2407(2014) .

[68] K. Fukushima, Phys. Rev. D **77**, 114028 (2008); Phys. Rev. D **78**, 039902 (2008).

[69] K. Kashiwa, M. Yahiro, H. Kouno, M. Matsuzaki, and Y. Sakai, J. Phys. G **36**, 105001 (2009).

[70] M. Cheng, N. H. Christ, S. Datta, J. van der Heide, C. Jung, F. Karsch, O. Kaczmarek, and E. Laermann *et al.*, Phys. Rev. D **77**, 014511 (2008).

[71] F. E. Close, An Introduction to Quarks and Partons (Academic Press, New York, 1997); L. Brekke and J. L. Rosner, Nucl. Part. Phys. **18**, (1988) 347.

[72] M. Ishii, K. Yonemura, J. Takahashi, H. Kouno, and M. Yahiro, Phys. Rev. D **93**, 016002 (2016). [arXiv:1504.04463].

[73] N. H. Christ *et al.* (RBC and UKQCD Collaboration), Phys. Rev. Lett. **105**, 241601 (2010).

[74] A. Bazavov *et al.* (HotQCD Collaboration), Phys. Rev. D **86**, 094503 (2012).

[75] L. Adamczyk *et al.* (STAR Collaboration), Phys. Rev. Lett. **113**, 022301 (2014).

[76] T. Dahms, Proc. 14th Int. Conf. on B-Physics at Hadron Machines (Beauty 2013)

[77] P. B. Demorest *et al.* , Nature **467**, 1081 (2010).